A Tuneable THz Source Using Excitonic Non-Linear Effects and Application in Absorption Spectroscopy

By:

Avan N. Majeed

A thesis submitted in partial fulfilment of the requirements for the degree of Doctor of Philosophy

Department of Electronic and Electrical Engineering

The University of Sheffield

Intentionally Blank

Abstract

This thesis reports the generation of tuneable THz radiation (0.2-6 THz) through second order nonlinear effects in the excitation of excitons in GaAs/AlAs multi-quantum wells (MQWs). A MQW GaAs/AlAs sample was designed to have excitonic resonances at a wavelength accessible by commercially available lasers (850 nm, 300 mW), and have E1HH1–E1LH1 splitting of 9.1 meV. The sample was grown by MBE on a heavily n-doped GaAs substrate to allow biasing of future devices. Following growth, an optical access mesa-diode structure was fabricated to assess the structure through photocurrent (PC) spectroscopy. The sample was then prepared prior to the preliminary THz measurements, with the substrate and cap layer being removed. The sample was then capillary bonded to a diamond heat spreader.

Two collimated lasers were used to excite the excitonic resonances. Both lasers were normally incident to the sample surface. A clear THz signal was observed in the case of collinear excitation, which scaled with the density of states of the excitons. Power dependence measurements confirm this as a second order non-linear effect. Hence the THz wave is realized by difference frequency generation, utilizing an enhancement to χ^3 obtained via resonant excitation of III-V semiconductor quantum well excitons. The symmetry of the quantum wells is broken by utilizing the built-in electric field across a p–i–n junction to produce effective χ^2 processes, derived from the high χ^3. This χ^2 media shows an onset of non-linear processes at ~ 4W/cm^2, allowing area (and hence power) scaling of the THz emitter. Phase matching was achieved laterally through excitation akin to two-colour interference.

Using a simple interferometer, and fitting the measured power with the expected transmission of a Fabry-Perot etalon, frequency measurements confirm the ability to tune the THz radiation from 0.75-3 THz, with linewidths of ~20 GHz and efficiencies of ~2x10^{-5} allowing ~ μW power levels to be demonstrated. This was achieved without the use of plasmonic effects, nor any kind of an antenna, nor an applied E-field to the structure. Tuneable THz emission from 0.2-6 THz is assumed from the width of the excitonic transitions.

This THz wave source is then used successfully to demonstrate transmission spectroscopy of atmospheric features at 750 GHz. This work opens prospects for new future swept-wavelength THz spectroscopy systems in the THz region.

Dedicated to my Family

Acknowledgements

This thesis would not have been as comprehensive without the guidance, support, and collaboration of many people.

First and foremost, I would like to extend my sincere thanks to my supervisor Professor Richard Hogg for his enthusiastic help; without his insight, guidance and support, this work would not have been as comprehensive or complete.

I would also like to give special thanks to my supervisor Professor Geraint Jewell, for all the support and encouragement he provided me with during the last two years, support that has undoubtedly been essential in helping me to overcome the many difficulties involved in completing this project.

Many thanks go to Professor Osamu Kojima and Dr. Pavlo Ivanov for stimulating discussions on mutual research interests.

I would also like to express my sincere appreciation to the University of Sheffield and the EPSRC National Centre for III-V Technologies for offering me this precious opportunity to conduct my research here, and for facilitating the entire process. Thanks go to Dr. David Childs for advice on characterisation and setup design, and to Dr. Nasser Babazadeh, Dr. Ken Kennedy and Saurabh Kumar for their advice on device fabrication. Thanks to Dr. Edmund Clarks for growing the sample and showing me the growth procedure steps, and to Professor John David and Dr. Kris Groom for letting me use some of their experiment apertures to conduct specific measurements.

Next, I would like to thank all my colleagues, particularly, Zhou, Xiao, Kristof, Negin, Noura, Amilia, Hifsa, Siming, Omar, Richard, Soroush, Ian, Tim, Brett, Alfred, Wei, Razvan and Graham, for helping to make my PhD journey enjoyable.

I gratefully acknowledge the financial support for my studentship from the Kurdistan Ministry of Higher Education and Scientific Research (Kurdistan).

Last but not least, I would like to express my deepest gratitude to my family for their endless love and support. Thank you to my beloved husband Dr. Fahmi Raza for his unconditional support, understanding and love, you were and always will be my bedrock and my greatest support. Special thanks and kisses to my angels Nvar and Viar for bringing so much happiness in my life: I appreciate your understanding during these years.

Presentation & Publications

- **A. N. Majeed**, P. Ivanov, D. T. D. Childs, E. Clarke, O. Kojima and R. A. Hogg. "Substrate Removal and Capillary Bonding of a Quantum Beat Sample". 8th UK-Europe-China Workshop on mm-Waves and THz Technologies, UCMMT, UK- Cardiff, September. 2015. **(Oral presentation)**.

- **A. N. Majeed**, B. Stevens, P. Ivanov, D. T. D. Childs, E. Clarke, N. Babazadeh, O. Kojima and R. A. Hogg. "Room Temperature Generation of THz Waves Using 2nd Order Non-Linear Excitonic Effects With CW Excitation of GaAs/AlGaAs Multi-Quantum Well Structures". UK Semiconductor Conference, UK-Sheffield, June 2016. **(Oral presentation)**.

- **A. N. Majeed**, B. Stevens, P. Ivanov, D. T. D. Childs, E. Clarke, N. Babazadeh, O. Kojima and R. A. Hogg. "Room Temperature Generation of THz wave using 2^{nd} Order Non-Linear Effect with CW Excitation of GaAs/AlAs Multi-Quantum Wells". 70th Workshop*:* Terahertz Science*,* Nanotechnology and application, Italy-Sicily, July 2016. (**EPL best presentation award**).

- **A. N. Majeed**, B. Stevens, P. Ivanov, D. T. D. Childs, E. Clarke, N. Babazadeh, O. Kojima and R. A. Hogg. "THz wave generation through 2nd order non-linear excitonic effects in GaAs/AlAs MQWs at room temperature". SPIE Photonics West, USA, San Francisco, February 2017. (**Oral presentation**).

- **A. N. Majeed**, P. Ivanov, B. J. Stevens, E. Clarke, D. T. D. Childs, O. Kojima, R. A. Hogg. "Tuneable THz Generation Using 2nd Order Non-Linear Optical Effects in GaAs/AlAs Multi-Quantum Well Excitons at Room Temperature". Optical Terahertz Science and Technology, OTST, UK-London, April 2017. (**Poster presentation**).

- **A. N. Majeed**, P. Ivanov, B. J. Stevens, E. Clarke, D. T. D. Childs, O. Kojima, R. A. Hogg. "Room Temperature Tuneable THz Generation Based On 2nd Order Non-Linear Optical Effects in GaAs/AlAs Multi-Quantum Well Excitons". CLEO/EUROPE- EQEC 2017, Germany-Munich, June 2017. (**Poster presentation**).

- **A. N. Majeed** , P. Ivanov, B. J. Stevens, E. Clarke, D. T. D. Childs, O. Kojima, R. A. Hogg. " Room Temperature Tuneable THz Generation Based On 2nd Order Non-Linear Optical Effects in GaAs/AlGaAs Multi-Quantum Well Excitons". Infrared and Millimeter Waves, International Conference IRMMW, Mexico- Cancun, August 2017. (**Keynote Talk**).

- **A. N. Majeed**, P. Ivanov, B. Stevens, E. Clarks, D.T.D. Childs, O. Kojima and R. A. Hogg. "Efficient Tuneable THz Wave Emission From 2nd Order Non-Linear Optical Effects in GaAs/AlGaAs Multi-Quantum Well Excitons At Room Temperature". UCMMT, UK- Liverpool, September 2017. (**Invited talk**).

- **A. N. Majeed**, P. Ivanov, B. Stevens, E. Clarks, I. M. E. Butler, D.T.D. Childs, O. Kojima and R. A. Hogg. **"**Towards Swept Source Spectroscopy Using THz Emission From 2nd - Order Nonlinear Optical Effects in GaAs/AlGaAs Multi-Quantum Well Excitons at Room Temperature". SPIE Photonics West, USA, San Francisco, February 2018. (**Oral presentation**).

- **A. N. Majeed**, P. Ivanov, D. T. D. Childs, E. Clarke, O. Kojima and R. A. Hogg. "Substrate Removal and Capillary Bonding of a Quantum Beat Sample". Proc. Millim. Waves THz Technol. Work. UCMMT, 2015-8th UK, Eur. China. 6–8.

- **A. N. Majeed**, P. Ivanov, B. Stevens, E. Clarke, I. M. E. Butler, D. T. D. Childs, O. Kojima and R. A. Hogg. "Broadband THz Absorption Spectrometer Based on Excitonic Non-Linear Optical Effects". Submitted to light: Science & Applications-Nature.

List of contents

Chapter One

Introduction

1.1 Introduction

This chapter includes a brief overview of the THz radiation gap. Then, some of the most attractive applications of THz radiation are briefly explored, paying special attention to the applications of THz in spectroscopy. The motivation for this work is highlighted and the outline of the thesis is detailed.

1.2 THz Radiation 'gap'

Terahertz is the term used to denote the spectrum of frequencies ranging from 0.3-10 THz [1]. This band of frequencies lying between the microwave and infrared regions is in between the regions of the electro-magnetic spectrum usually associated with electronics and photonics, as shown in Fig.1.1. Traditionally, this region of the spectrum has been ill-served in terms of the availability of suitable sources.

THz wave research received particular attention at the beginning of 1990s, and although some applications have been established for THz waves, a lot of research still needs to be done on the supporting the research of THz applications, as well as in producing efficient emitters and detectors. Until recently, therefore, this area in the electromagnetic spectrum was referred to as the 'THz gap' [2], and applications in the THz region were much less extensively investigated and developed than those for microwave and infrared light.

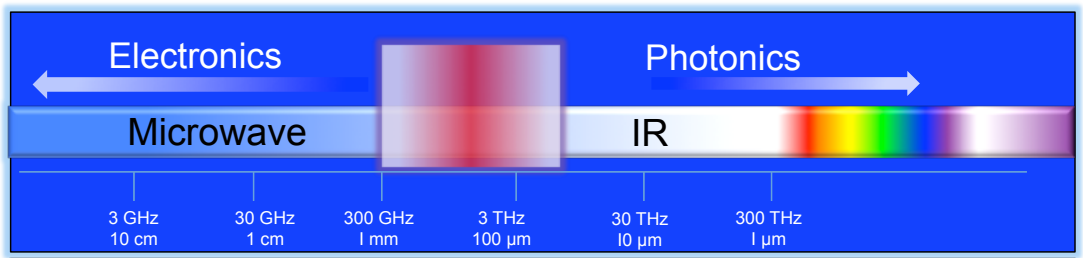

Figure 1.1 The terahertz gap in the frequency range between 300 GHz (0.3 THz) and 10 THz

1.3 THz Main Applications

THz radiation has unique properties, which potentially open the way to an extensive range of applications, especially for imaging microscopic objects and in spectroscopic application. The following outlines some of these applications:

- **Quality Control**

In contrast to the microwave range, THz waves have a shorter wavelength and higher energy, enable them to penetrate deeper and provide a higher resolution and sharper images. Furthermore, compared to the optical wavelengths, THz can penetrate through non-polar, non-metallic and dry materials such as plastic, paper and clothes, meanwhile metal is opaque to the THz frequency range, thereby providing the required contrast for imaging. Since THz is non-ionizing radiation, this combination of properties means that it is very attractive for use instead of x-rays for non-destructive scanning in order to investigate the contents of sealed packages. Furthermore, chemical composition can be determined non-destructively throughout manufacture [3–5]. Since THz radiation is very sensitive to water, it can also be used to precisely detect the water content in moisture sensitive goods [6].

- **Biology and Biomedical**

The sensitivity of THz to moisture means that it could be used to measure the water contents in some plants, for example measuring the leaf water grade for a transpiring plant [7] .

THz is also very attractive for use in biomedical applications [8], as it has low photon energy and therefore is not ionizing. This, in combination with its sensitivity to water, means that THz can be used to examine hydration in contexts such as the investigation of burn depth and severity, examining the tissues near to the surface

(since it will not penetrate deeply due to water absorption) and for determining the normality of the biological system such as the detection of skin [9, 10], breast [11], and some other kinds of cancer [12, 13] (see Fig. 1.2).

Since the proportional of water is different in cancer cells as compared to healthy cells, also it could be used for tooth imaging [14], and some other biological tissues [15, 16].

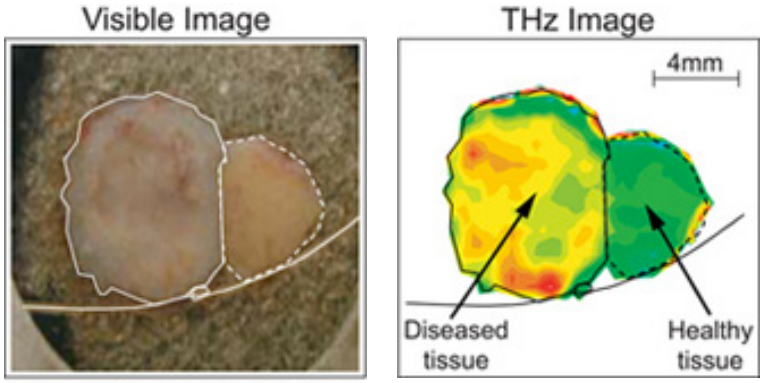

Figure 1.2 Biomedical terahertz imaging (Diagnosis of basal cell carcinoma) Images courtesy of TeraView Ltd. [17]

- **Security Checks**

Since plastics, polymers and paper are all transparent to THz radiation, it has many potential security applications, being able to detect hidden objects (as shown in Fig. 1.3) [18, 19], and hidden explosives [18, 20]. It is therefore now used in airport security checking.

Figure 1.3 Terahertz image of a man with a hidden knife, adapted from [19]

- **Material Characterization**

THz also has an interesting application in the characterization of different kinds of materials, such as semiconductors, polymer films and lightweight molecules. THz radiation can be used to measure the carrier concentration and to investigate the parameters of superconducting materials. Specifically, THz spectroscopy is already being used to evaluate various properties of semiconductor wafers, such as their mobility, carrier density and plasma oscillation [21, 22].

Moreover, THz has been used to inspect foam insulation and detect defects caused by air bubbles in materials like the external foam coating the space shuttle [23].

They are many other applications for THz radiation as it has been used widely in wireless communications since it has the benefit of a high data rate performance [24], especially for communication in rural areas and for communicating between buildings during a disaster. Another application is to monitor the environment of the earth, such as in the NASA Aura satellite, which monitors chemical species of

different gases, clouds and ice in the atmosphere, as well as measuring the temperature [25].

1.4 THz Detector

THz detection methods are classified into two main categories: direct and indirect.

Direct detection mechanisms include detector types that are directly affected by an incident THz beam, such as where the beam initiates a change in temperature. Some examples of direct detectors include bolometers cooled to cryogenic temperatures [26], pyroelectric detectors that exploit the properties of a pyroelectrical material, where a change in temperature is induced by a spontaneous electric field [27, 28], Goly cells, where a chamber is filled with a small volume of gas that is very sensitive to the absorbed heat that is introduced by the THz radiation [28], and photoconductive switches that are sensitive to the current induced by the beam [29]. This kind of detector is able to respond to THz radiation throughout a wide range of frequencies, but this response is relatively slower than with indirect detectors.

Indirect detection mechanisms are based on the concept that THz waves generated by light can be converted and detected as an optical light. These methods are dependent on Electro-Optical (EO) techniques [28, 30, 31], in which a non-linear crystal and photodiode sensor is used to observe the indirect changes of the THz beam on a probing laser beam. This detection technique is noise sensitive and there is a trade-off between the frequency response and the noise sensitivity related to the choice of crystal and its thickness [32].

1.5 Motivation and Objectives of The Research Work

The spectroscopic potential of THz radiation has been described above, with a wide range of present and possible industrial, biological, medical and security applications. Current THz spectroscopic solutions are bulky and expensive, and there is therefore a need to develop a THz spectrometer system that is low cost, compact and portable, while being widely tuneable across the THz spectrum and able to operate at room temperature. As part of this endeavour, my PhD was focused on developing THz sources for use in such a system that can be operated efficiently using commercial semiconductor laser systems at room temperature.

To this end, a novel sample was designed to explore quantum beating when illuminated by two CW lasers as an optical excitation source. The thesis describes the design rules for the sample structure, its optical/electronic characterization, and the resulting THz measurements. Initial experimental results led us to select different approaches tailored to producing widely tuneable THz emissions at room temperature and based on different frequencies.

To achieve the above overall aim, the research work was divided into five specific objectives, each with its own work stage.

The first stage was to develop the sample design. First, the transition energy in the structure was calculated to ensure that the sample was designed to emit electromagnetic waves within the THz frequency range. Next, the opto-electronic properties of the sample structure were studied using a mesa diode developed for this task. Specifically, photoluminescence and photocurrent were studied to ensure that the structural qualities matched those necessary for the design.

In the second stage the sample was prepared to ensure that it was able to absorb the maximum amount of energy from the laser, while minimizing the extent of THz

absorption (i.e. so that THz was emitted efficiently rather than being absorbed). This was achieved by using techniques such as wet etching and polishing to remove the cap layer and substrate, and in order to support the sample during the etching process, it was attached to diamond/glass by means of capillary bonding [33]. A copper disc with a hole in the centre were designed and used to hold the sample suspended on the diamond wafer.

Preliminary THz measurements were carried out in the third stage and it was accordingly confirmed that the sample was able to emit radiation in the THz range through the difference frequency generation method.

The fourth stage focused on more in-depth measurements to confirm that the device could be adjusted to tune the THz emissions, with the THz wavelength being measured using an etalon interferometer.

In the final stage the practical application of the novel THz source was assessed. A continuous wave spectrometer was realized to study the attenuation of the emitted THz radiation in the atmosphere. To this end, a spectrometer system was set up and tests performed at room temperature. This enabled us to propose the development of a complete THz spectrometer system based on the novel device created in this research.

1.6 Organization of Thesis

This thesis includes eight chapters explaining the work undertaken.

- **Chapter 1**

Presents a brief background of the THz gap, and highlights the wide range of applications for THz radiation, along with the techniques to detect THz radiation, the

gaps in current knowledge, and thus the motivation for the contributions presented in this thesis.

- **Chapter 2**

Sets out the detail of the present methods for THz generation, classified into three categories according to how they operate.

- **Chapter 3**

Explains the design rules and characterizes the opto-electronic properties of the sample design, demonstrating that the quality of the growth sample by MBE matched the initial design.

- **Chapter 4**

Describes the steps followed to develop the sample, and to prepare it for THz measurements.

- **Chapter 5**

Shows the proposed setup of the THz emission system, along with the characterization of the lasers. It also investigates the absorption through the sample after the preparation processes, and presents preliminary results for the THz emissions.

- **Chapter 6**

Describes the updated setup consisting of the etalon interferometer, and more detailed THz measurement results. Three different wavelength measurements are produced and the origin of THz generation is explained and the results discussed.

- **Chapter 7**

Demonstrates the potential application of the THz generated by the sample in spectroscopy by calculating the attenuation of THz radiation through the atmosphere as well as measuring this experimentally in our laboratory.

- **Chapter 8**

Concludes the project by summarizing its major findings and achievements and discussing future work that might build on this research.

References

1. Williams, B.S.: Terahertz quantum-cascade lasers. Nat Phot. 1, 517–525 (2007).

2. Sirtori, C.: Applied physics: Bridge for the terahertz gap. Nature. 417, 132–133 (2002).

3. Brinkmann, S., Vieweg, N., Gärtner, G., Plew, P., Deninger, A.: Towards quality control in pharmaceutical packaging: Screening folded boxes for package inserts. J. Infrared, Millimeter, Terahertz Waves. 38, 339–346 (2017).

4. Nidhi, K., Indrajeet, S., Khushboo, M., Gauri, K., Sen, D.J.: Hydrotropy: A promising tool for solubility enhancement: A review. Int. J. Drug Dev. Res. 3, 26–33 (2011).

5. Ung, B.S.-Y., Fischer, B.M., Ng, B.W.-H., Abbott, D.: Towards quality control of food using terahertz. Proc. SPIE. 6799, 67991E–67991E–4 (2007).

6. Federici, J.F.: Review of moisture and liquid detection and mapping using Terahertz imaging. J. Infrared, Millimeter, Terahertz Waves. 33, 97–126 (2012).

7. Mittleman, D.M., Jacobsen, R.H., Nuss, M.C.: T-Ray Imaging. 2, 679–692 (1996).

8. Siegel, P.H.: Terahertz technology in biology and medicine. IEEE Trans. Microw. Theory Tech. 52, 2438–2447 (2004).

9. Woodward, R.M., Cole, B.E., Wallace, V.P.V.P., Arnone, R.J.P.D.D., Linfield, E.H., Pepper, M., Pye, R.J., Arnone, D.D., Linfield, E.H., Pepper, M.: Terahertz Pulse imaging in Reflection Geometry of Human Skin Cancer and Skin Tissue. Phys. Med. Biol. 47, 3853–3863 (2002).

10. Woodward, R.M., Wallace, V.P., Arnone, D.D., Linfield, E.H., Pepper, M.: Terahertz pulsed imaging of skin cancer in the time and frequency domain. J Biol Phys. 29, 257–259 (2003).

11. Ashworth, P.C., Pickwell-MacPherson, E., Provenzano, E., Pinder, S.E., Purushotham, A.D., Pepper, M., Wallace, V.P.: Terahertz pulsed spectroscopy of freshly excised human breast cancer. Opt. Express. 17, 12444 (2009).

12. Brun, M.A., Formanek, F., Yasuda, A., Sekine, M., Ando, N., Eishii, Y.: Terahertz imaging applied to cancer diagnosis. Phys Med Biol. 55, 4615–4623 (2010).

13. Yu, C., Fan, S., Sun, Y., Pickwell-Macpherson, E.: The potential of terahertz imaging for cancer diagnosis: A review of investigations to date. Quant. Imaging Med. Surg. 2, 33–45 (2012).

14. Pickwell, E., Wallace, V.P.: Biomedical applications of terahertz technology. J. Phys. D. Appl. Phys. 39, R301–R310 (2006).

15. Pickwell, E., Cole, B.E., Fitzgerald, A.J., Pepper, M., Wallace, V.P.: *In vivo* study of human skin using pulsed terahertz radiation. Phys. Med. Biol. 49, 1595–1607 (2004).

16. Markelz, A.G.: Terahertz dielectric sensitivity to biomolecular structure and function. IEEE J. Sel. Top. Quantum Electron. 14, 180–190 (2008).

17. Terahertz Detection Of Skin, Mouth And Epithelial Cancers, http://www.teraview.com/applications/medical/oncology.html.

18. Federici, J.F., Schulkin, B., Huang, F., Gary, D., Barat, R., Oliveira, F., Zimdars, D.: THz imaging and sensing for security applications—explosives, weapons and drugs. Semicond. Sci. Technol. 20, S266–S280 (2005).

19. Vidhi Sharma, D.A. and M.J.: Terahertz Technology and its Applications. 5th IEEE Int. Conf. Adv. Comput. Commun. Technol. 175–178 (2014).

20. Tribe, W.R., Newnham, D.A., Taday, P.F., Kemp, M.C.: Hidden object detection: security applications of terahertz technology. Proc. SPIE. 5354, 168–176 (2004).

21. Nashima, S., Morikawa, O., Takata, K., Hangyo, M.: Temperature dependence of optical and electronic properties of moderately doped silicon at terahertz frequencies. J. Appl. Phys. 90, 837–842 (2001).

22. Mittleman, D.M., Cunningham, J., Nuss, M.C., Geva, M.: Noncontact semiconductor wafer characterization with the terahertz Hall effect. Appl. Phys. Lett. 71, 16–18 (1997).

23. Zimdars, D., Valdmanis, J.A., White, J.S., Stuk, G., Williamson, S., Winfree, W.P., Madaras, E.I.: Technology and applications of terahertz imaging non-destructive examination: Inspection of space shuttle sprayed on foam insulation. AIP Conf. Proc. 760, 570–577 (2005).

24. Koenig, S., Lopez-Diaz, D., Antes, J., Boes, F., Henneberger, R., Leuther, A., Tessmann, A., Schmogrow, R., Hillerkuss, D., Palmer, R., Zwick, T., Koos, C., Freude, W., Ambacher, O., Leuthold, J., Kallfass, I.: Wireless sub-THz communication system with high data rate. Nat. Photonics. 7, 977–981 (2013).

25. Waters, J.W., Froidevaux, L., Harwood, R.S., Jarnot, R.F., Pickett, H.M., Read, W.G., Siegel, P.H., Cofield, R.E., Filipiak, M.J., Flower, D.A., Holden, J.R., Lau, G.K., Livesey, N.J., Manney, G.L., Pumphrey, H.C., Santee, M.L., Wu, D.L., Cuddy, D.T., Lay, R.R., Loo, M.S., Perun, V.S., Schwartz, M.J., Stek, P.C., Thurstans, R.P., Boyles, M.A., Chandra, K.M., Chavez, M.C., Chen, G.S., Chudasama, B. V., Dodge, R., Fuller, R.A., Girard, M.A., Jiang, J.H., Jiang, Y., Knosp, B.W., Labelle, R.C., Lam, J.C., Lee, K.A., Miller, D., Oswald, J.E., Patel, N.C., Pukala, D.M., Quintero, O., Scaff, D.M., Van Snyder, W., Tope, M.C., Wagner, P.A., Walch, M.J.: The Earth Observing System Microwave Limb Sounder (EOS MLS) on the aura satellite. IEEE Trans. Geosci. Remote Sens. 44, 1075–1092 (2006).

26. Richards, P.L.: Bolometers for infrared and millimeter waves Bolometers for infrared and millimeter waves. 1, 1–24 (1994).

27. Sergey Ganichev, W.P.: Intense Terahertz Excitation of Semiconductors. Oxford University Press, Oxford, UK (2006).

28. Lee, Y.-S.: Principles of Terahertz Science and Technology. Springer, New York, U.S.A (2009).

29. Saeedkia, D. ed: Handbook of Terahertz Technology for Imaging, Sensing and Communications. Woodhead Puplishing (2013).

30. Winnewisser, C., Jepsen, P.U., Schall, M., Schyja, V., Helm, H., Winnewisser, C., Jepsen, P.U., Schall, M., Schyja, V., Helm, H.: Electro-optic detection of THz radiation in. 3069, 10–13 (2011).

31. Yin, Xiaoxia, Ng, Brian, Abbott, D.: Terahertz Imaging for Biomedical Applications. Springer, New York (2012).

32. Cai, Y., Brener, I., Lopata, J., Wynn, J., Pfeiffer, L.: Coherent terahertz radiation detection : Direct comparison between free-space electro-optic sampling and antenna detection Coherent terahertz radiation detection : Direct comparison between free-space electro-optic sampling and antenna detection. 444, 73–76 (2011).

33. Majeed, A.N., Ivanov, P., Childs, D.T.D., Clarke, E., Hogg, R.A.: Substrate Removal and Capillary Bonding of a Quantum Beat Sample. Millim. Waves THz Technol. Work. (UCMMT), 2015 8th UK, Eur. China. 6–8.

Chapter Two

Overview of Terahertz Radiation Sources

2.1 Introduction

This chapter includes an overview of the main techniques for THz generation, classified into three main categories according to their mode of operation. The advantages and disadvantages of each technique are explored and highlighted. Through discussing these features the chapter concludes that laser-driven THz emission sources are the most attractive for generating tuneable THz waves at room temperature.

2.2 THz Emission Sources

THz emission sources are generally divided into three main categories based on the physics of their methods of THz generation; namely, electronic, laser and optically driven sources, as illustrated in Fig. 2.1. This section will give a brief general description of some of these techniques for generating THz emissions, focusing on the laser-driven techniques, since the device proposed in this thesis can be classified as a laser-driven THz generation technique.

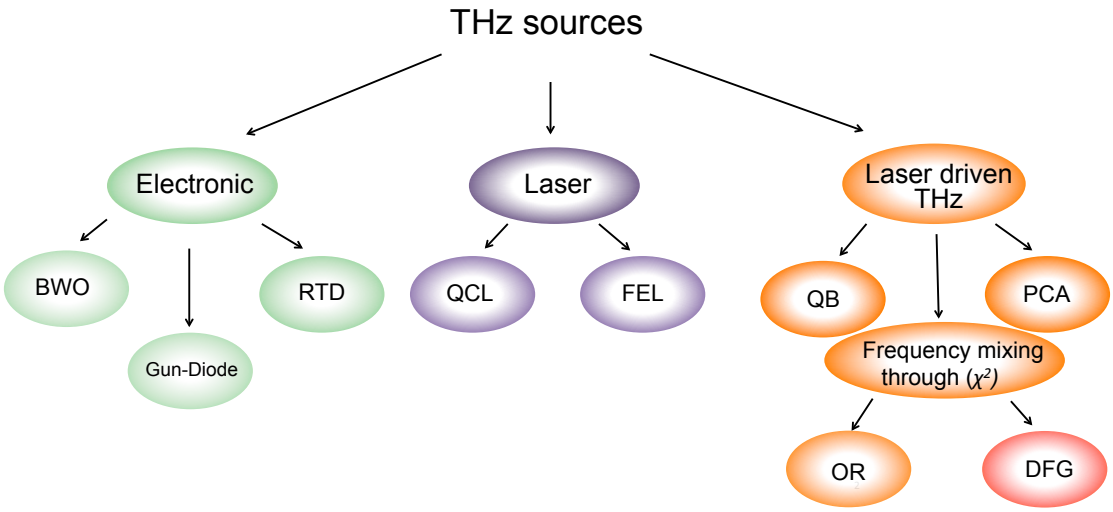

Figure 2.1 Flow diagram of the main mechanisms for THz generation

2.2.1 Electronic Devices

Backward-Wave Oscillator (BWO)

This is an electron vacuum diode that is able to produce CW, narrow band, tuneable and high power (up to tens of mW) THz radiation [1, 2]. Fig. 2.2 shows the schematic diagram of the BWO device, the electron is emitted from the heated cathode, and by applying DC electric field the electron is accelerated towards the

anode. The device is positioned in a permanent magnet to collimate the electron beam. The electrons deliver above a comb-like fine metallic structure, in which the electrons velocity are modulated and also grouped in bunches with the presences of charges and electric field. Because of this acceleration, the electrons excite and sustain an electromagnetic wave (travelling in opposite direction to the electron beam direction), then this radiation exits the source via an oversized waveguide coupled to the cavity. The velocity of the electrons determine the frequency of the radiation, therefore the frequency could be tuned with adjusting the bias voltage [3, 4].

BWO is one of the THz sources that have been used for spectroscopic measurements [5, 6], covering a frequency range of 0.3 to 1.3 THz [7]. This THz radiation source, however, has only limited tuneabilty, meaning that many BWOs have to be applied in order to generate a wide range of THz emissions.

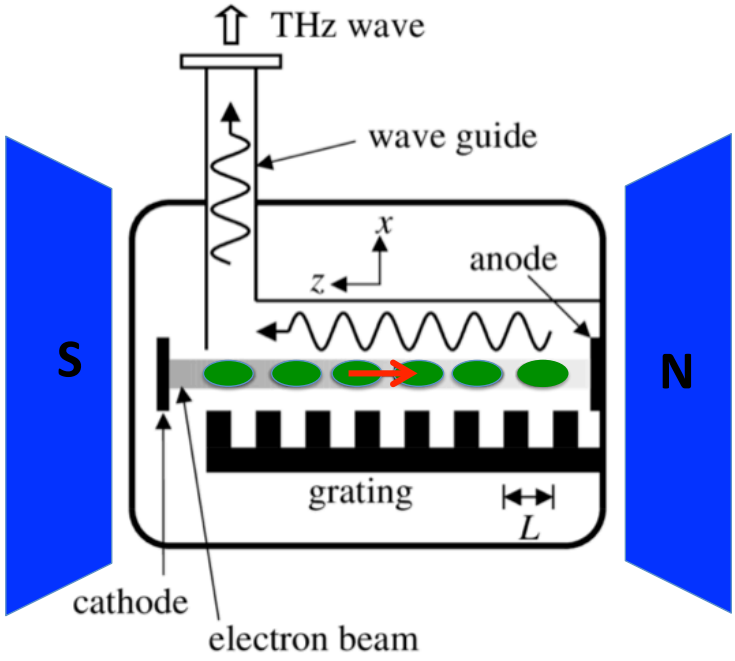

Figure 2.2 Schematic diagram of backward wave oscillator, adapted from [3]

It is also heavy and expensive, and needs a strong magnetic field in addition to a vacuum system.

Gunn Diode

Gunn diodes are two-terminal negative differential resistance (NDR) electronic devices; generate electromagnetic wave when it is coupled to an appropriately tuned AC resonator. The typical device structure of a Gunn diode involves a uniform doped n-type layer of III-V material (such as GaAs, InP) inserted between heavily doped regions at each terminal. Fig. 2.3 shows the band structure of the GaAs, the lowest conduction band has distinct valleys in certain orientations, as they labelled Γ and L. If the electrons exist in the lower Γ- valley, then they display a small effective mass and also high mobility, while the electrons have a large effective mass and low mobility in the L-valley. A very small energy gap separated the two valleys (ΔE) [8].

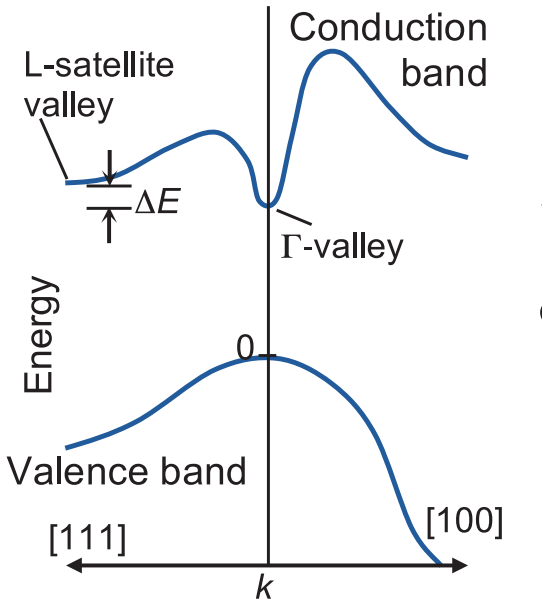

Figure 2.3 GaAs band structure, adapted from [8]

The external bias is applied across the diode; when the bias reaches a certain threshold value, the electrons gain adequate energy to transfer to the L-valley, where their mobility decreases as a result of an increase of their effective mass, because of that, the conduction current through the Gunn diode decreases as appeared, the curve in the region 2 (area in blue) shown in Fig. 2.4, and the diode exhibits a region of NDR (region spanning from peak point to valley point) in the V-I characteristic curve. This effect is called transferred electron effect and thus the Gunn diodes are also called transferred electron devices [8].

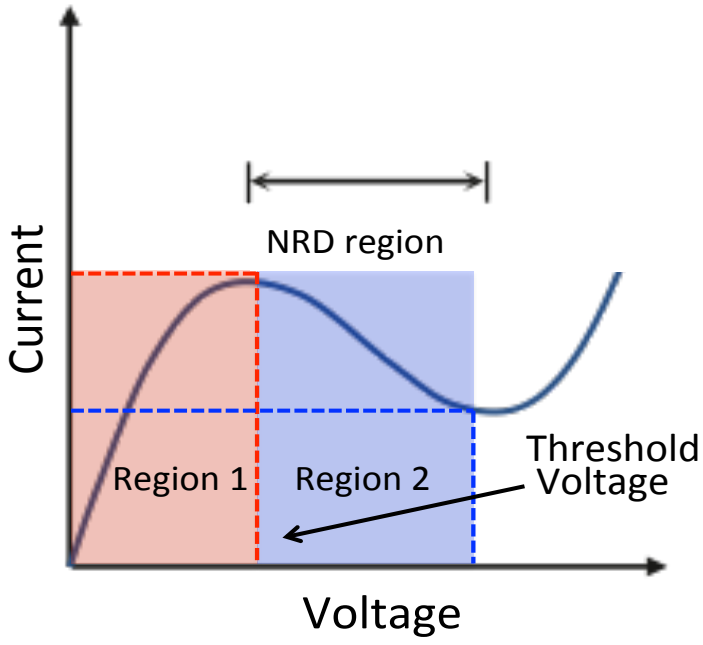

Figure 2.4 V-I characterization of Gunn diode, adapted from [8]

When the diode is connected to a cavity or resonant circuit, the resistance of the resonator is cancelled by the negative resistance, this cancellation of resistance result in circuit oscillates without attenuation and emits electromagnetic radiation.

The average output power in the THz frequency ≈ several tens of μW [9]. The power; however, decreases rapidly as the THz frequency increases [10].

Resonant Tunnelling Diode (RTD)

RTDs are a resonant-tunnelling structure where electrons can tunnel through some resonant states at certain energy levels. Fig. 2.5 illustrates the structure of an RTD, which is made up of two hetero barriers (large band gap material) and a quantum well. An emitter region works as a source of electrons and a collector region collects the electron tunnelling across the hetero barriers [11]. Resonant tunnelling happens at specific resonant energy levels consistent to the doping levels and width of the quantum well.

The current–voltage (I–V) curve includes peaks at which the resonance level in the quantum well is nearby to the conduction band edge of the device. A bias voltage is required and increasing the applied voltage leads to a rapid drop in the current. As a result, the resonance level falls below the emitter conduction band edge and the current-voltage (I-V) curve of the diode exhibits a negative differential conductance region [12, 13].

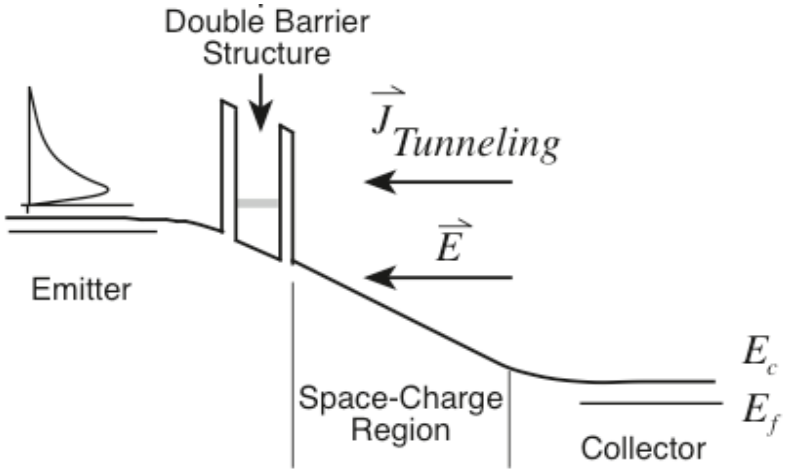

Figure 2.5 RTD structure with applied forward bias, adapted from [11]

Although it has low power, as well as limited frequency up to 2 THz at low level powers, compared to the others emitters [14, 15], it is still attractive for use in communication applications.

2.2.2 Laser Sources

Free-Electron Laser (FEL)

FEL feature high intensity electron and is a high power THz emitter ≈ several watts [12]. The gain medium in the free-electron laser consists of an electron beam that moves spontaneously through a periodic magnetic structure (wiggler period), this modulated the electron periodically, the electron shows a harmonic oscillation around the cavity and this oscillation emit electromagnetic wave. It has the widest tuneable wavelength range (0.12- 4.75 THz) [7], which covers the spectrum from microwaves to X-rays. The drawback of this emitter, however, is its complexity of operation and its huge dimensions. It is therefore only available in some large universities and academic research institutes [16] .

Quantum Cascade Lasers (QCL)

Quantum cascade lasers (QCLs) are made up of coupled quantum wells. The term ‘cascading’ refers to the repetitive nature of the multiple intersubband transitions that are required in order to achieve electromagnetic emissions, either in the mid-infrared or THz frequency range. The first QCL was developed in 1994, with frequency lasing in the mid-infrared region of about 70 THz [17].

As shown in Fig. 2.6, the cascaded structure of each period is made up of an undoped active region and an n-doped relaxation/injection region.

By 2002, frequency lasing at 4.4 THz had been demonstrated [18]. The disadvantages of QCLs are that the device needs to be cooled to no more than 199.5 K in pulsed mode [19], and the THz spectra cannot be tuned.

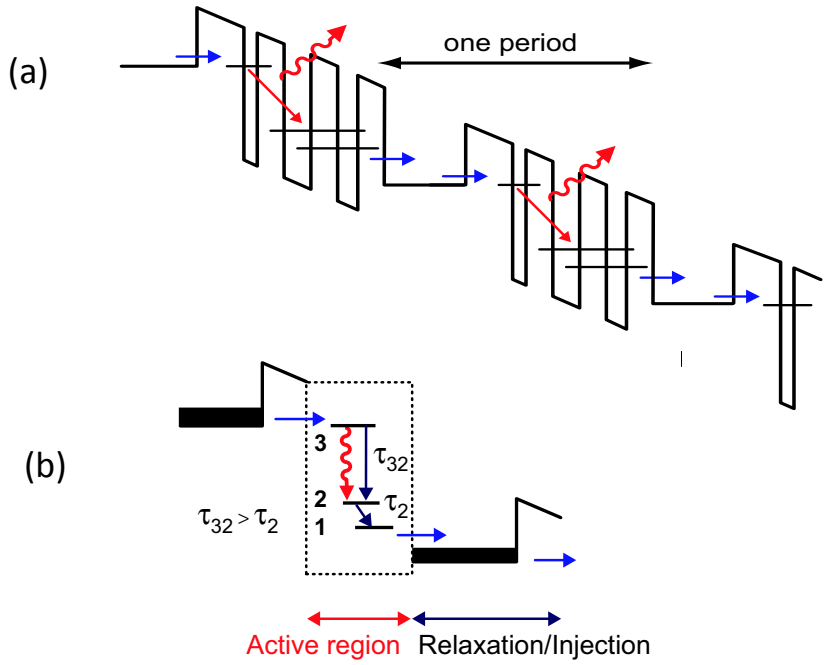

Figure 2.6 (a) Schematic diagram of the conduction band of a quantum cascade laser. Two periods are shown in the diagram, with each period of the cascade structure containing an active region and a relaxation/injection region, (b) Schematic diagram of a single period in the structure, showing how the active region is a three-level unipolar system, and how the lifetime of the 3 → 2 transition should be longer than the lifetime of level 2 if population inversion is to be obtained. Adapted from [20] The blue arrows represent the incident laser and wavy red arrows the electron flow

To overcome these challenges, however, an alternative mechanism can exploit the advances in high power mixing of two colour mid-infrared QCLs at room temperature to provide intracavity THz by difference frequency generation [21, 22]. This methodology is not powerful compared to THz QCL, however, and there remain some limitations [7].

2.2.3 Laser Driven THz Sources

Photoconductive Switches and Photomixing

Photoconductive antennae (PCA) can be used to generate and detect THz waves. These are constructed from a semiconductor substrate with DC biased metal electrodes located on top of the surface that can be incorporated into the generation of pulsed and continuous wave THz.

Fig. 2.7 shows a schematic diagram of the PCA and the photomixer. In both cases, a photoconductor is used, but the physical mechanism that underlies THz pulse generation in PCA is initiated by means of an ultrafast laser pulse at a photon energy ($h\upsilon$) larger than energy gap [23], while two CW laser are used in the photomixing techniques [24]. The photon energy can be determined in accordance with the properties of a semiconductor material, which is used as an emitter that changes the material's conductivity and generates electron–hole pairs in the photoconductor.

Applying a DC biased voltage accelerates the carrier, causing electrons and holes to flow in a certain direction. This process produces a transient current. Since short-period pulse laser energy rapidly changes, this also rapidly changes the number of electron and holes, thereby causing the current intensity to vary. This generates a time-varying electric field with an associated electromagnetic spectrum.

In the CW mode, meanwhile, two tuneable laser beams that produce different frequencies in the THz range are combined into an optical fibre or in space, then mixed in a photo-absorbing medium (photomixer) [25].

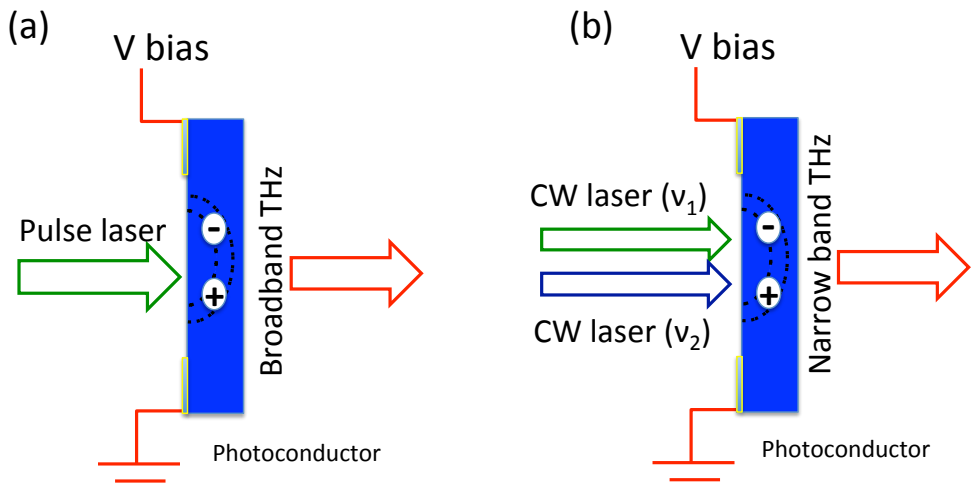

Figure 2.7 Schematic diagram side view of (a) PCA, (b) photomixer in which two lasers with slightly difference laser wavelengths illuminate the surface of the photoconductor

These methods lack long-term stability and scalability, however, and also have low conversion efficiencies from the optical to the THz regime [20]. Furthermore, they have a fundamental limitation of being relatively low power due to thermal failure of the device when high power lasers are applied [26]. Nonetheless, they have been widely used in spectroscopic applications [27, 28].

Quantum Beat (QB)

In a quantum well, the quantum beat can be defined by excitonic polarization interference produced by light hole (LH) and heavy hole (HH) excited states [29]. In a semiconductor quantum well, meanwhile, the confinement energy in the growth direction lifts the degeneracy between the heavy hole and light hole due to their different effective masses. Thus the quantum beat is achieved by applying a coherent excitation of HH and LH with a pulse width wide enough to cover both transition energies, causing oscillation in the optical response which leads to charge oscillation at the HH-LH splitting frequency, producing polarization in the system, Furthermore, for these two-level systems, the polarization interference can be

oscillated in a period corresponding to the inverse of the energy transitions (i.e. in the THz range) [29]. Tuneable THz 1.4-2.6 at 10 K, THz was achieved by increasing the applied electric field [30].

Nonlinear Frequency Mixing Through χ^2

Laser interaction with nonlinear optical materials leads to nonlinear responses in properties like frequency, polarization, phase or path of the incident light. These nonlinear interaction processes cause a host of optical phenomena that can be exploited for THz generation [10]. The most common phenomena used for THz generation in non-centrosymmetric materials, are optical rectification and different frequency generation. In contrast to photoconduction, the output THz wave power is related to the second-order nonlinear coefficient of the material, meaning that it does not have the upper limit voltage characteristics, and the output power is not limited by the optical damage threshold of the material [26].

- **Optical Rectification (OR)**

This kind of the THz generation method requires excitation with an ultrafast laser. It is a non-linear optical process (i.e. a second order nonlinear phenomenon) in which an intense laser pulse with a broad-spectrum and different frequency components, interacts with an electro-optic nonlinear crystal producing DC polarization [31]. When a laser beam consisting of ultra-short pulses passes via a non-linear electro-optic crystal, the driving electric field leads the atom to produce an oscillating dipole moment, resulting in electromagnetic wave radiation. This phenomena can be exploited to generate a broadband electromagnetic wave in the THz frequency range [32]. The power efficiency of the THz radiation generated using this method relies on the second order nonlinear coefficient and the condition

of the phase matching [33]. This method has, however, been used in combination with E-O sampling to demonstrate a THz spectroscopy system [34].

- **Difference Frequency Generation**

Difference frequency generation (DFG) is a second-order nonlinear optical process in which two optical beams, at ω_1 and ω_2, interact simultaneously with a nonlinear crystal, causing a narrowband electromagnetic wave to be generated along with a new photon at a frequency of ω_3 ($\omega_3 = \omega_1 - \omega_2$), as shown in Fig 2.8 (a). This process can give rise to intense coherent radiation in the infrared range. The fundamental of the DFG can be seen from the energy level in Fig. 2.8 (b), since the DFG production is accompanied by the amplification of one of input fields at the expense of the other. For this reason, DFG is often referred to as optical parametric amplification; furthermore, the process works at room temperature.

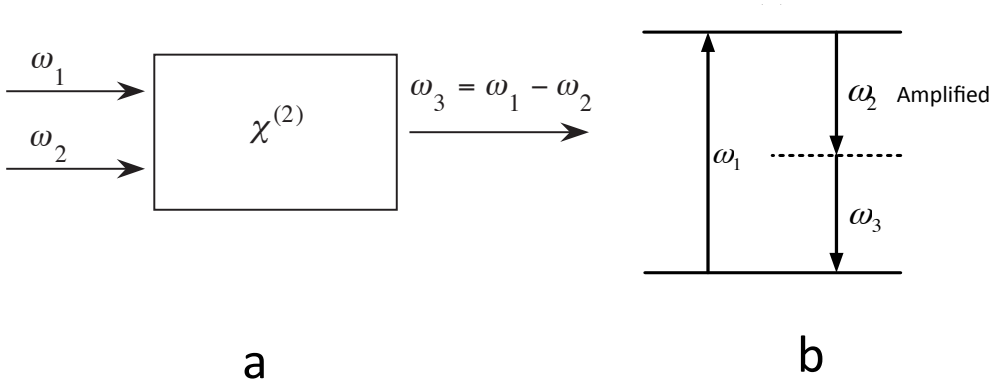

Figure 2.8 (a) Schematic illustration of the difference-frequency generation process, (b) Energy-level diagram of difference-frequency generation

Using DFG to generate THz is attracting increasing attention because of the lack of efficient, CW, tuneable and powerful THz sources working at room temperature [8]. Different nonlinear crystals have therefore been examined and used to generate THz; among them, GaSe, GaAs, quartz, $LiNbO_3$, GaP and DAST (4-dimethylamino-N-methyl-4-sibazolium-tosylate) [35–38], among all of these, the GaSe and GaAs were found to be the most promising materials for demonstrating THz emission through DFG, as they have large second-order nonlinear coefficients χ^2 (d=54 pm/V, and 47 pm/V for GaSe and GaAs, respectively). Phase matching is achievable between the optical pump at the range of the infrared wavelength [3], and a widely tuneable THz can be produced. Furthermore, it has a low linear absorption coefficient in the THz frequency range [39, 40], as illustrated in Fig. 2.9. Furthermore, the spectral feature (such as a line width) of THz generation by DFG is in respect to the feature of the pump lasers these are used for the excitation.

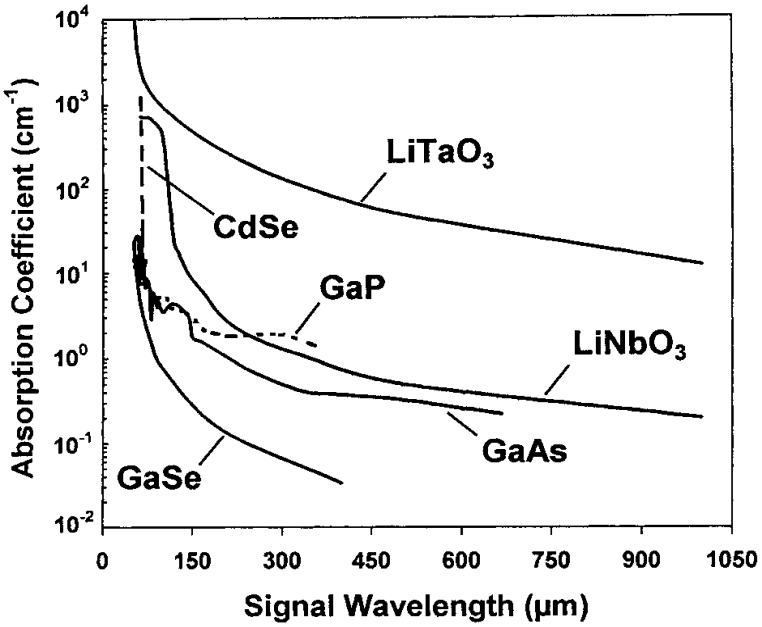

Figure 2.9 Absorption coefficients for different materials within the THz radiation range, re-printed from [3]

The following parameters are therefore advantageous for laser beams [33] .

- Narrow laser beam linewidths and a single longitudinal mode, since the DFG emission linewidth is equal to the convolution of the pump laser linewidths under Gaussian beam profile fitting.
- A wide range of wavelength tuneability since this produces a widely tuneable THz range.
- A high power laser is required in order to generate significant levels of THz since the THz wave power is quadratically dependent on the laser power.

Table 2.1 summarise the performance of source technologies and the drawbacks of each technique [3, 7, 41, 42].

Electronic Sources				
Devices	**Mode Operation**	**Max. Power**	**THz Tuneability**	**Drawbacks**
BWO	Narrow CW	Tens of mW (up 1.45 THz)	0.3 to 1.3 THz	• Bulky • Magnetic field is required for operation
RTD	CW	0.3 mW at (0.712 THz)	Limited frequency up to 2 THz	• Operated at low temperature • Limited tuneability
Gunn diode	CW	FEW microwatt>1.9THz		• Operated at low temperature
Laser Sources				
Devices	**Mode operation**	**Max. Power**	**THz Tuneability**	**Drawbacks**
FEL	CW	Several hundred watts	0.12- 4.75 THz	• Complexity of operation • Bulky
QCL	CW/PULSE	139 mW (CW) at 10K / 248 mW (pulsed) at 77K	1–5 THz	• Operated at low temperature
Laser driven THz Sources				
Devices	**Mode Operation**	**Optical to THz Conversion Efficiency**	**THz Tuneability**	**Drawbacks**
QB	CW		1.4 - 2.6 THz at 10K	• Operated at low temperature
PCA/PM	Pulse/CW	$\approx 10^{-6}$-10^{-5}	0.05 - 6 THz	• Very low Power as it is limited to the thermal damage of the emitter
OR	Pulse	$\leq 10^{-4}$	Wide range of tuneability	• Relatively low power
DFG	`Narrow CW	$\leq 10^{-6}$	Wide range of tuneability	• Relatively low power

Table 2.1 THz sources performance and their drawbacks

2.3 The THz Spectroscopy System

Due to the advantages of THz radiation (as described in detail in section 1.3) THz-time domain spectroscopy (THz-TDS) has many advantages over the other wavelengths of light used for spectroscopic applications, and is also able to provide better spectral resolution than other spectroscopy systems like Fourier transform spectroscopy (FTS).

Terahertz spectroscopy is attractive for material characterization in both industry and medical sectors. Different types of spectroscopy are classified based on the mechanism of THz generation, detection, THz spectral features, and the method that is used to characterize the sample, and some of these systems, are explained in this section.

2.3.1 THz Time Domain Spectroscopy THz-TDS

Time domain spectroscopy is based on using an ultra-short pulse laser, <100 fs, in order to generate short pulses of broadband THz. Usually, the same kind of devices are used for generating and detecting the THz radiation, and either PCA or optical rectification combined with (electro-optic) EO crystal are used [34, 43]. Fig. 2.10 illustrates a typical TH-TDS system, here using an ultra-fast laser pulse which is then split by means of beam splitter into a pump and probe beam. The pump beam is then incident onto the THz emitter in order to emit THz pulses.

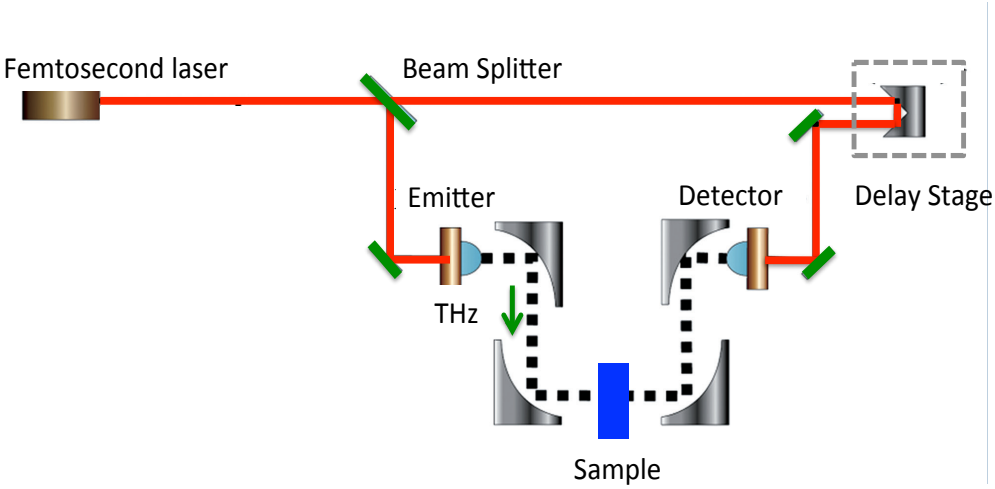

Figure 2.10 Schematic diagram of THz –TDS

Since the generated THz is expected to be divergent (not well directed), parabolic mirrors are used to collimate and focus the THz radiation onto the detector. Additionally the probe beam is used to gate the detector and measure the THz electric field. Moreover, a delay stage is used to offset the two beams (probe and pump), permitting the THz temporal profile to be iteratively sampled.

Since this technique was first established in 1980, the THz-TDS approach has been widely used in different aspects of materials characterization and imaging systems, such as, medicine, cancer diagnosing, and biology and biomedical applications. These THz-TDS systems have three major drawbacks, however [7, 42].

1. High cost (several thousand pounds) since femtosecond pulse lasers are needed, which are expensive.

2. The mechanical delay stages (an essential part in the system) are slow at long travel distances, therefore it this kind of system is not appropriate to measure thick material layers at high sampling rates.

3. The spectral resolution is not high ≈ 1 GHz [44] .

2.3.2 Continuous Wave THz Spectroscopy

Continuous wave THz systems consist of narrowband continuous tuneable THz sources. Different detectors can be used in the system. In addition, although most of the narrowband tuneable THz sources can be used in this system, the laser-driven THz sources are preferable to the electronic sources since the latter have low frequency tuning ranges, making it difficult to measure thin layers (≈ 1 μm) [42]. Continuous wave THz systems have the advantage of a high signal-to-noise ratio (SNR), high spectral resolution [45], fast scanning rate, and are also considered more affordable that the THz-TDS since the CW laser sources (excitation sources) are commercially available at a low price. Taken together, this means that CW THz systems are more attractive for use in imaging systems, and also, due to their resolution and tuneability, very attractive for the spectroscopy of gases [44]. The photomixer has been widely used as a detector and emitter for this system [45] and, among the other THz wave generation methods, DFG is considered very attractive for continuous wave THz spectroscopy, since with this method, a single frequency, widely tuneable THz range can be generated, and it provides a higher signal to noise ratio (SNR) and spectral resolution [42].

References

1. Dobroiu, A., Yamashita, M., Ohshima, Y.N., Morita, Y., Otani, C., Kawase, K.: Terahertz imaging system based on a backward-wave oscillator. Appl. Opt. 43, 5637 (2004).

2. Gorshunov, B.P., Volkov, A.A., Prokhorov, A.S., Spektor, I.E.: Methods of terahertz-subterahertz BWO spectroscopy of conducting materials. Phys. Solid State. 50, 2001–2012 (2008).

3. Lee, Y.-S.: Principles of Terahertz Science and Technology. Springer, New York, U.S.A (2009).

4. Van Slageren, J., Vongtragool, S., Gorshunov, B., Mukhin, A.A., Karl, N., Krzystek, J., Telser, J., Müller, A., Sangregorio, C., Gatteschi, D.: Frequency-domain magnetic resonance spectroscopy of molecular magnetic materials. Phys. Chem. Chem. Phys. 5, 3837–3843 (2003).

5. Lewen, F., Gendriesch, R., Pak, I., Paveliev, D.G., Hepp, M., Schieder, R., Winnewisser, G.: Phase locked backward wave oscillator pulsed beam spectrometer in the submillimeter wave range. Rev. Sci. Instrum. 69, 32–9 (1998).

6. Dressel, M., Drichko, N., Gorshunov, B., Pimenov, A.: THz spectroscopy of superconductors. IEEE J. Sel. Top. Quantum Electron. 14, 399–406 (2008).

7. Dhillon, S.S., Vitiello, M.S., Linfield, E.H., Davies, A.G., Hoffmann, M.C., Booske, J., Paoloni, C., Gensch, M., Weightman, P., Williams, G.P., Castro-Camus, E., Cumming, D.R.S., Simoens, F., Escorcia-Carranza, I., Grant, J., Lucyszyn, S., Kuwata-Gonokami, M., Konishi, K., Koch, M., Schmuttenmaer, C.A., Cocker, T.L., Huber, R., Markelz, A.G., Taylor, Z.D., Wallace, V.P., Axel Zeitler, J., Sibik, J., Korter, T.M., Ellison, B., Rea, S., Goldsmith, P., Cooper, K.B., Appleby, R., Pardo, D., Huggard, P.G., Krozer, V., Shams, H., Fice, M., Renaud, C., Seeds, A., Stöhr, A., Naftaly, M., Ridler, N., Clarke, R., Cunningham, J.E., Johnston, M.B.: The 2017 terahertz science and technology roadmap. J. Phys. D. Appl. Phys. 50, 43001 (2017).

8. O'Sullivan, C.M.M., Murphy, J.A.: Field guide to terahertz sources, detectors,

and optics. SPIE (2012).

9. Gunn, J.B.: Instabilities of Current in III–V Semiconductors. IBM J. Res. Dev. 8, 141–159 (1964).

10. Kitaeva, G.K.: Terahertz generation by means of optical lasers. Laser Phys. Lett. 5, 559–576 (2008).

11. York, R.: Schottky-collector Resonant Tunnel Diodes for Sub-Millimeter-Wave Applications. 229 (1997).

12. Gold, S.H., Nusinovich, G.S.: Review of high-power microwave source research. Rev. Sci. Instrum. 68, 3945–3974 (1997).

13. Asada, M., Suzuki, S., Kishimoto, N.: Resonant tunneling diodes for sub-terahertz and terahertz oscillators. Jpn. J. Appl. Phys. 47, 4375–4384 (2008).

14. Sinha, R., Karabiyik, M., Al-Amin, C., Vabbina, P.K., Güney, D.Ö., Pala, N.: Tunable Room Temperature THz Sources Based on Nonlinear Mixing in a Hybrid Optical and THz Micro-Ring Resonator. Sci. Rep. 5, 9422 (2015).

15. Maekawa, T., Kanaya, H., Suzuki, S., Asada, M.: Oscillation up to 1.92 THz in resonant tunneling diode by reduced conduction loss. Appl. Phys. Express. 9, 24101 (2016).

16. Yin, Xiaoxia, Ng, Brian, Abbott, D.: Terahertz Imaging for Biomedical Applications. Springer, New York (2012).

17. Faist, J., Capasso, F., Sivco, D.L., Sirtori, C., Hutchinson, A.L., Cho, A.Y.: Quantum cascade laser. Science (80). 264, 553–555 (1994).

18. Köhler, R., Tredicucci, A., Beltram, F., Beere, H.E., Linfield, E.H., Davies, A.G., Ritchie, D.A., Iotti, R.C., Rossi, F.: Terahertz semiconductor-heterostructure laser. Nature. 417, 156–159 (2002).

19. Saeed Fathololoumi, Emmanuel Dupont, Ivan C. Chan, Zbigniew R. Wasilewski, Sylvain R. Laframboise, Dayan Ban, Alpar Matyas, Christian Jirauschek, Qing Hu, and H.L.: 199.5 K Operation of THz Quantum Cascade Lasers. OSA Tech. Dig. (Optical Soc. Am. , Pap. CTu2B.1. (2012).

20. Faist, J., Capasso, F., Sivco, D.L., Hutchinson, A.L., Sirtori, C., Cho, A.Y.: Quantum cascade laser: A new optical source in the mid-infrared. Infrared Phys. Technol. 36, 99–103 (1995).

21. Belkin, M.A., Capasso, F.: New frontiers in quantum cascade lasers: high performance room temperature terahertz sources. Phys. Scr. 90, 118002 (2015).

22. Lu, Q.Y., Bandyopadhyay, N., Slivken, S., Bai, Y., Razeghi, M.: Widely tuned room temperature terahertz quantum cascade laser sources based on difference-frequency generation. Appl. Phys. Lett. 101, (2012).

23. Smith, P.R., Auston, D.H., Nuss, M.C.: Subpicosecond Photoconducting Dipole Antennas. IEEE J. Quantum Electron. 24, 255–260 (1988).

24. Brown, E.R., Smith, F.W., McIntosh, K.A.: Coherent millimeter-wave generation by heterodyne conversion in low-temperature-grown GaAs photoconductors. J. Appl. Phys. 73, 1480–1484 (1993).

25. Pliński, E.: Terahertz photomixer. Bull. Polish Acad. Sci. Tech. Sci. 58, 463–470 (2010).

26. Verghese, S.: Highly tunable fiber-coupled photomixers with coherent terahertz output power. IEEE Trans. Microw. Theory Tech. 45, 1301–1309 (1997).

27. Shen, Y.C., Upadhya, P.C., Beere, H.E., Linfield, E.H., Davies, A.G., Gregory, I.S., Baker, C., Tribe, W.R., Evans, M.J.: Generation and detection of ultrabroadband terahertz radiation using photoconductive emitters and receivers. Appl. Phys. Lett. 85, 164–166 (2004).

28. Shen, Y.: Terahertz Time-Domain Spectroscopy and Imaging. J. Electr. Electron. Syst. 3, 2–3 (2014).

29. Leo, K., Damen, T.C., Shah, J., Göbel, E.O., Köhler, K.: Quantum beats of light hole and heavy hole excitons in quantum wells. Appl. Phys. Lett. 57, 19–21 (1990).

30. Planken, P.C.M., Nuss, M.C., Brener, I., Goossen, K.W., Luo, M.S.C.,

Chuang, S.L., Pfeiffer, L.: Terahertz emission in single quantum wells after coherent optical excitation of light hole and heavy hole excitons. Phys. Rev. Lett. 69, 3800–3803 (1992).

31. Qi, J.: Nonlinear Optical Spectroscopy of Gallium Arsenide Interfaces. 211 (1995).

32. Rice, A., Jin, Y., Ma, X.F., Zhang, X.-C., Bliss, D., Larkin, J., Alexander, M.: Terahertz optical rectification from (110) zinc blende crystals. Appl. Phys. Lett. 64, 1324–1326 (1994).

33. Dragoman, D., Dragoman, M.: Terahertz fields and applications. Prog. Quantum Electron. 28, 1–66 (2004).

34. Nahata, A., Weling, A.S., Heinz, T.F.: A wideband coherent terahertz spectroscopy system using optical rectification and electro-optic sampling. Appl. Phys. Lett. 69, 2321–2323 (1996).

35. Shi, W., Ding, Y.J., Fernelius, N., Vodopyanov, K.: Efficient, tunable, and coherent 0.18--5.27-THz source based on GaSe crystal. Opt. Lett. 27, 1454–1456 (2002).

36. Ding, Y.J.: High-power tunable terahertz sources based on parametric processes and applications. IEEE J. Sel. Top. Quantum Electron. 13, 705–720 (2007).

37. Tanabe, T., Suto, K., Nishizawa, J., Saito, K., Kimura, T.: Tunable terahertz wave generation in the 3-to 7-THz region from GaP. Appl. Phys. Lett. 83, 237–239 (2003).

38. Satoh, T., Toya, Y., Yamamoto, S., Shimura, T., Kuroda, K., Takahashi, Y., Yoshimura, M., Mori, Y., Sasaki, T., Ashihara, S.: Generation of mid- to far-infrared ultrashort pulses in 4-dimethylamino-N-methyl-4-stilbazolium tosylate crystal. J. Opt. Soc. Am. B. 27, 2507–2511 (2010).

39. Ding, Y.J., Zotova, I.B.: Second-order nonlinear optical materials for efficient generation and amplification of temporally-coherent and narrow-linewidth terahertz waves. Opt. Quantum Electron. 32, 531–552 (2000).

40. Träger, F.: Handbook of Lasers and Optics. Springer, New York (2007).

41. Ung, B.S.: Novel hardware for terahertz time-domain spectroscopy by. (2013).

42. Nagatsuma, T.: Terahertz technologies: Present and future. IEICE Electron. Express. 8, 1127–1142 (2011).

43. Jepsen, P.U., Jacobsen, R.H., Keiding, S.R.: Generation and detection of terahertz pulses from biased semiconductor antennas. J. Opt. Soc. Am. B. 13, 2424 (1996).

44. Hindle, F., Yang, C., Mouret, G., Cuisset, A., Bocquet, R., Lampin, J.F., Blary, K., Peytavit, E., Akalin, T., Ducournau, G.: Recent developments of an opto-electronic THz spectrometer for high-resolution spectroscopy. Sensors. 9, 9039–9057 (2009).

45. Deninger, A., Roggenbuck, A., Schindler, S., Mayorga, I.C., Schmitz, H., Hemberger, J., Gusten, R., Gruninger, M.: Cw THz spectrometer with high SNR and MHz frequency resolution. 34th Int. Conf. Infrared, Millimeter, Terahertz Waves, IRMMW-THz 2009. 1–2 (2009).

Chapter Three

Sample Design, Manufacture, and Characterization

3.1 Introduction

This chapter includes the following: an introduction to the design of the sample, highlighting the main points in its structure and design rules; an introduction to the molecular beam epitaxy (MBE) as the technique used to grow the sample; a discussion of the optical prosperities of the sample, as measured by photoluminescence spectroscopy (PL); the fabrication process for the mesa diode; and the experimental setup for photocurrent measurements. Then the results are discussed in detail.

3.2 Design Rules for Sample Structure

The sample was designed to investigate the possibility of THz emissions resulting from quantum beats in electronic states in semiconductor quantum well structures under coherent optical excitation [1–3].

GaAs/AlAs was chosen for this task because it is a suitable material to realise a multiple quantum well structure (MQW). If the GaAs in the well is thicker than ≈ 3.5 nm, both the electrons and holes in the GaAs have lower energies than in the AlAs, which is defined as a "Type I" system [4].

Unlike in the bulk GaAs, the valence band of quantum wells is often split due to the different confinement energies of the light hole and heavy hole states [4–6]. Furthermore, in the quantum well, the exciton resonances are clearly observed at room temperature, since, for relatively thin layered quantum wells, and suitable well depths, the binding energy is increased as the electron-hole separation is reduced [7–9]. In addition, the energy of the optical transitions in the system can be tailored according to the geometry of the wells in the THz range, and commercially available lasers can achieve coherent excitation of the carriers.

AlAs can be grown directly on the GaAs, since their lattice constants are almost identical, as shown in Fig. 3.1 [10]. High quality GaAs/AlAs structure can be routinely manufactured either by molecular beam epitaxy (MBE) or metal-organic vapor phase epitaxy (MOVPE) [11–13]. As the MQW is made of barrier, high quality samples can be prepared, with only width fluctuations of the quantum well contributing to broadening of the optical transition.

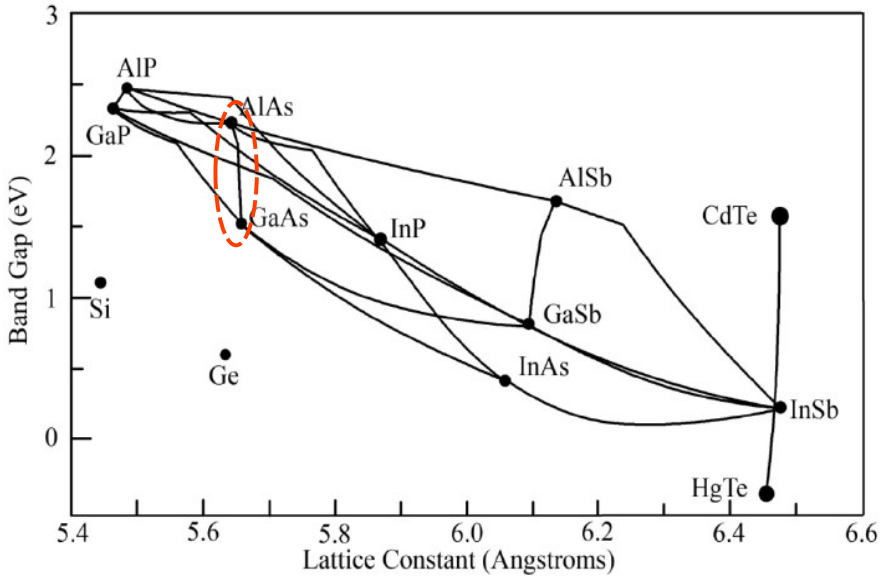

Figure 3.1 Energy gap and wavelength as a function of lattice constant for common III-V material [10]

Furthermore, the multiple quantum well structure of GaAs/AlAs has wide transparency at the THz range, a high damage threshold, and large optical nonlinearity at room temperature [7, 14].

Moreover the alloy concentration of Al is chosen to be 40% as the doped regions are transparent to the pump beams and the 40% Al layer has the largest direct band-gap of any AlGaAs alloy [15, 16]. The film quality and resilience to oxidization is expected to be good. As the material is direct band-gap, mobility is still high should the structure require efficient current flow in future [17].

In this work, the GaAs/AlAs quantum well structure is designed to utilize the heavy hole and light hole energy states. To produce a coherent excitation of E1-HH1 and E1-LH1excitons in the three level system of the quantum well, two continuous wave commercially available lasers at energies corresponding to the E1-HH1 and E1-LH1 transitions were used.

Table 3.1 presents a sample structure of the layers, which comprises a MQW structure consisting of 30 periods of 11.9 nm GaAs wells and 7.1 nm AlAs barriers. The 30 layers of GaAs are sufficient to achieve adequate optical absorption ≈ 45% of the laser sources according to the GaAs absorption coefficient at 850 nm [18].

Repeats	**Thickness**	**Material**
1	200 nm	p-GaAs
1	1500 nm	p-$Al_{0.4}Ga_{0.6}As$
1	7.1 nm	AlAs
30	11.9 nm	GaAs
30	7.1 nm	AlAs
1	1500 nm	n-$Al_{0.4}Ga_{0.6}As$
1	200 nm	n-GaAs
		n- GaAs Substrate

Table 3.1 Sample structure layers

During the sample design, MQWs are required and not a superlattice, therefore Nextnano was used to model the energy level of two quantum wells and to investigate the requirements on barrier thickness needed to separate the wells and avoid significant carrier tunnelling through the barrier. The simulation of the double quantum well shows that a 7.1 nm layer of AlAs is sufficiently thick and, since the potential barriers are high, the transition energies are almost the same in both wells,

as shown in Fig. 3.2. Since there is no wave-function penetration from one GaAs quantum well to another (given that both wells have the same energy level) the structure is defined as an MQW.

The physics of an MQW structure is the same as for a set of separate wells, therefore the simulation of a single quantum well was considered in order to calculate the transition energies.

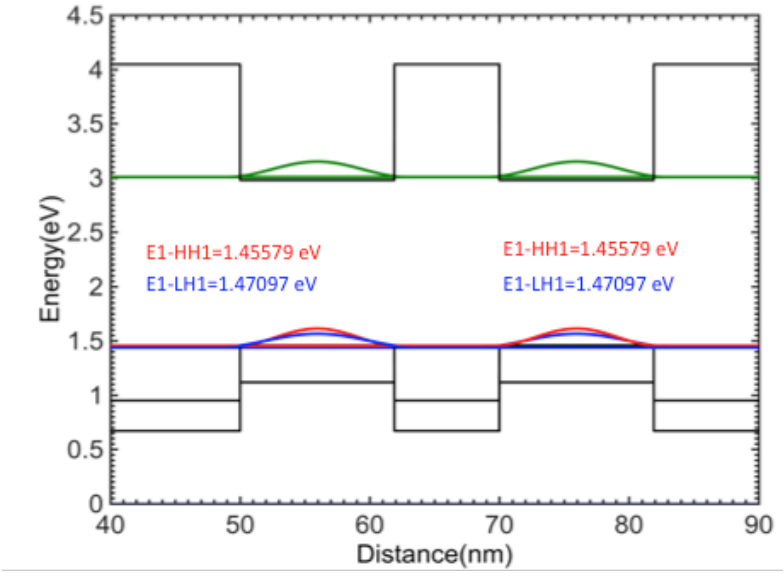

Figure 3.2 Transition diagram of the three level system of the GaAs/ALAs double quantum well with similar E1-HH1, E1-LH1 in both wells, calculated by Nextnano [16]

Fig. 3.3 shows the band structure of the three level system of a GaAs/AlAs single quantum well with E1-HH1, E1-LH1 at E = zero, calculated using Nextnano [19].

Moreover the 30 repeats of the intrinsic GaAs/AlAs multiple quantum structure were sandwiched between 1500 nm of p-n-doped $Al_{0.4}Ga_{0.6}As$ layers in order to bias the sample and apply a perpendicular external electric field, which resulted in a quantum confined Stark effect [20, 21].

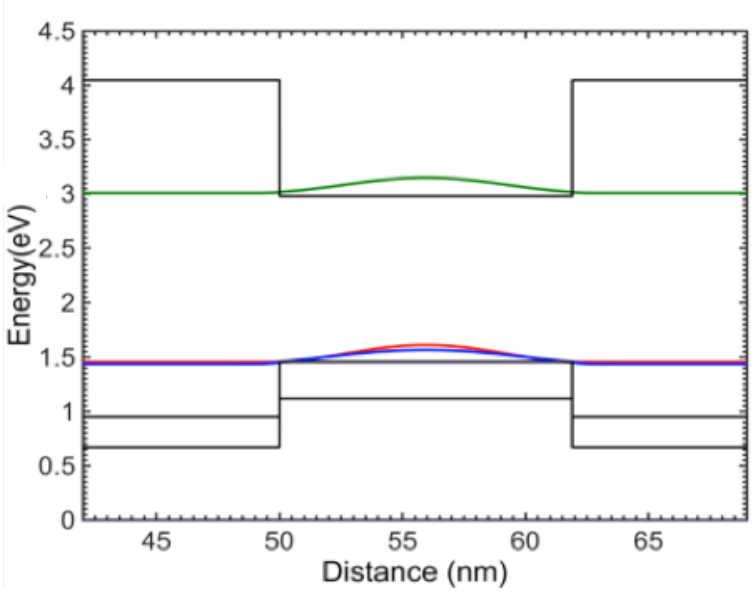

Figure 3.3 Transition diagram of three level system of the GaAs/AlAs quantum well with E1-HH1, E1- LH1, as calculated by Nextnano

Fig. 3.4 illustrates the quantum confined Stark effect in quantum wells; showing how electron and hole wave functions are affected by the electric field, E. This causes a red shift in the transition energy.

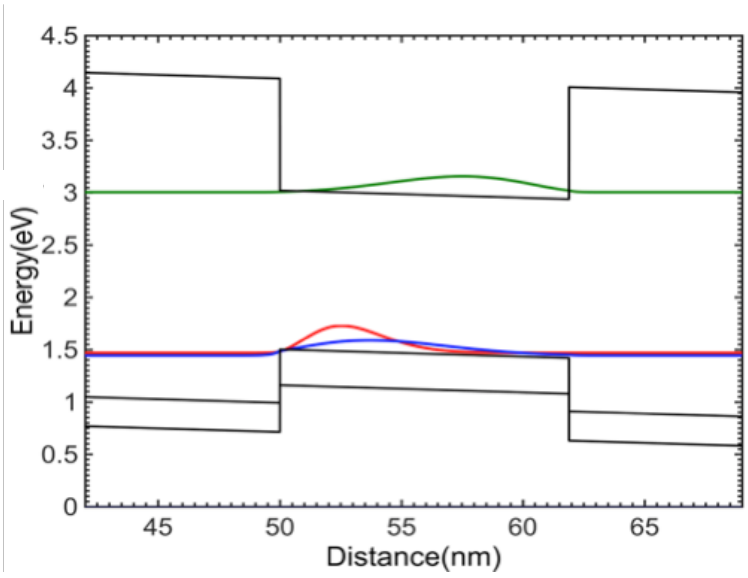

Figure 3.4 Transition diagram illustrating quantum confined Stark effect in quantum wells

Since the shift in the transition energies is not the same, this phenomenon can be employed to tune the THz frequency (as displayed in table 3.2).

Electric field (kV/cm)	E1-HH1 (eV)	E1-LH1 (eV)	Frequency (THz)
0	1.4558	1.4711	3.675
25.992	1.453	1.4697	4.03
43.32	1.4485	1.4674	4.57
60.648	1.4427	1.464	5.15
77.97	1.436	1.4598	5.75

Table 3.2 Calculated transition energy versus applied electric field using Nextnano, also shows theexpected wave frequency in THz

Furthermore, an increased electric field can be expected to increase the electron-hole wave-function separation and hence increase χ^2. However, an increased E-field, decrease electron-hole wave-function overlap and meanwhile lead to reduce the absorption, that results in reducing the THz power.

3.3 Molecular Beam Epitaxy (MBE)

Molecular beam epitaxy (MBE) is a process of growing thin, high purity epitaxial layers of different materials; it has been used widely for growing compound semiconductors since the early 1970s [22]. Because of the high degree of thickness, doping and composition control, and the ability to produce a uniform layer, it is a common growth technique used in industry for the development of optoelectronic and electric devices [23, 24].

The MBE growth technique takes place in an ultra-high vacuum system ($\approx 10^{-10}$ torr). One or more evaporated atoms or molecular beams are indicated upon a single crystal surface, which makes it capable of depositing high-quality thin epitaxial layers with very sharp interface layers [25].

MBE systems include three main chambers: a growth chamber, a buffer, which is known as a preparation chamber, and a transfer chamber, which is used to move the sample into and out of the vacuum system [23, 26]. Fig. 3.5 provides a schematic diagram of the MBE growth chambers.

The semiconductor substrate is placed on a rotating stage using a magnetically coupled transfer rod; the stage is then rotated at a fixed speed in order to produce a uniform deposition thickness over the whole of the substrate.

The atomic beams are formed in effusion cells, heated independently using a succession of heat shields. In the MBE system, the cells are located in front of the substrate holder, and at the front of each effusion cell there is a computer-controlled shutter, which is responsible for controlling the supply of material.

Although the UHV environment ensures very high quality films, the defect concentration in the substrate must be relatively low, as these affect the optoelectronic properties of the device. Two techniques can be used to ensure wafer cleanliness in the preparation chamber; Auger electron spectroscopy [27, 28], although this is not widely used because it needs more elaborate arrangements; and "epi-ready" wafers. These are a combination of pre-cleaned and oxidized thin films that form a protective layer that could be removed in the growth chamber. Epi-ready wafers are the most widely used technique at present.

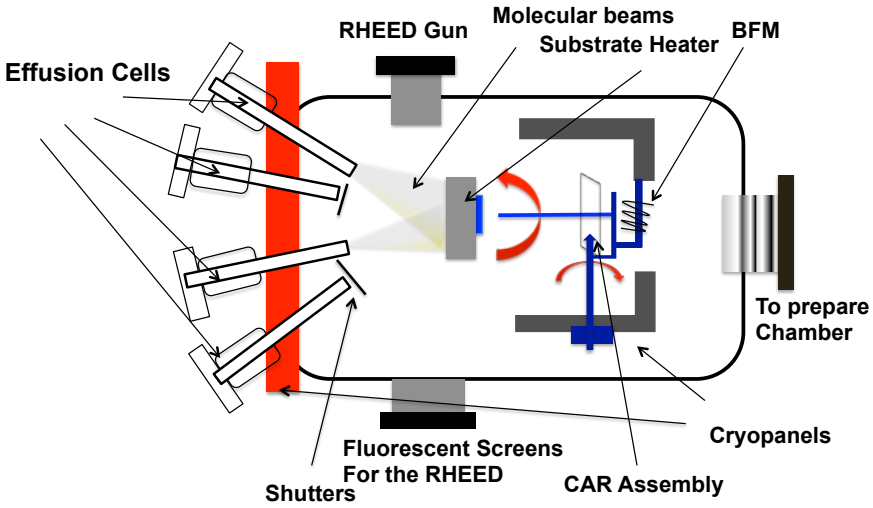

Figure 3.5 Schematic diagram of typical MBE growth chamber

The UHV environment of the system is also suitable for various in-situ characterization tools, like RHEED (reflection high energy electron diffraction), which is a very important analytical instrument used for investigations of epitaxial growth in MBE. The emitted electrons from the RHEED gun hit the sample surface at a very low angle (~1-3°) [29]. Fig. 3.5 shows how the RHEED is located on the top-side of the growth chamber, opposite a fluorescent screen. This screen creates a series of electron reflection and diffraction patterns that give detailed information about the surface crystallography.

The epitaxial layers of our structure consisted of a 200 nm n-doped GaAs ($1x10^{18}$ cm^{-3}) buffer layer deposited on an n-doped GaAs substrate, followed by 1500 nm n-doped $Al_{0.4}Ga_{0.6}As$ ($5x10^{17}$ cm^{-3}). This was followed by the deposition of the MQW, which was made up of 30 repeats of 11.9 nm un-doped GaAs quantum wells separated by 7.1 nm undoped AlAs barriers. A 1500 nm p-doped $Al_{0.4}Ga_{0.6}As$ ($5x10^{17}$ cm^{-3}) was subsequently grown. The epitaxial layer ended by growing 200 nm

p-doped GaAs ($1x10^{19}$ cm^{-3}). Fig. 3.6 shows the layered structure of the device, schematically, along with an SEM image of the device.

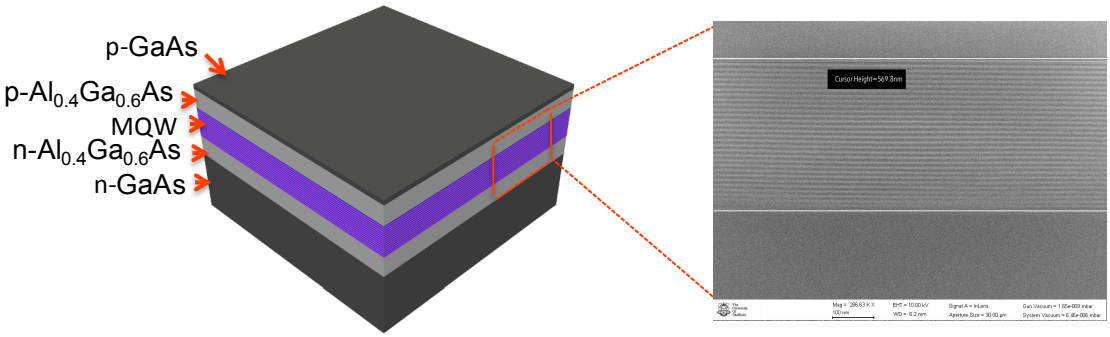

Figure 3.6 Schematic of the layered structure of the sample, and an SEM image of the MQW part of the device

3.4 Photoluminescence Spectroscopy (PL)

PL is a contactless non-destructive technique that is used widely to investigate the optoelectronic properties of semiconductor materials.

Fig. 3.7 shows (a) the light incident perpendicular to the sample surface; and (b) a schematic diagram of the PL processes. The excitation source, whose photon energy is equal to or higher than the energy gap on the material, is directed to the sample, where it is absorbed, leading to the injection of electrons in elevated states of the conduction and holes in the valence band. These rapidly relax, sinking to the bottom of the state and losing their energy by emitting phonons with a correct energy and momentum in order to satisfy the conservation laws.

After this the electron and holes can recombine radiatively, by emitting photons, or non-radiatively [30].

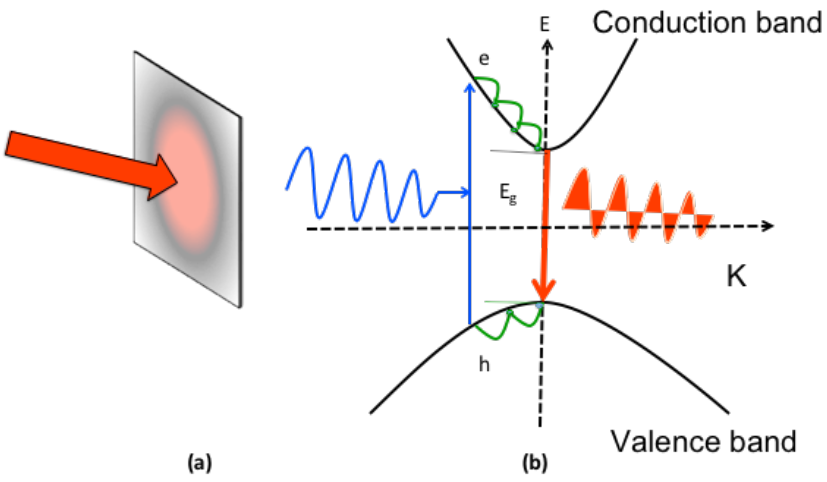

Figure 3.7 (a) Illumination of sample, (b) Absorption and recombination process during PL measurement

The photoluminescence spectra can be recorded and utilized to study the optical processes and to evaluate the quality of the surface and interface, as well as the impurity levels.

In particular, photoluminescence allows us to investigate the wafer growth conditions, and a wide variety of defects that are common in semiconductor materials. This is because the PL intensity is related to the radiative and non-radiative recombination rate, due to the fact that the impurities within the material, and the roughness between the multi-layered structure, leads to faster non-radiative recombination rate (lower PL intensity). Furthermore, a broadening of the luminescence linewidth in the spectrum could be an indication of a fluctuation in the alloy concentration across the materials [31], or a fluctuation in the well width within the excitation spot on the wafers of the quantum well structure [32, 33]. PL spectra are also widely used to study the excitonic effects in 2D structures such as QWs [34, 35].

In this research, the PL spectra were recorded at room temperature using a BIO-RAD RPM 2000 PL mapper. Fig. 3.8 shows the PL spectra of the GaAs/AlAs MQW structure, revealing a strong PL band peak at 1.455 eV, corresponding to the recombination between electrons in the first level in the conduction sub-band and holes in the heavy hole valance sub-band. Moreover, a weaker feature observed on the higher energy side of the main PL peak, near 1.467 eV, was produced by the recombination of ground state electrons and light holes.

In order to evaluate the uniformity of the structure for the entire epitaxial wafer of the PL spectra, measurements were carried out at different points along the radius of the wafer. A high spectral similarity between the measured signals is indicated away from the edge (C, D), that specify the band gap of the substrate (GaAs), in Fig. 3.8: a close match can be seen between the PL spectra peaks at points A, B.

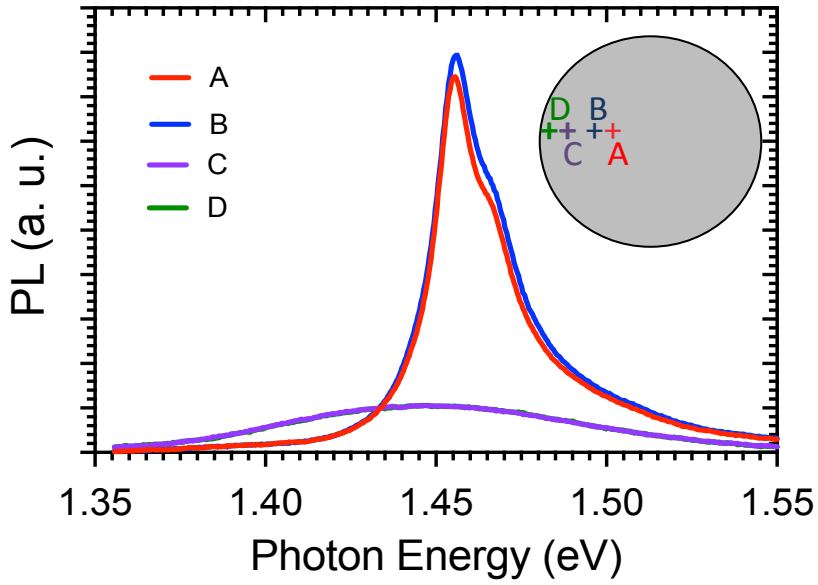

Figure 3.8 Room temperature PL spectra for the GaAs/AlAs MQW structure at different points on the wafer

Fig. 3.9 plots energy peaks of PL along different points of the wafers and inset is the schematic of the scanned area in the wafer, the results shows only a slight change in the energy peaks position of the PL spectra at all points of the wafer in the different areas examined.

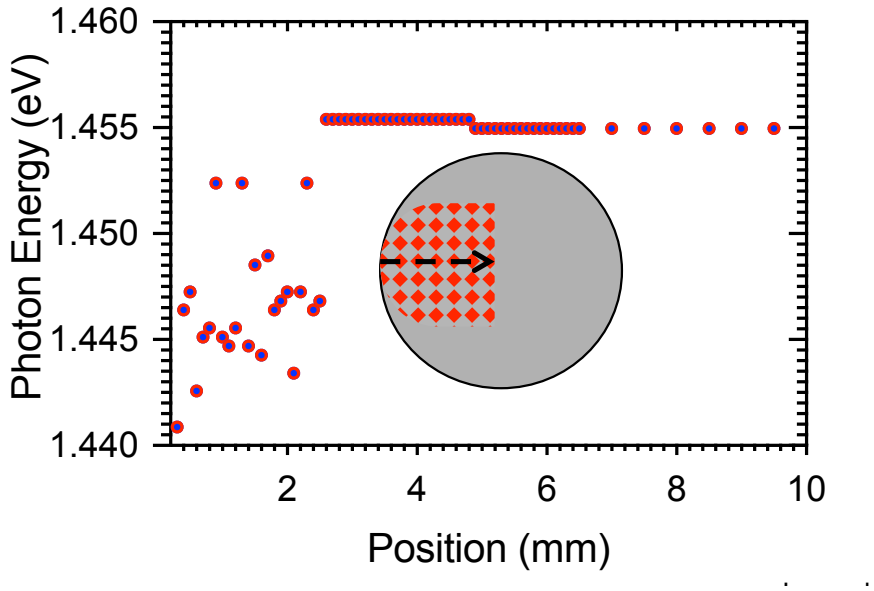

Figure 3.9 Distribution of PL spectra across a 2-inch piece of epitaxial wafer, inset is schematic of the scanned area of the wafer

This is clear evidence for a structure that is relatively highly homogenous in its optical response over the entire investigated area. This applies both to the well width and the purity of the semiconductor materials. Smaller transition peak energy values were measured at the edges of the wafer, however (points C and D in Fig 3.8), illustrating poor crystal quality near the wafer edges. Hence, none of these parts were used in any of the measurements.

3.5 Mesa Diode Fabrication

A mesa diodes were fabricated in order to observe the electrical characterization of the materials. The fabrication process used in this study was based on standard recipes.

Wafer with a diameter of 2” is scribed at the edge with a diamond tip scriber, then the piece which is required to be used for fabrication of mesa diodes is cleaned using the three step solvent cleaning process to ensure all the dust and debris are removed, Fig. 3.10 shows the piece of epitaxial structure of the wafer grown by MBE that is cleaned to be used for the mesa diode fabrication.

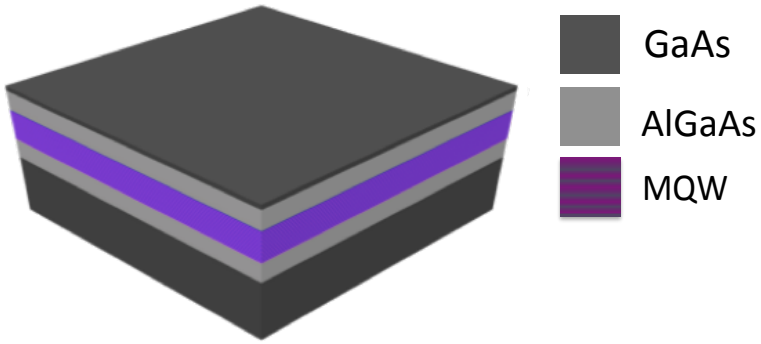

Figure 3.10 Epitaxial structure of the wafer grown by MBE

The first step of the cleaning is to put the sample into a beaker of n butyls acetate and boil it for approximately 30 seconds, after which the sample is taken out of the solvent and cleaned with cotton buds, and put into the warm acetone, then the sample is removed from the acetone to be immersed in warm isopropyl alcohol for a few seconds.

The sample is removed from the isopropyl alcohol and dried with nitrogen gas.

A microscope is used to inspect the cleanliness of the sample surface; if the sample is still not clean, then all the cleaning processes should be repeated until the sample is free of any dirt.

Once the surface has been cleaned, the sample is placed on a small piece of blue tacky paper in order to protect the backside of the sample, and it is put onto the vacuum chuck of a spinner, a photoresist named BPRS100 is dropped on the sample and then the sample is spun at 4000 rpm for 30 seconds. The next step is to put the sample on the hotplate for 1-minute to bake the photoresist. The thickness of the photoresist is non-uniform around the edge of the sample, for that reason about 1.5-2 mm must be removed. Removing the edge is carried out by masking the sample and then exposing the edge to UV for 30 seconds using aligner UV300, after which the sample is developed in 3:1 H_2O: PLSI for 1 minute, followed by rinsing in DI water and blow drying with a nitrogen gun. Fig. 3.11 shows the cleaned sample with a thin layer of photoresist on the top.

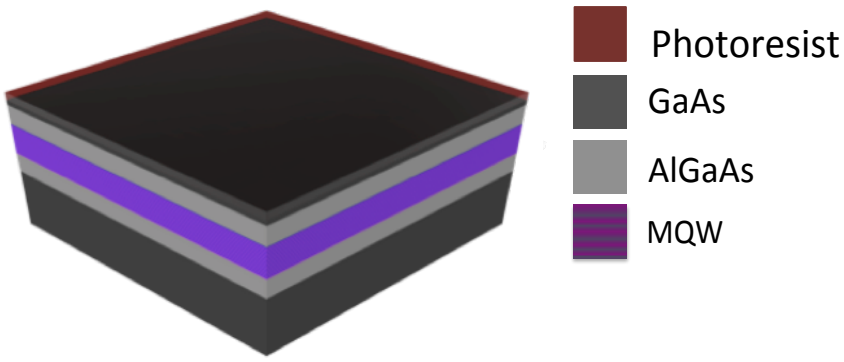

Figure 3.11 The cleaned sample with a thin layer of photoresist on the top

Then, the sample is placed on the mask aligner stage and the mask is positioned on the sample. The sample is then exposed using UV light and developed in 3:1 H2O: PLSI for 1 minute to define a pattern on the resist, and then rinsed in DI water and dried with N_2.

Fig. 3.12 shows the sample with the mesa pattern on the top, all the photolithography processes are carried out in the yellow room to ensure that the only area exposed to the UV radiation from the mask aligner is the one that has been modified.

The pattern is checked under the microscope and the sample is put in the Asher for 1 minute to make sure all the photoresist is removed in the patterned area prior to metallization.

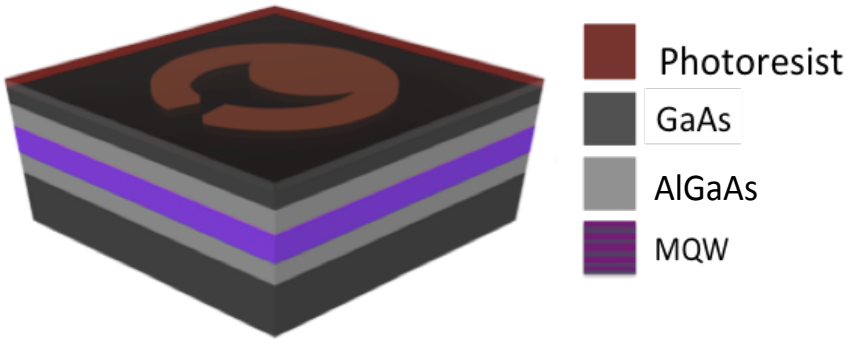

Figure 3.12 Sample after patterning on the photoresist

For the top metallization stage, a thermal evaporator is used to deposit an Au/Zn/Au metallic contact onto the front side of the device. A tungsten coil/heating element and a tungsten coil/heating basket are placed at a position of 6 cm above the crystal thickness monitor in the thermal evaporator. The tungsten coil/heating element basket is filled with ~10 mg of zinc and then gold wire is folded and cleaned with 3

stage solvents, and placed in the tungsten coil/heating element. The sample is placed in1:19 Analar Ammonia: H_2O solution for 30 seconds and dried in order to remove the surface oxide, then the sample is placed into the evaporator near to the crystal thickness monitor and just below the coils. Next the chamber is closed and a vacuum of ~10^{-6} mbar is applied. First, a thin layer of gold ~20 nm is deposited onto the sample surface to improve the adhesion of the ~10 nm zinc which is deposited after the Au layer. Finally, another ~200 nm gold layer is deposited. The thickness of each metal is measured using the crystal thickness monitor. As soon as the deposition process is finished, the sample is allowed to cool down for 10 minutes, and then taken out of the evaporator. The sample is then placed into a beaker of acetone, for the lift off processes, which dissolve the photoresist and remove any gold in unwanted areas. This is followed by inspection of the sample under the microscope. Next the sample is placed in the Asher for 2 minutes in order to remove any remaining resist; Fig. 3.13 shows the sample after the metallization, lift-off processes. Once the sample has been cleaned, it is placed in the rapid thermal annealing (RTA) system and annealed at 360^{o}C for 30 seconds in order to provide a low resistance electrical contact.

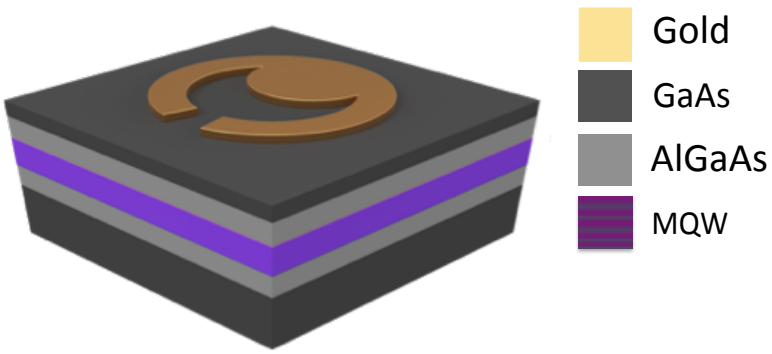

Figure 3.13 Sample after metallization, lift-off and thermal annealing procedure

Then, the sample is prepared for a wet etch step by spinning the SPR350 photoresist on top of the sample and then baking it for 1 minute. The edge bead is removed from the sample. Then, the sample is fixed and positioned on the aligner, the pattern on the surface is aligned with that of the mesa etch pattern on the mask as shown in Fig. 3.14, then the sample is exposed. Next the sample is placed in MF26A for 1 minute in order to develop the resist and to produce the required pattern on the sample, then the sample is rinsed in DI water and blown dry.

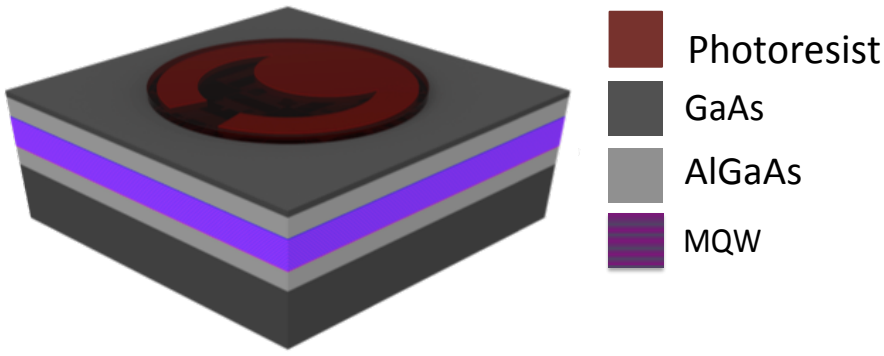

Figure 3. 14 Photolithograph on the sample prepared to be etched by 1:1:1 wet etch

A mixture of well-known 1:1:1 chemical etchants (acetic acid, hydrobromic acid and potassium dichromate) are used to etch the mesa through the active region; then the devices are rinsed in DI water and blown dry, the device after the wet etching prosess is shown in Fig. 3.15.

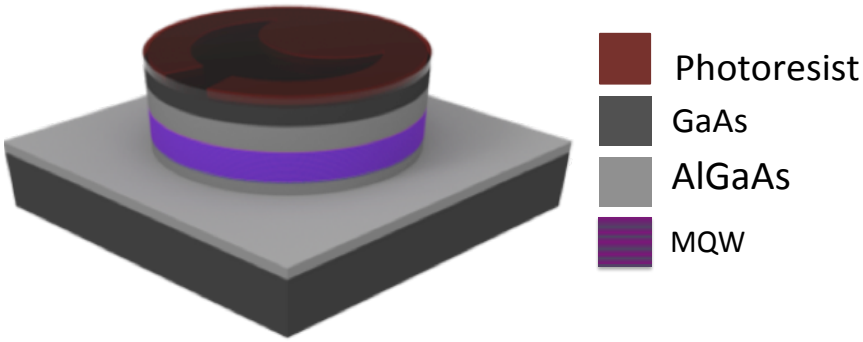

Figure 3.15 Device after the mesa wet etching process

Next the sample is placed in a beaker of acetone in order to dissolve and remove the photoresist on top of the gold. After the photoresist has been removed, the sample is exposed to O_2 plasma ash for 30 seconds in order to remove any residual photoresist, Fig. 3.16 shows the device after the mesa wet etching and lift off process.

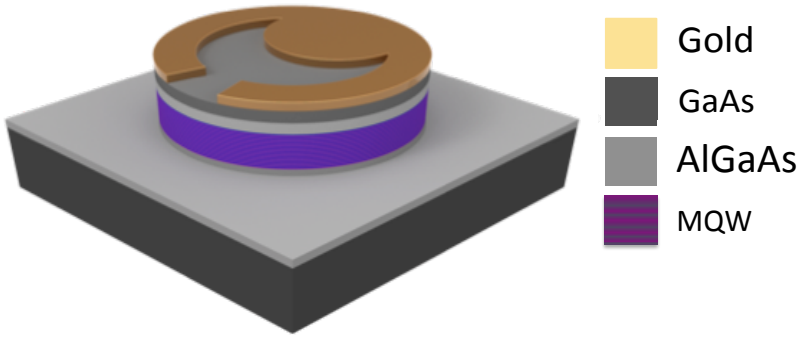

Figure 3.16 Device after the lift off process

Fig. 3.17 shows the backside metal contact is deposited on the sample by using a thermal evaporator. The evaporator is set up again by placing a tungsten coil/heating element and a tungsten coil/heating element basket at 6 cm. The tungsten coil/heating element basket is filled with ~10 mg of indium, and ~10 mg of

germanium, also a two 2 cm length of folded gold wire is placed in the tungsten coil/heating element. The sample is rinsed in 19:1 Analar Ammonia solution for 30 seconds to remove the surface oxide, rinsed in DI water and blown dried. It is placed inside the thermal evaporator, then the chamber is pumped down to a pressure of ~10^{-6} mbar, 20 nm of indium/germanium alloy is first deposited onto the surface, with 400 nm gold deposited as the last layer. After the deposition process is complete the sample is allowed to cool down, and then the sample is annealed in the RTA for 30 seconds at 340 ^{o}C in order to produce a low resistance n-type contact on the backside of the sample.

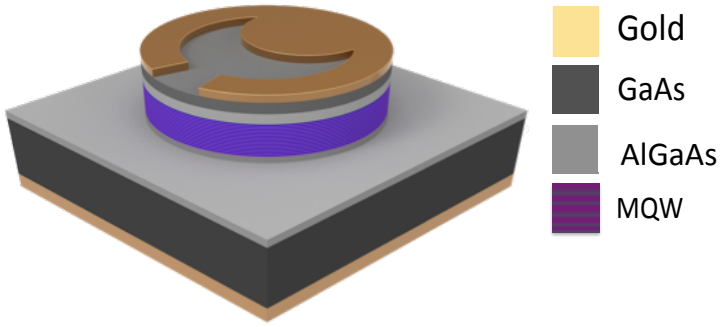

Figure 3.17 Metallization on rear side of the device

Finally, the devices are cleaved and mounted onto a gold ceramic tile using indium epoxy at 120 °C, the devices are then wire bonded in readiness for different kinds of characterization. Fig 3.18 shows the cleaved mesa device attached to the tile.

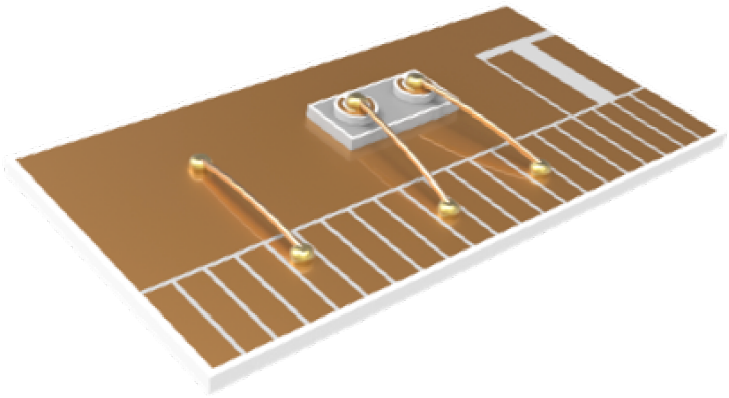

Figure 3.18 Cleaved devices mounted onto gold tile

3.6 Photocurrent Spectroscopy (PC)

Photocurrent spectroscopy is one a type of spectroscopy widely used to study the electronic and optical properties of semiconductor low dimensional structures, like quantum well structures. PC is complimentary to PL as it provides absorption related information, and is also appropriate for experimental conditions where the temperature is high or the application of an electric field is required [36]. PC spectroscopy has three main steps: photo-absorption, which generates carriers, carrier transport, and recombination. Fig. 3.19 shows the schematic diagram of the experimental apparatus used to measure the PC spectra of the sample.

Light from a tungsten lamp source is modulated by the optical chopper and filtered by a monochromator, then focused on the p-type surface of optical p-i-n mesa diodes (400 μm), described previously in section 3.5. Once the mesa is optically excited, the absorbed photons in the intrinsic region generate electron-hole pairs, which drift towards the contacts due to the applied E-field. This relies on the carriers being able to escape before they recombine, either by tunnelling through the barrier or by thermionic emission directly over the potential barrier [37]. Signal:noise is improved

by the use of lock-in amplifier. The PC spectrum is recorded using the LabView program.

DC bias can be applied perpendicularly to the mesa diode by using a Keithley voltage source.

The photocurrent spectra is related to the absorption spectra and is very powerful, both for describing sub-band structures in the MQW structure and for investigating all the lower and higher lying intersub-band transitions.

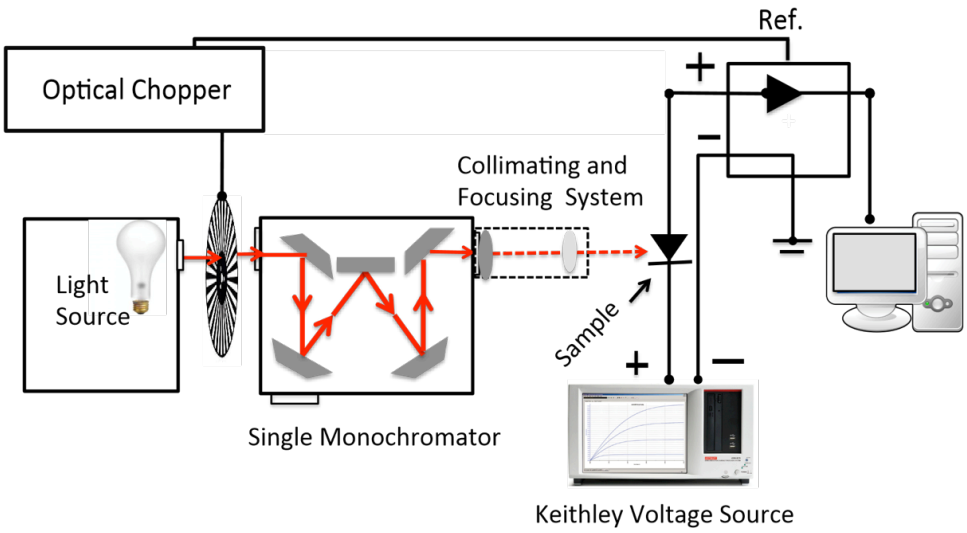

Figure 3.19 Schematic diagram of the photocurrent experimental setup

It is also valuable for studying the exciton binding energy and normally forbidden transition, where a different reverse bias is applied to the sample [38, 39].

In this thesis the photocurrent spectra for the MQW intrinsic region of the p-i-n sample was measured at room temperature, at zero bias and as a function of a different applied reverse bias.

Appling the reverse bias to the sample produces a strong DC electric field along the growth direction, the magnitude of which can be calculated by [30].

$$E = \frac{|V_{bi}-V_0|}{l_i}$$

where

V_{bi}: built in voltage ≈ 1.5 V [40]

V_0: applied bias

l_i: intrinsic region

The total thickness of the intrinsic quantum well region in the sample is 577.1 nm, and the built-in electric field is = 25.993 (kV/cm).

Fig. 3.20 plots the PC spectrum where no external bias is applied to the sample. The transition energies between valence sub-bands and conduction sub-bands, calculated using Nextnano, are also plotted. The energy states of 3 electron, 3HH and 3LH are all considered. Excellent agreement is observed between simulation and experiment results over a wide range of transitions.

The highest exciton peaks were observed at 1.452 eV and 1.465 eV, corresponding to the transition between the lowest quantized levels in the conduction band (E1) and HH1, LH1 in the valence band.

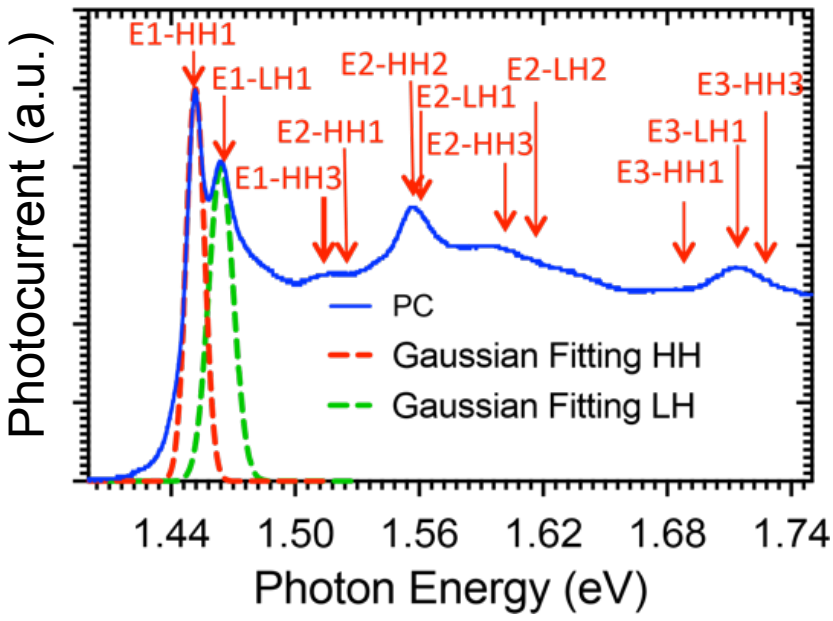

Figure 3.20 Measured PC spectrum. Transitions are identified from their expected transition energies from simulation; also Gaussian fits to E1-HH and E1-LH1 are shown

In a low electric field, the PC spectrum shows exciton peaks for the allowed transition in relation to the selection rules. When the electric field is increased, however, more exciton peaks appear in the PC spectra as a result of the associated deformation of the well potential, warping the electron and holes wave function and moving them in a different direction, thus making the overlap integral between the electron and hole wave-function no longer equal to zero for forbidden transitions.

Another obvious effect of increasing the electric field on the PC spectra is the shift of the interband transition exciton energy to the lower energy as a result of the quantum confined Stark effect (QCSE) [20]. Fig. 3.21 shows a series of spectra for the sample as a function of the applied electric field. The dotted line is used to highlight the shift in the exciton peaks for the E1-HH1 and E1-LH1 transitions as a function of the applied electric field.

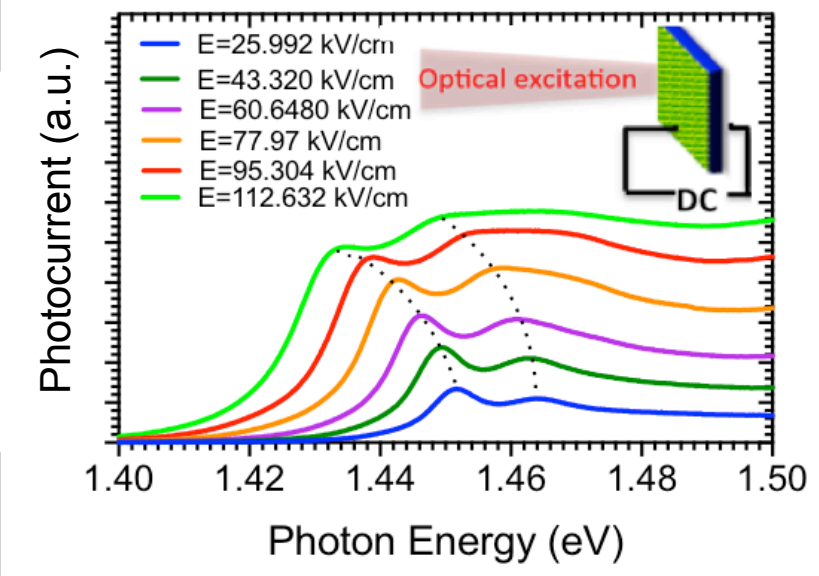

Figure 3.21 Photocurrent spectra at room temperature of the GaAs/AlAs MQW diode as function of the applied electric field

When the applied electric field was low this showed some agreement with the calculated values, as shown in Fig. 3.22 below. With stronger electric fields,

however, there was less agreement, due to the broadening of the PC spectra, which makes it difficult to determine the exact values of the peaks.

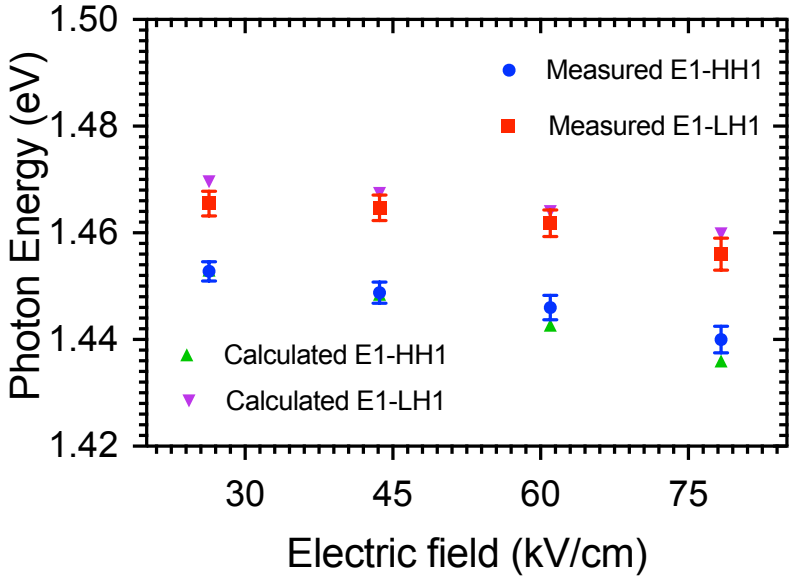

Figure 3.22 Measured and calculated transition energies between states E1-HH1 and E1LH1 according to the applied electric field

To summarise the design of the sample was highlighting and the main points in its structure design rules was discussed in detail, an introduction of MBE was given as it was the techniques used to grow the sample. Different sample characterization techniques were explained and the results discussed. A good agreement between the sample design and the manufactured sample was reported.

3.7 Future Work

A thorough study of the optimal growth techniques for realising good structures and hence narrow excitonic transitions has not been made. Using photoluminescence excitation (PLE) and photoluminescence (PL), an optimisation of the growth process

could be carried out. This would be best at low temperatures as this would help to determine the transition linewidths, free of thermal broadening. Using different growth processes in MBE such as migration-enhanced epitaxy (MEE) [41] may be a route to enhanced excitonic transitions. Furthermore, MOVPE could be considered if any phosphorous alloy such as InGaP is added to the sample structure as a stop layer [42], (proposed for new structure in next chapter). Applying an external bias to realize the QCSE in QWs is explained in section 3.6 and this allows tuning the transition energy of both E1-HH1 and E1-LH1 and result in tuning the emitted THz. Therefore considering the fabricating of a contact in the sample is required which will enable connecting the sample to the external voltage source and allow us to apply an electric field.

References

1. Leo, K., Damen, T.C., Shah, J., Göbel, E.O., Köhler, K.: Quantum beats of light hole and heavy hole excitons in quantum wells. Appl. Phys. Lett. 57, 19–21 (1990).

2. Shah, J., Leo, K., Gobel, E., Schmitt-Rink, S., Damen, T., Schafer, W., Kohler, K.: Quantum beats of excitons in quantum wells. Surf. Science. 267, 304–309 (1992).

3. Planken, P.C.M., Nuss, M.C., Brener, I., Goossen, K.W., Luo, M.S.C., Chuang, S.L., Pfeiffer, L.: Terahertz emission in single quantum-wells after coherent optical-excitation of light hole and heavy hole excitons. Phys. Rev. Lett. 69, 3800–3803 (1992).

4. Hosoda, M., Mimura, H., Ohtani, N., Tominaga, K., Fujita, K., Watanabe, T., Inomata, H.: Observation of Γ-X resonances in type-I GaAs/AlAs semiconductor superlattices : Anomaly in photoluminescence. 55, 689–696 (1997).

5. Miller, D.A.B.: Optical Physics of Quantum Wells. Quantum Dyn. Simple Syst. Oppo, G. -L., Barnett, S. M., Riis, E., Wilkinson, M., Eds.; Inst. Phys. London. 239–266 (1996).

6. Mitin, V. V, Kochelap, V.A., Stroscio, M.A.: Quantum heterostructures : microelectronics and optoelectronics. Cambridge University Press, Cambridge, UK (1999).

7. Chemla, D., Miller, D., Smith, P., Gossard, A., Wiegmann, W.: Room temperature excitonic nonlinear absorption and refraction in GaAs/AlGaAs multiple quantum well structures. IEEE J. Quantum Electron. 20, 265–275 (1984).

8. Miller, A., Ebrahimzadeh, M., Finlayson, D.M.: Semiconductor Quantum Optoelectronics. Scottish University Summer School in Physics&Institute of Physics Publishing, Bristol and Philadelphia (1999).

9. Miller, R.C., Kleinman, D.A.: Excitons in GaAs quantum wells. J. Lumin. 30, 520–540 (1985).

10. Downs, C., Vandervelde, T.E.: Progress in infrared photodetectors since 2000. Sensors (Switzerland). 13, 5054–5098 (2013).

11. Cho, A.Y.: Growth of III-V semiconductors by molecular beam epitaxy and their properties. Thin Solid Films. 100, 291–317 (1983).

12. Seshan, K.: Handbook of Thin Film Deposition Processes and Technology Processes and Techniguies, Principles, Methods, Equipment and Applications. Noyes Publications / William Andrew Publishing, New York, U.S.A (2002).

13. Pelzel, R.: A comparison of MOVPE and MBE growth technologies for III-V epitaxial structures. In: CS MANTECH Conference, USA. 105–108 (2013).

14. Miller, D.A.B., Chemla, D.S., Eilenberger, D.J., Smith, P.W., Gossard, A.C., Tsang, W.T.: Large room-temperature optical nonlinearity in GaAs/Ga1-x AlxAs multiple quantum well structures. Appl. Phys. Lett. 41, 679–681 (1982).

15. Gehrsitz, S., Reinhart, F.K., Gourgon, C., Herres, N., Vonlanthen, A., Sigg, H.: The refractive index of empirical modeling below the band gap : Accurate determination and The refractive index of AlxGa1-x As below the band gap : Accurate determination and empirical modeling. (2001).

16. Goldberg, Y.A.: Handbook Series on Semiconductor Parameters, Volume 2: Ternary and Quaternary Semiconductors, (1999).

17. Levinshtein, M., Rumyantsev, S.L., Shur, M., Scientific, W.: Handbook Series on Semiconductor Parameters: Ternary and quaternary III-V compounds. World Scientific Publishing Company (1999).

18. Palik, E.D.: Gallium Arsenide (GaAs). Handb. Opt. constants solids. 1, (1985).

19. Nextnano3, http://www.nextnano.com/nextnano3/.

20. Miller, D.A.B., Chemla, D.S., Damen, T.C., Gossard, A.C., Wiegmann, W., Wood, T.H., Burrus, C.A.: Band-edge electroabsorption in quantum well structures: The quantum-confined stark effect. Phys. Rev. Lett. 53, 2173–2176 (1984).

21. Miller, D.A.B., Chemla, D.S., Damen, T.C., Gossard, A.C., Wiegmann, W.,

Wood, T.H., Burrus, C.A.: Electric field dependence of optical absorption near the band gap of quantum-well structures. Phys. Rev. B. 32, 1043–1060 (1985).

22. Cho, A.Y.: How molecular beam epitaxy (MBE) began and its projections into the future. J. Cryst. Growth. 202, 1–7 (1999).

23. Cho, A.Y.: Film Deposition by Molecular-Beam Techniques. J. Vac. Sci. Technol. 8, S31 (1971).

24. Cho, A.Y., Cheng, K.Y.: Growth of extremely uniform layers by rotating substrate holder with molecular beam epitaxy for applications to electro-optic and microwave devices. Appl. Phys. Lett. 38, 360–362 (1981).

25. Ohring, M.: Materials Science of Thin Films. Academic Press (2002).

26. Rinaldi, F.: Basics of molecular beam epitaxy (MBE). NIVERSITÄT ULM. 31 (2002).

27. Holloway, P., McGuire, G.: Handbook of Compound Semiconductors - Growth, Processing, Characterization, and Devices. William Andrew Publishing/Noyes, New Jerssey (1995).

28. Bauer, G., Richter, W.: Optical characterization of epitaxial semiconductor layers. Springer Science & Business Media (2012).

29. Joyce, B.A.: Molecular beam epitaxy. Reports Prog. Phys. 48, 1637–1697 (1985).

30. Mark Fox: Optical Properties of Solids. , Oxford, UK (2010).

31. Mihara, M., Nomura, Y., Mannoh, M., Yamanaka, K., Naritsuka, S., Shinozaki, K., Yuasa, T., Ishii, M.: Composition dependence of photoluminescence of $Al_xGa_{1-x}As$ grown by molecular beam epitaxy. J. Appl. Phys. 55, 3760–3764 (1984).

32. Perkowitz, S.: Optical Characterization of Semiconductor: Infrared, Raman, and Photoluminescence Spectroscopy. Academic Press Limited, London (1993).

33. Beer, W.: Semiconductors and Semimetals., Academic Press, London (1987).

34. Miller, R.C., Kleinman, D.A., Tsang, W.T., Gossard, A.C.: Observation of the

excited level of excitons in GaAs quantum wells. Phys. Rev. B. 24, 1134–1136 (1981).

35. Bastard, G., Mendez, E.E., Chang, L.L., Esaki, L.: Exciton binding energy in quantum wells. Phys. Rev. B. 26, 1974–1979 (1982).

36. Polland, H.J., Horikoshi, Y., Gobel, E.O., Kuhl, J., Ploog, K.: Photocurrent and picosecond photoluminescence spectroscopy in GaAs/AlGaAs quantum well. Surf. secience. 174, 278–282 (1986).

37. Kawasaki, K., Imazawa, M., Kawashima, K., Fujiwara, K.: Negative peaks in photocurrent spectra of thick barrier GaAs / AlAs multiple quantum Negative peaks in photocurrent spectra of thick barrier GaAs / AlAs multiple quantum wells. 84, 3338–3341 (1998).

38. Yamanaka, K., Fukunaga, T., Tsukada, N., Kobayashi, K.L.I., Ishii, M.: Photocurrent spectroscopy in GaAs/AlGaAs multiple quantum wells under a high electric field perpendicular to the heterointerface. Appl. Phys. Lett. 48, 840–842 (1986).

39. Collins, R.T., Klitzing, K.V., Ploog, K.: Photocurrent Spectroscopy of GaAs/AlxGa1-xAs Quantum Wells in an Electric Field. Phys. Rev. B. 33, 8–11 (1986).

40. Fox, M.: Optical Properties of Solids. Oxford University Press, Oxford, 2010 (2010).

41. Horikoshi, Y., Kawashima, M., Yamaguchi, H.: Migration-Enhanced Epitaxy of GaAs and AlGaAs. Jpn. J. Appl. Phys. 27, 169 (1988).

42. Hsieh, Y.C., Chang, E.Y., Yeh, S.S., Chang, C.W., Luo, G.L., Chang, C.Y., Lee, C.-T.: Optimization of the growth of the InGaP etch-stop layer by MOVPE for InGaP/GaAs HBT device application. J. Cryst. Growth. 289, 96–101 (2006).

Chapter Four

Sample Preparation Processes

4.1 Introduction

This chapter describes the sample preparation processes and explains in detail how the sample was processed in order to maximize the incident pump power available for absorption in the QWs and minimize the THz signal power absorbed through the heavily doped n-GaAs sample substrate. Since the pump power absorption calculation, made using the p-GaAs absorption coefficient [1] at a pumped laser wavelength ≈ 850 nm, indicated that 20% of the total laser pump power was absorbed in the p-GaAs cap layer, it was clear that the cap layer should be totally removed. In addition, the absorption coefficients [2] indicate losses in excess of 6 dB/μm for this material at the THz wavelength, therefore, given a n-GaAs substrate any thickness >≈ 1 μm, most, if not all the THz radiation generated by the device would be absorbed in the substrate. Hence, the complete removal of the substrate was required. One method that has been widely investigated and is applied here for removing the p-GaAs cap layer and n-GaAs substrate and for preparing the sample for measurement is wet etching.

4.2 The Wet Etching Process

Wet etching is a material removal process in which special chemical liquids, known as etchants, are employed to remove unwanted material from the area of the structure, and is widely used in the manufacturing of semiconductor devices [3, 4]. Wet etching is carried out in three stages: the first involves dispersion of the etchant to the area from which unwanted material is to be removed; in the second stage, a reaction occurs between the liquid etchant and the material being removed, causing oxidation of the material. This leads to the third stage, in which the oxidized material is dissolved. Finally, the products of the reaction are diffused from the reacted surface.

The chemical etchant usually contains two components: oxidizing and dissolving agents. In the etchant system used in the work carried out for this thesis, H_2O_2 (30%) was always the oxidizer and citric acid and ammonia H_3PO_4 were used as dissolvers. A well-behaved chemical etching composition can selectively remove a particular part of the structure or specific material (S) without damaging the rest of the structure.

The selectivity coefficient S of the solutions can be defined as below:

$$S = \frac{R_1}{R_2} \tag{4.1}$$

where

R_1: etch rate for the material to be removed

R_2: etch rate for the stop layer

Thus, the optimal solution has a higher R_1 and lower R_2 for high selectivity. The etch rates are determined by dividing the etched depth by the time taken for the etching process to be completed.

In this experiment, the samples were prepared for wet etching by cleaving the wafer into small pieces (8×8 mm), then cleaning the samples by immersing them in acetone and isopropyl alcohol, for 5 min. each. The samples were checked under the microscope and, once clean, attached to a microscope slide after a thin layer of wax had been applied to the glass. They were then heated on a hotplate and left at room temperature for 30 minutes to cool down, as shown in Fig. 4.1.

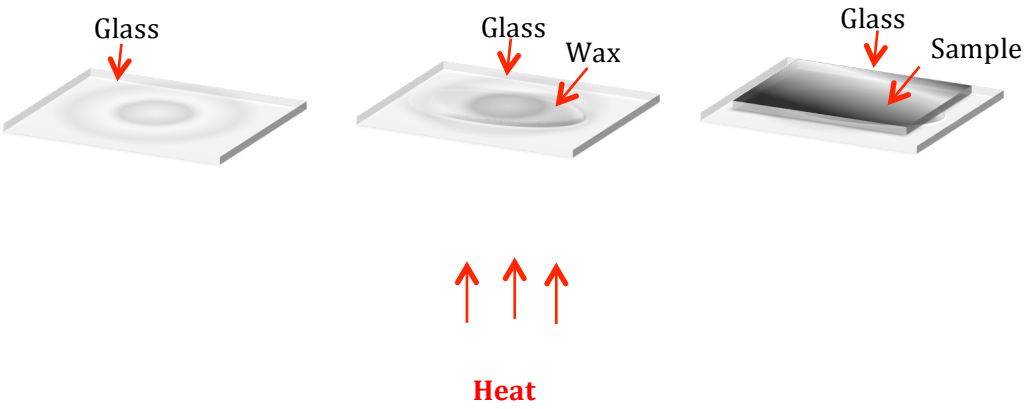

Figure 4.1 Sample prepared for wet etching

While cooling was taking place, the etchant was mixed and prepared, and the samples were then submerged in the chemical solution for the necessary period. Neither agitation nor jet streams were used during the etching process. The samples were then removed from the etchant, washed in DI water and blow-dried with N_2, before the etching depths were measured with a mechanical stylus profile meter (Dektak). Different chemical etchants were investigated in terms of their ability to remove the GaAs with respect to AlGaAs; specifically, $NH_4OH+H_2O_2$, $C_6H_8O_7+H_2O_2$, $H_3PO_4+ H_2O_2+H_2O$, as shown in table 4.1. All the etching tests were carried out at room temperature. The chemical etchants were chosen based on the fastest etching rate and highest selectivity, as illustrated in [5–11].

Etchants	GaAs	$Al_{0.4}Ga_{0.6}As$	Selectivity
$NH_4OH+H_2O_2$ (1 : 1)	4.5 μm/min.	0.4 μm/min.	11.2
$NH_4OH+H_2O_2$ (1 : 50)	1 μm/min.	0.015 μm/min.	66.6
$H_3PO_4+H_2O_2+H_2O$ (3 : 1 : 25)	0.3 μm/min.	0.01μm/min.	30
$NH_4OH+H_2O_2$ (1 : 225)	0.2 μm/min.	0.010 μm/min.	20
Citric acid $+H_2O_2$ (4 : 1)	0.34 μm/min.	0.00347 μm/min.	102

Table 4.1 Etch rate and selectivity for different chemical etchants at different concentrations

Unlike the ammonia-based etchant, the citric acid + hydrogen peroxide etchant has a low etch rate. Moreover, since the etch rate was linearly proportional to the etch time, the etch mechanisms for citric acid + hydrogen peroxide were investigated using a range of solution concentrations. The highest selectivity was achieved with a ratio of 4:1, as is shown in Fig. 4.2. The citric acid was prepared by mixing citric acid powder with H_2O, with ratio of 1:1.

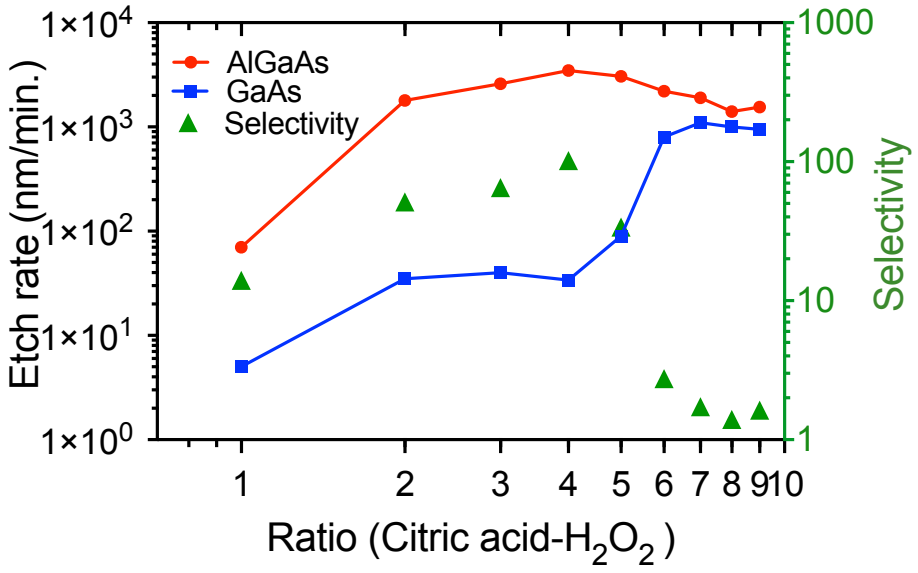

Figure 4.2 Etch rates of the GaAs and $Al_{0.4}Ga_{0.6}As$ versus volume ratio of citric acid + H_2O_2 at room temperature

The selectivity at this composition was 102, with a smooth etching profile, as shown in Fig. 4.3.

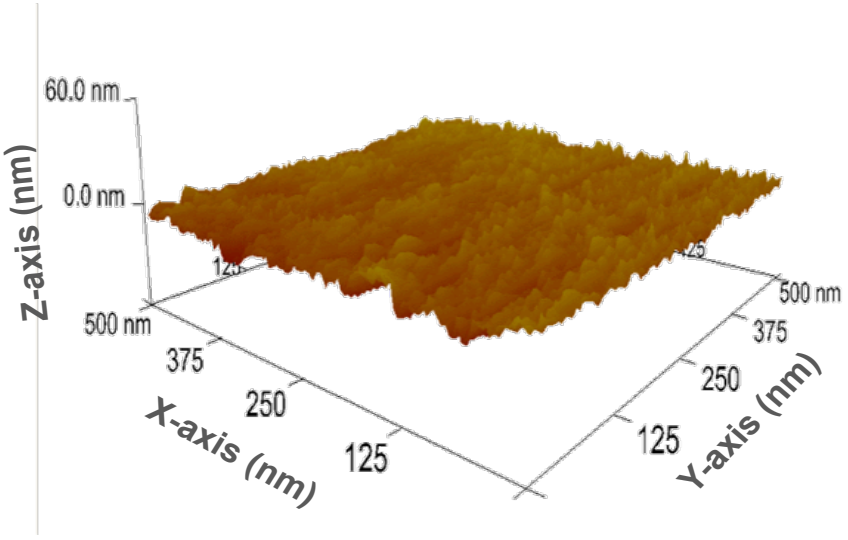

Figure 4.3 AFM images taken from the surface of the GaAs etched by a solution of citric acid + H_2O_2 with ratio of 4:1

It was observed that the $NH_4OH+H_2O_2$ etchant with a ratio (1:1) had the highest etch rate but a rough etching profile, as shown in Fig. 4.4. As a result, this substance was used when fast, non-selective etching was required.

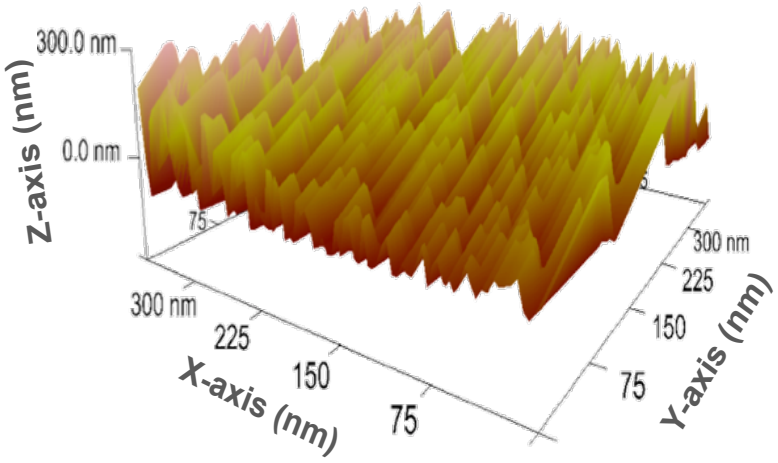

Figure 4.4 AFM image for the surface of the GaAs etched by a solution of $NH_4OH+H_2O_2$ with a ratio of 1:1

4.3 Capillary Bonding

Capillary bonding is a mechanism of surface tension used widely to pull the different semiconductor wafers to very close contact and strong bonding [12, 13]. The wafer surfaces should be polished and carefully well cleaned, the cleaning processes includes lightly etched of the sample surface, and then the sample and the glass rinsed in a liquid with a relatively strong adhesive forces, usually methanol is used [14], and then the sample and the glass were removed from the methanol, gradually the liquid with the strong adhesive forces evaporate across the edges of the wafers, and come to be thinner and finally pulled the wafers to the atomic contact. This process usually monitored with observing the interference fringes of the liquid thin film via the top surface of a transparent wafer glass, diamond or sapphire, at the

beginning the some fringes are appeared and then gradually disappear (the fringeless surface specify a wafer separation less than quarter of the visible wavelength), within several hours the remaining thin layer of liquid is completely escape and the best atomic contact between wafers are achieved [12].

4.4 Sample Preparation Process Steps

A wafer with a diameter of 2" was scribed at the edge with a diamond tip scriber, then the piece to be used in the process was cleaned using the three-step solvent process so as to ensure that all dust and debris were removed. In order to do this, the sample was decanted into a beaker of n-Butyl acetate and boiled for approximately 30 seconds, after which the sample was removed, cleaned with cotton buds, and put into warm acetone; then the sample was removed from the acetone and immersed in warm isopropyl alcohol for a few seconds; and finally the sample was removed from the isopropyl alcohol and dried with nitrogen gas.

- A p-GaAs cap layer etched using a citric acid to water ratio of 1:1, and ratio of this solution to hydrogen peroxide of 4.
- Since the substrate-free structure is very fragile, the sample is attached to diamond or glass by capillary bonding (explained in section 4.3), in order to support it prior to substrate removal. In this case, a diamond wafer was used because it has better thermal conductivity (2000 $W.m^{-1}.K^{-1}$) [15] than glass (1 $W.m^{-1}.K^{-1}$) [16], and also has good transparency ≈ 70% in the range of the excitation wavelength [15].

The diamond wafer and the sample without the cap layer were cleaned using the three solvents technique, in order to ensure capillary bonding [14], the cleaning involving the following process; first, the sample and the diamond wafer were put into a beaker of n-Butyl acetate and boiled for approximately 30 seconds; then they were removed from the solvent and immersed in warm acetone; after this, the sample and diamond were removed from the acetone and placed in warm isopropyl alcohol for a few seconds, before being removed and dried with a nitrogen gas.

Both the sample and the diamond were examined under a microscope to check their surface cleanliness; if any of them were still not completely clean then the entire cleaning processes was repeated until they were dirt-free.

- The sample and the diamond were then processed by plasma ashing (a process of removing photo-resist which become ash (carbon) during reacting with O_2), for 4 minutes, and finally rinsed in $NH_4OH:H_2O$ (1:19) in order to remove the native oxide and make the surface hydrophilic, in order for it to achieve high quality capillary bonding. The contact angle of water on the surface can be measured in order to assess the hydrophobicity of the surfaces, as shown in Fig. 4.5. Observations confirmed that the angle was less than 90^o, and thus the surface was hydrophilic [17].

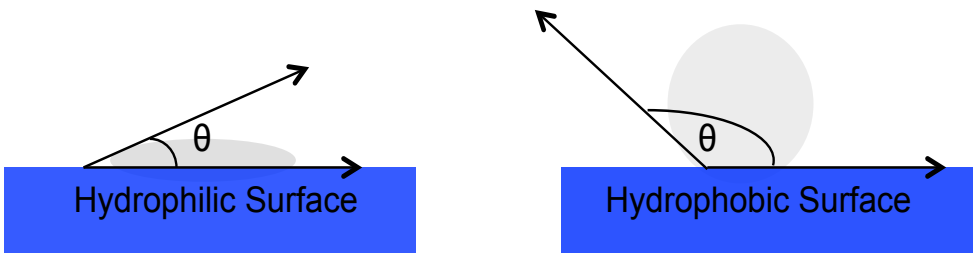

Figure 4.5 Hydrophobic surface and hydrophilic surfaces

- Finally, the treated sample and diamond wafer were immersed in methanol for several minutes and put into contact with each other. After removal, the sample was found to have attached to the diamond wafer.

  It was found if the wet etching took place immediately after removing the sample and the diamond from the methanol the sample delaminated from the diamond, but leaving them in an open place for few hours allowed the sample and the diamond to develop a strong enough bonding to resist the wet etching processes for many hours, thereby allowing the whole substrate to be removed.

For small samples ≤ (4×4) mm, where a lapping machine may be unsuitable for thinning the substrate, a combination of non-selective and selective etching can be used. The first 200 μm was etched using $NH_4OH+H_2O_2$ (1:1), which has a high etch rate, but a rough etch profile and low selectivity, as shown in Fig. 4.4 this was followed by etching with citric acid and H_2O_2, generating a slower, selective etch. In this case, the etch stopped once the substrate was entirely removed, as depicted in Fig. 4.6.

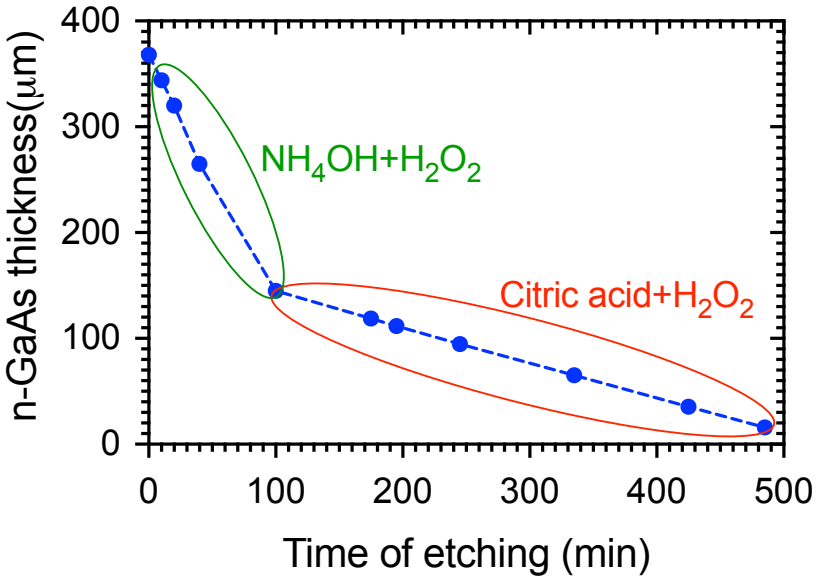

Figure 4.6 Sample thicknesses (measured by Dektak) as a function of etching time using the two-stages wet etching process

Alternatively, for comparatively large samples, once the selective etching of the p-GaAs cap has been completed, the n-GaAs substrate may be lapped to a thickness of ~150 μm, capillary bonded, and selectively etched using citric acid and H_2O_2. Surface profiling indicated that, in this case, the finished sample thickness was ≈ 3.68 μm, which was confirmed by cross-sectional SEM, as shown in Fig. 4.7. This is in a good agreement with the thickness of the epitaxial layer (≈ 3.6 μm), suggesting that all of the cap layer and substrate were removed.

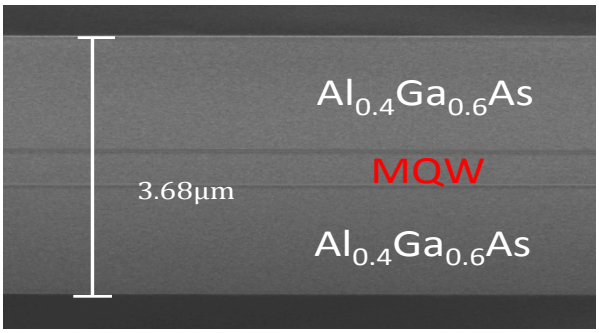

Figure 4.7 SEM image indicating the thickness of the prepared sample

In summary, this chapter has reported a method to remove the cap layer from p-doped GaAs and the substrate from n-doped GaAs from the sample. The described process satisfies the objective of reducing pump laser absorption in the cap and THz absorption in the substrate.

Two approaches to complete substrate removal have thus been examined: first, considering the sample size before attaching the sample to a diamond wafer to provide support and encourage heat extraction; and second, preparing the sample prior to the THz measurement.

Both these approaches successfully achieved substrate removal. A combination of non-selective and selective etching can be used with a comparatively small sample, while larger samples can initially be thinned with a lapping machine before selective etching.

4.5 Future Work

Different material such as InGaP which has a good lattice match to the GaAs [18, 19], could be used in between the AlGaAs and the n-GaAs substrate layers during the sample growth, this provides an easier way to remove the substrate, since a high selectivity rate of the GaAs over InGaP or InGaP over GaAs is achievable with using plasma dry etching [20, 21]. In both cases the sample could be release from the substrate. Moreover since the high resistivity Si has a good transparency to THz [22], therefore it is a very attractive to be used (bound to the backside of the sample) instead of the diamond (bound to the front side of the sample) to support the thin sample and in meanwhile provide a good waveguide platform for the THz wave.

References

1. Casey, H.C., Sell, D.D., Wecht, K.W.: Concentration dependence of the absorption coefficient for n- and p-type GaAs between 1.3 and 1.6 eV. J. Appl. Phys. 46, 250–257 (1975).

2. Kim, U.W., Oh, S.J., Maeng, I., Kang, C., Son, J.-H.: Terahertz Electrical Characteristics of Heavily Doped n-GaAs Thin Films. J. Korean Phys. Soc. 50, 789 (2007).

3. Campbell, S.A.: The Science and Engineering of Microelectronic Fabrication. Oxford University Press, Oxford, UK (2001).

4. Pearton, S.J., Ren, F.: Wet chemical etching of compound semiconductors. Proc. Electrochem. Soc. 147–159 (2005).

5. Clawson, A.R.: Guide to references on III-V semiconductor chemical etching. Mater. Sci. Eng. R Reports. 31, 1–438 (2001).

6. Mori, Y., Watanabe, N.: A New Etching Solution System, H_3PO_4-H_2O_2-H_2O, for GaAs and Its Kinetics. J. Electrochem. Soc. 125, 1510–1514 (1978).

7. Kim, J.-H., Lim, D.H., Yang, G.M.: Selective etching of AlGaAs/GaAs structures using the solutions of citric acid/H_2O_2 and de-ionized H_2O/buffered oxide etch. J. Vac. Sci. Technol. B Microelectron. Nanom. Struct. Process. Meas. Phenom. 16, 558–560 (1998).

8. Ribas, R., Leclercq, J., Karam, J., Courtois, B., Viktorovitch, P.: Bulk micromachining characterization of 0.2 μm HEMT MMIC technology for GaAs MEMS design. Mater. Sci. Eng. B. 51, 267–273 (1998).

9. Juang, C.: Selective etching of GaAs and $Al_{0.30}Ga_{0.70}As$ with citric acid/hydrogen peroxide solutions. J. Vac. Sci. Technol. B Microelectron. Nanom. Struct. 8, 1122 (1990).

10. Haszko, S.E., Journal, T., Desalvo, G.C., Tseng, W.F., Comas, J.: Etch Rates and Selectivities of Citric Acid / Hydrogen Peroxide on GaAs, AlGaAs, InGaAs, InGaAs, InAlAs and InP. J. Electrochem. Soc. 139, 3–7 (1992).

11. Moon, E.-A., Lee, J.-L., Yoo, H.M.: Selective wet etching of GaAs on AlxGa1−xAs for AlGaAs/InGaAs/AlGaAs pseudomorphic high electron mobility transistor. J. Appl. Phys. 84, 3933–3938 (1998).

12. Liau, Z.L.: Semiconductor wafer bonding via liquid capillarity. Appl. Phys. Lett. 77, 651–653 (2000).

13. Mastrangelo, C.H.C.H., Hsu, C.H.H.: Mechanical stability and adhesion of microstructures under capillary forces. I. Basic theory. J. Microelectromechanical Syst. 2, 33–43 (1993).

14. Jerez-Hanckes, C.F., Qiao, D., Lau, S.S.: A study of Si wafer bonding via methanol capillarity. Mater. Chem. Phys. 77, 751–754 (2003).

15. Colbran, S.B.: Element Six CVD Diamond Handbook. 1–9 (2015).

16. Greg Becker; Chris Lee, Z.L.: Thermal conductivity in advanced chips-Emerging generation of thermal greases offers advantages. (2005).

17. Drelich, J., Chibowski, E., Meng, D.D., Terpilowski, K.: Hydrophilic and superhydrophilic surfaces and materials. Soft Matter. 7, 9804 (2011).

18. Vurgaftman, I., Meyer, J.R., Ram-Mohan, L.R.: Band parameters for III-V compound semiconductors and their alloys. J. Appl. Phys. 89, 5815–5875 (2001).

19. Nayak, P.P., Dutta, J.P., Mishra, G.P.: Efficient InGaP/GaAs DJ solar cell with double back surface field layer. Eng. Sci. Technol. an Int. J. 18, 325–335 (2015).

20. Hays, D., Cho, H., Jung, K., Hahn, Y., Abernathy, C., Pearton, S., Ren, F., Hobson, W..: Selective dry etching using inductively coupled plasmas: Part I. GaAs/AlGaAs and GaAs/InGaP. Appl. Surf. Sci. 147, 125–133 (1999).

21. Leerungnawarat, P., Cho, H., Hays, D.C., Lee, J.W., Devre, M.W., Reelfs, B.H., Johnson, D., Sasserath, J.N., Abernathy, C.R., Pearton, S.J.: Selective dry etching of InGaP over GaAs in inductively coupled plasmas. J. Electron. Mater. 29, 586–590 (2000).

22. Lee, Y.-S.: Principles of Terahertz Science and Technology. Springer, New York, U.S.A (2009).

Chapter Five

Laser Characterization, Absorption Measurements, and Preliminary THz Measurements

5.1 Introduction

This chapter describes the experimental setup that was assembled and used to measure the THz signal generation through DFG and to confirm the second order nonlinear phenomena. It provides information about the operating characterization of the two CW lasers, as well as a detailed account of the different optical elements used to collimate and overlap the laser beams, the imaging and THz detection system. The chapter also explains the setup of the absorption measurement process, and gives a comparison of the absorption at high excitation of the sample (as prepared in chapter 4) to the PC spectrum obtained from a mesa-diode structure (described in chapter 3). Preliminary results are presented of the generation of THz radiation using this new method, and the THz power dependence upon laser power is measured. Finally, the chapter discusses some of the interesting findings arising from this work.

5.2 Experimental Setup System for THz Generation and Detection

Fig. 5.1 shows a 3D schematic image of the THz generation and detection setup system and the optical beams (produced by SolidWorks). The system consists of the following main parts:

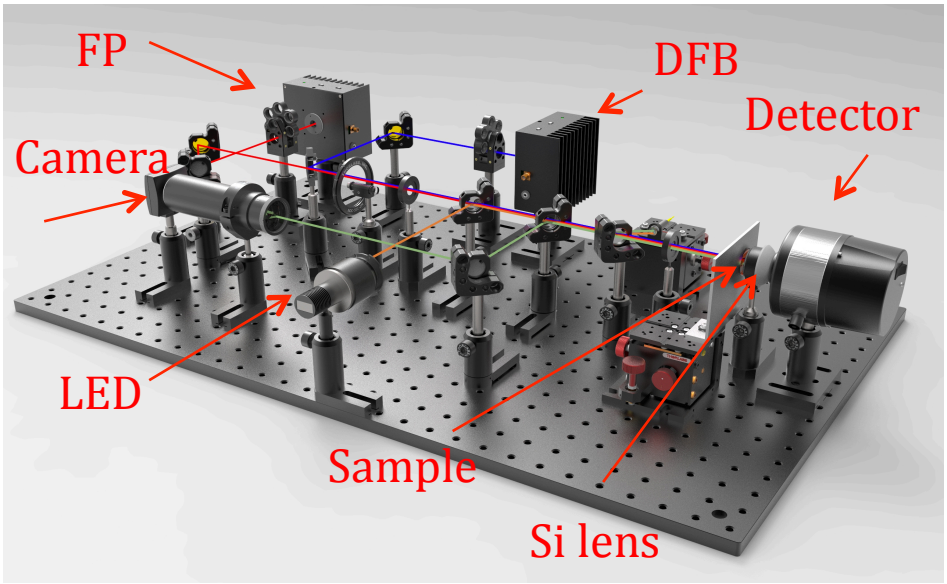

Figure 5.1 3D image of the THz generation and detection system

5.2.1 Laser System

The system includes two CW commercial single mode diode lasers, specifically Fabry-Perot (FP) and distributed feedback (DFB) lasers operating at slightly different wavelengths corresponding to the HH and LH exciton energy in the MQW structure (described in chapter 3). This is compact and more economical (a few hundred pounds) than other kinds of laser systems, such as Ti:Sapphire lasers (20-40 thousand pounds). The Ti:Sapphire laser, however, has a narrower linewidth with single mode operation (free of mode hop) and can therefore produce a higher power than the semiconductor diode laser.

Standard laser diodes are made of the active region of the laser diode in the intrinsic region, and the carriers (electrons and holes) are pumped into that region from the n- and p-regions respectively. Although the first generation of diode lasers was demonstrated on simple p-n diodes, all modern lasers have a double-heterostructure or QW structure, since this structure allows the carriers and the photons to be confined, thereby maximizing the probabilities of recombination and then light generation. In addition, laser diodes need a mechanism to provide optical feedback in order to generate the optical wave (e.g. pair of mirrors on the facet in FP lasers or grating in DFB lasers).

- **Fabry-Perot (FP) Laser**

With FP the optical feedback (produced by a pair of mirrors on the faces) generates standing wave patterns, thus allowing only an integer number of resonant frequencies or longitudinal modes to exist. The output wavelength also changes with temperature since the variation of the medium band gap with temperature produces a shift in the wavelength of the order of 0.5 nm/°C. Furthermore, a slight change in the temperature causes a shift in the wavelength, resulting from the variation of the index of refraction, as well as changes in cavity length due to thermal expansion, since the wavelengths occur at longitudinal modes of the cavity, and these modes depend on the cavity length [1].

In this work, a commercial Fabry-Perot laser diode from Thorlabs (L852P150) was used after being connected to a laser driver and temperature controller. Fig 5.2 shows the tuneability range of the FP laser wavelength (842.3 - 865 nm) as a function of the chip temperature at a constant power (130 mW). The current required to achieve this power is also plotted.

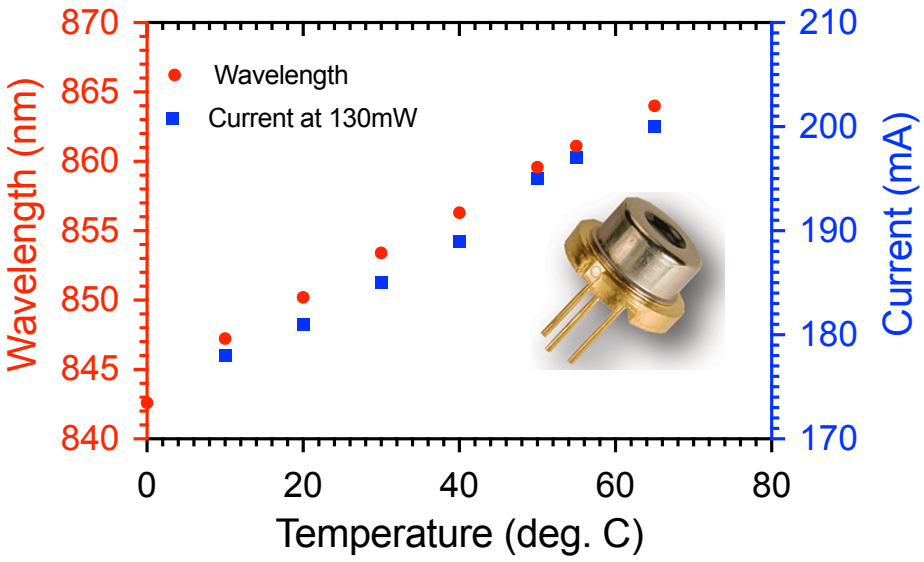

Figure 5.2 FP laser wavelength tuneability, with corresponding current and temperature

The laser tuning range is 22.7 nm and the $d\lambda/dT \approx 0.36$ nm/°C, which is in line with the Varshni equation for GaAs [2].

Whilst lasing predominantly from a single mode it was found that the lasing wavelength could alter suddenly (mode-hop) at certain temperatures. Fig. 5.3 plots the wavelengths of peaks observed in the emission spectrum of the F-P laser at 25° C as a function of drives current. At this particular temperature, two modes might compete for the available power, and the laser may switch backwards and forwards between them. This mode hopping [3], was avoided while the laser wavelength was tuned by careful adjustment of temperature and current to achieve a particular λ. Fig. 5.3 also shows the separation between the modes ≈ 0.45 nm.

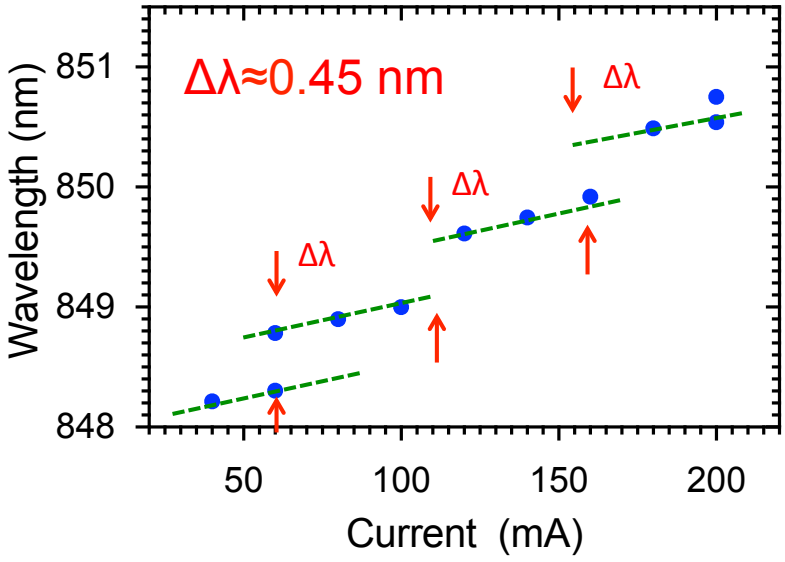

Figure 5.3 FP mode separation of the wavelength as a function of current

- **Distributed Feedback (DFB) Laser**

In contrast to the FP laser, the DFB does not use two discrete mirrors to form the optical cavity. Instead, it has a layer with a periodic variation in refractive index, or diffraction grating realised internally, close to the active region. This grating works as a distributed filter, which introduces a frequency that is selective of the optical losses [4], allowing only one of the longitudinal modes to propagate back and forth. The wavelength of DFB lasers can be tuned, since the wavelength shifts in line with temperature changes in the active region. This is possible to achieve by changing the temperature of the chip or the injected current. A commercial DFB laser from eagleyard (EYP-DFB-0852-00150) was used in this work and the temperature coefficient of the emission wavelength is expected to be 0.06 nm/°C based on its specification. Therefore the DFB laser's wavelength is tuneable within a limited range of 3.5 nm (as shown in Fig. 5.4) and the $d\lambda/dT \approx 0.05$ nm/°C, so has the ability to excite the HH.

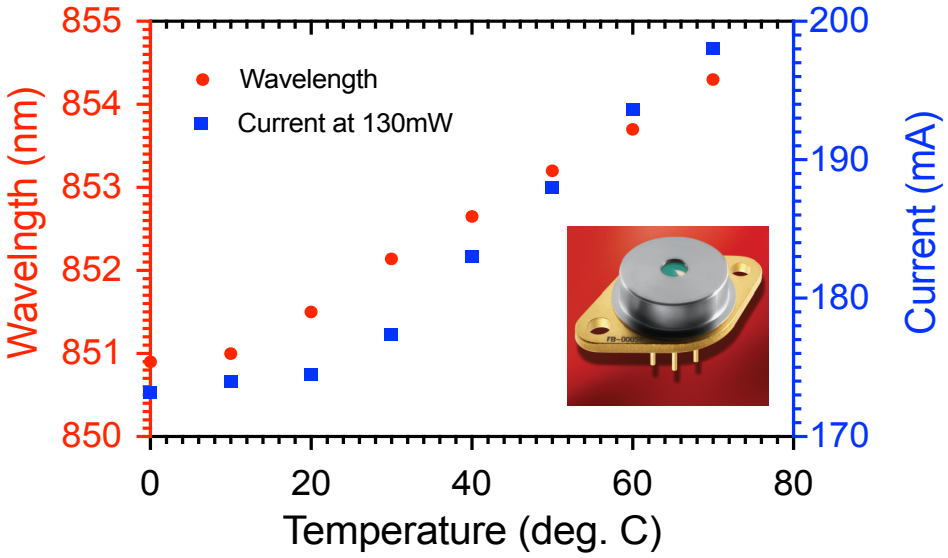

Figure 5.4 DFB laser wavelength tuneability, with corresponding to the current and temperature

The DFB laser has a narrower-spectral-width than the FP laser and is expected to give a linewidth of 2 MHz according to its specification, but in our measurements and resolution is limited to 0.1 nm, as it is attributed to the filter function of the measurement system optical spectrum analyser (OSA), it is also free mode hop and single longitudinal-mode laser [5], as shown in Fig. 5.5 (a). The figure also shows a wider measured linewidth for the FP laser compared to the DFB laser linewidth (Fig. 5.5 (b)).

The FP can operate in multimode, where the emission is made up of multiple longitudinal modes, and in this case the convolution of these modes can be several nanometres wide. While if it is operated in single mode, the laser linewidth is expected to be much narrower (~MHz) [6], but still not as narrow as is expected for the DFB laser linewidth (~ <MHz) [7].

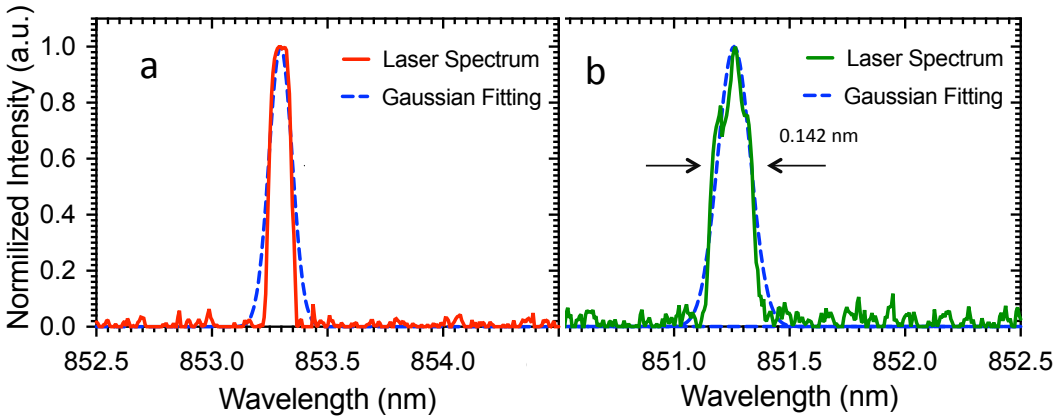

Figure 5.5 (a) DFB laser spectrum in red, and the dashed blue line is the Gaussian fitting, (b) FP laser spectrum in green and the blue dashed line is the Gaussian fitting

However, the linewidth of the FP is measured to be 0.142 nm as shown in Fig. 5.5 (b) the broadening in its linewidth is not because of the mode hop as the separation of the laser modes is about 0.45 nm as shown in Fig. 5.3. This broadening is unexpected, and could be originated from external optical feedback into the laser [8], or undesirable free-carrier/thermal effects within the laser cavity.

To summarize, two lasers were used, each of which has a narrow linewidth, although one was slightly broader than expected. The HH can be excited with the DFB laser, and there is sufficient tuneability to target absorption by this resonance peak correctly, while the FP laser can be tuned over the excitonic bands.

5.2.2 Laser Optics System

Fig. 5.6 illustrates the setup schematically. Many lenses and reflectors (mirror and beam splitters) were used to collect, collimate, direct and overlap the laser beams on the sample.

The laser was collimated using an aspheric lens (f=4.6 mm), then reflected by using gold mirrors with reflectivity > 96%, in order to get a very close distance between

the axes of the two laser beams, a broadband dielectric D-shaped mirror was used to reflect the FP laser beam at 90° to be co-axial with the DFB laser beam, at a distance of less than 2 mm. Since the lasers beams are invisible, a detection card was used to determine the distance between the two lasers beams. Then the lasers beams were passed through the pellicle beam splitter, uncoated for 8:92 (R:T) which introduces LED illumination of the sample (for imaging purpose).

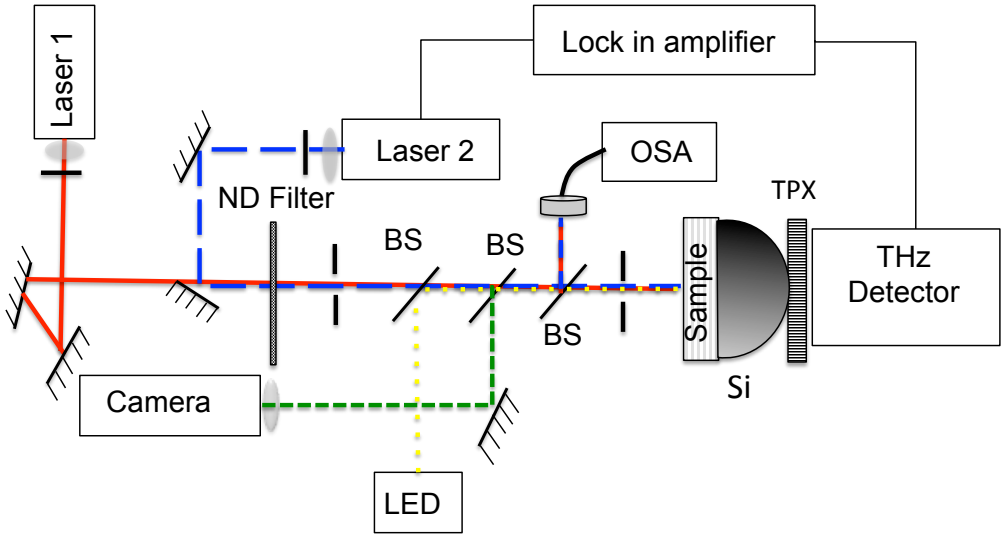

Figure 5.6 Schematic diagram of the THz generation and detection setup

The transmitted light goes through another pellicle beam splitter, uncoated for 8:92 (R:T), allowing the camera to image the sample, while the reflected light was focused on the light collimator, which was coupled and delivered the laser beams to the OSA with multi-mode fibre-optics. The OSA was used in order to monitor the single mode laser and the wavelength of the lasers. The transmitted light was passed through a 1 mm hole in the copper disk and was then incident onto the sample. The laser beams were aligned parallel to the optical bench. Several pinholes at various

points and at the same height from the base of the optical bench were used to ensure beam alignment.

An imaging system with a CCD camera and an LED light were used to check the overlap of the two laser beams onto the sample surface. Another method was used to monitor the overlap of the laser beams involving checking the overlapping beam spots of the two lasers at specific points from the sample holder (10-500 mm). Since the intention was to measure the non-linear optics effect, the part of the laser beams transmitted through the sample was measured in order to achieve the best laser alignments and deliver the highest laser power to the sample. A digital power meter with a slim Si sensor was used for this purpose. For safety purposes, an attenuator was used to minimize the laser radiation power during alignment of the system.

During testing, it was found that the system alignment was sensitive and there was a deviation of the FP beam spot upon variation of the laser temperature, so the system was re-aligned and the overlap of the laser beams was checked after every single measurement.

In this work, an HP 71452B OSA [9], was used to monitor the lasers' emission spectrum while each THz measurement was being carried out.

5.2.3 Detection System

Fig. 5.7 illustrates the detection system schematically, consisting of the following main parts:

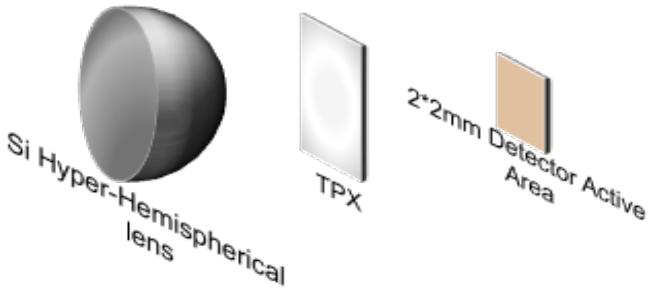

Figure 5.7 Detection part of the experiment measurement setup

- **THz Optics**

Since the THz radiation may be divergent, a specific lens should be used in order to collect and deliver the THz radiation to the detector. To this end, a hyper-hemispherical Si lens made of high permittivity silicon (ε_{Si} = 11.7) from TYDEX was used in this work, since the refractive index of the material matches well with that of GaAs (thus improving the THz coupling through the sample), and because it has a very low absorption at THz frequencies [10]. The Si lens also sharpens the THz radiation pattern and improves the directivity.

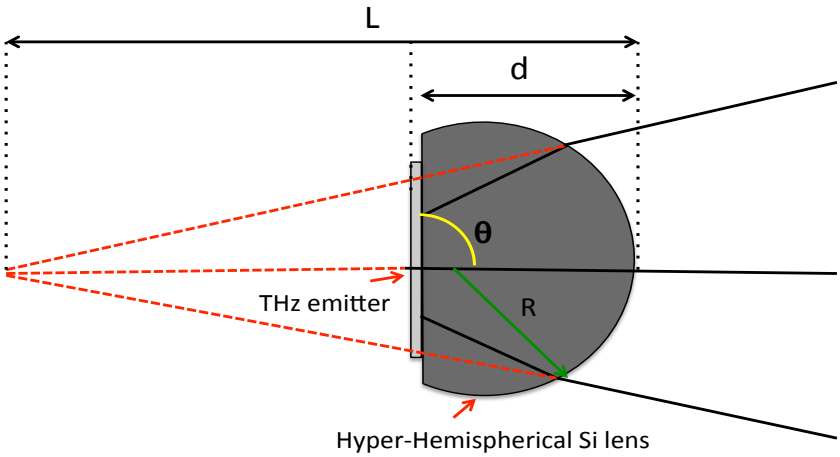

Figure 5.8 Hyper-hemispherical silicon lens combined with the sample

A ray diagram of the lens system is shown schematically in Fig. 5.8. The distance between the virtual focus point behind the lens and the tip of the lens (L), the distance (L), and the emission angle (θ), were calculated to be ~ 60 mm, 73°, respectively, for a hyper-hemispherical lens with a diameter of 25.4 mm. Although a thin layer of glue between the lens and substrate can be used to enhance the coupling, in this experiment the lens was attached to the back of the sample gently without using any glue, since it was necessary to remove the lens when the laser beam alignments were investigated in advance of the THz measurements.

- **THz Radiation Detector**

A GENTEC room temperature pyroelectric detector, model THZ 21-BL-BNC, was used to detect the THz radiation. This has an active area of 4 mm^2, with a sensitivity of 140 kV/W, and a noise equivalent power (NEP) of 4×10^{-10} $W/(Hz)^{1/2}$ [11] . Also the predicted absorption efficiency is ≈10% [12].

Since this kind of detector is very sensitive to wide range of the electromagnetic radiation; A TPX (Rexolite) filter was placed carefully in the front of the active area of the detector in order to block any unwanted near infrared light impinging upon the detector. Fig. 5.9 shows the TPX window for spectra ranging between 20-2000 μm, with ≥ 80% transmission when operated between 80-2000 μm.

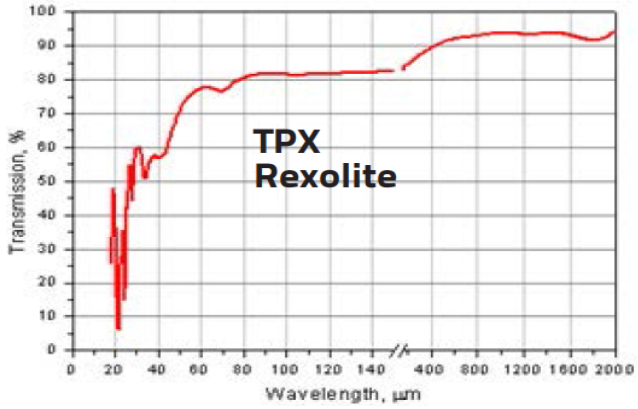

Figure 5.9 TPX (Rexolite) has a window covering spectra ranging from 20 to 2000 μm

A lock-in amplifier was used to process the signal, since the THZ21-BL-BNC integrates an analogue module that enables users to plug the head directly into the amplifier [12]. Since the instantaneous polarization of the pyroelectric detector changes in respect to the temperature change rate [10], an optical chopper set was applied to the path of the FP laser beam at 2 Hz, in order to provide the required source of modulation to heat and cool down the detector. Furthermore, tuning the laser and switching to different frequencies interrupted the system alignments. A careful alignment procedure was therefore employed until the maximum signal was recorded for each THz radiation frequency measurement. It was also found that the detector was very sensitive to any vibration around the laboratory, so most of the data was taken during out-of-hours periods so as to enhance the accuracy of the measurements.

5.3 Absorption, Reflection and Transmission through the QB Structure

When a light beam is incident on the surface of an optical medium, part of it is reflected and the remainder propagates to then be absorbed or transmitted through the medium. Fig. 5.10 illustrates this schematically [13] .

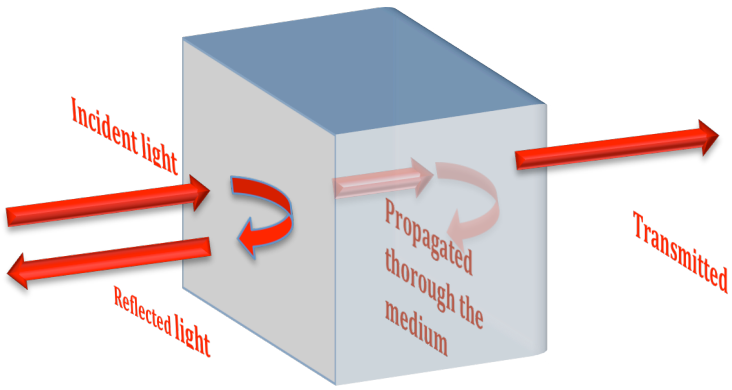

Figure 5.10 Schematic of the reflected and the propagated light at the normal incident angle to the optical medium

For a multilayer optical medium with different refractive indices, such as our sample structure attached to glass or diamond, some of the incident light beam is reflected at each interface between the two surfaces and the remainder is either absorbed or transmitted to the next layer.

Fig. 5.11 shows a schematic diagram of the prepared sample structure and how the normal incident light to the surface is reflected and propagates through each layer with a different refractive index at the wavelength 848 nm. The refractive index of the GaAs is 3.65 at 848 nm [14].

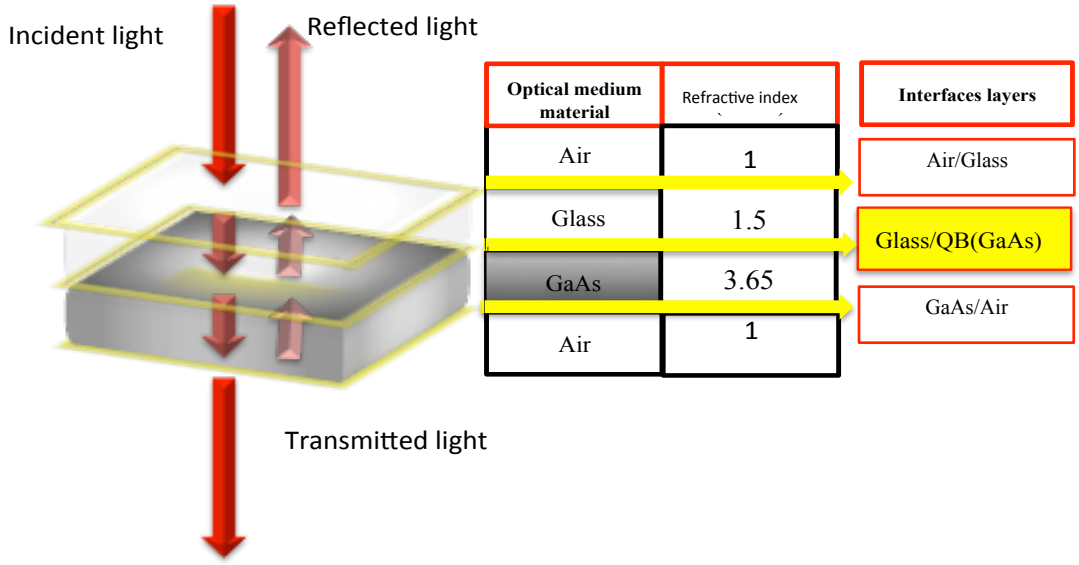

Figure 5.11 Schematic of prepared sample structure layers with their different refractive indices

The reflection coefficients at each interface can be calculated by [15]:

$$R = \left(\frac{n_1 - n_2}{n_1 + n_2}\right)^2 \tag{5.1}$$

where

n_1: refractive index of the first optical material,

n_2: refractive index of the second optical medium.

The conservation of energy can be represented by [13].

$$R + T + A = 1 \tag{5.2}$$

Assuming that the air and glass are totally transmissive to the incident light beam, the absorption $A = 0$, and the transmission coefficients of the incident light beam are therefore calculated by:

$$T = 1\text{-}R \tag{5.3}$$

The transmission coefficient can be defined as the ratio of the output signal power to the input signal power [13].

$$T = \frac{P_{output}}{P_{input}} \tag{5.4}$$

Using equations 5.1, 5.3 and 5.4, the fraction of the output power to the incident power can be found by:

$$P_{out} = P_{in}\left[1\text{-}\left(\frac{n_1\text{-}n_2}{n_1+n_2}\right)^2\right] \tag{5.5}$$

Based on the above equation, table 5.1 shows the calculated output of the light signal to the input for the system described in 5.2.

Optical medium	Incident power	Output power	Absorption
Air		P_0	No absorption
Glass	P_0	$P_1=P_0\times0.96$	No absorption
First layer of the sample	P_1	$P_2=P_1\times0.825$	A=1-T $A=1-(P_2^*/P_2)$
Last layer of the sample	P_2^*	$P_3=P_2^*\times0.68$	
Air	P_3		No absorption

Table 5.1 Output power to incident power fraction in each layer, and possible absorption in the layers

The assumption was made that the air and glass are totally transparent to the light beam, and the light beam was absorbed only in the sample structure. The power of the initial incident input signal, P_0, and of the transmitted light beam through the sample to the air, P_3, were measured experimentally using the apparatus illustrated schematically in Fig. 5.12.

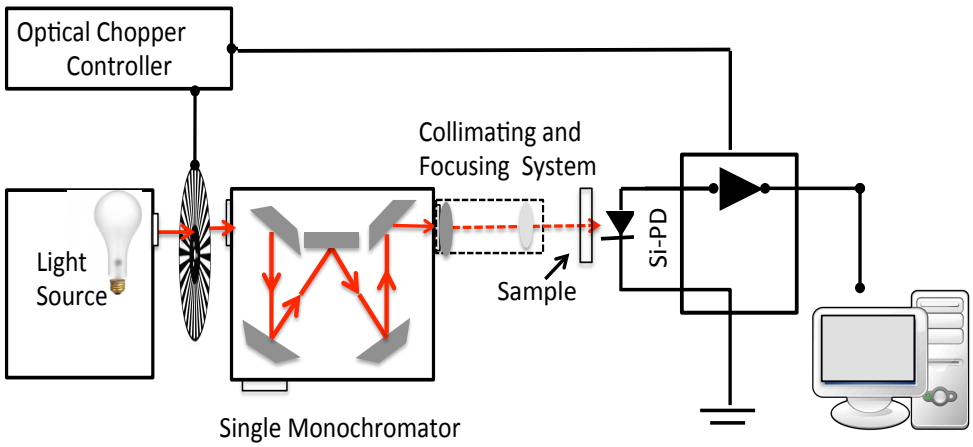

Figure 5.12 Schematic diagram of the setup used for light signal measurementss

A Tungsten lamp source with a wide wavelength range was used as an optical source. The light from the Tungsten source was passed through a monochromator to select a narrow wavelength band; a Bentham 300M was used in this setup. Lenses were used to focus the light to a circular diameter of less than 1 mm, so as to make sure all the light passed through the copper disk with a 1 mm hole in the centre.

A silicon photodiode detector SM05PD1A from Thorlabs was used to detect and measure the light signal; a lock-in amplifier and mechanical chopper were used to process the detected signal, and Labview was installed on the PC and used to record the signal data, specifically, the photodiode measured a signal current, and then this signal current was converted to a signal power, corresponding to the diode responsivity.

The diode responsivity is defined as the ratio of the photocurrent I_{pc} to the optical power P, and is given by:

$$\text{Responsivity} = I_{pc} / P$$

The measurements were completed by measuring the light signal passing through the copper disk when the sample was not attached, followed by attaching the sample to the copper disk and measuring the signal of the light transmitted through it.

A schematic diagram of the prepared sample attached to the copper disk is shown in Fig. 5.13.

Both measurements were made at the same resolution (0.1 nm) for the monochromator and also for the same wavelength range, 835-870 nm.

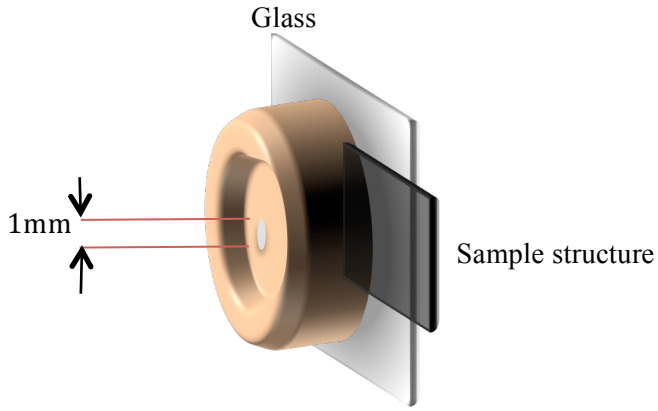

Figure 5.13 Schematic diagram of the sample and copper disk

Only the absorbed power in the sample structure actually contributes to the process of producing the THz signal. By substituting the measured P_0 and P_3 signal in column 3, table 5.1, the coefficient of absorption of the propagating optical power in the sample structure was obtained (column 4, table 5.1). For simplicity the slight change in the refractive index was ignored, and only one value at 848 nm was used in all the calculations. In addition, it was assumed that the sample structure was comprised of only one layer of GaAs. Fig. 5.14 shows the absorption spectrum of the propagated light beam into the device structure together with the photocurrent spectrum, which was produced in section 3.6.

Two main peaks are present in the absorption spectrum, at 1.453 eV and 1.462 eV, associated with excitonic transition between the first quantized levels in the conduction and valence sub-bands, E1-HH1 and E1-LH1, respectively.

The figures also shows a slight difference in the excitonic transition peaks of the absorption spectrum compared to the photocurrent spectrum, for E1-HH1 transition a 1.3 meV blue shift, whilst for the E1-LH1 transition a 2.7 meV red shift occurs

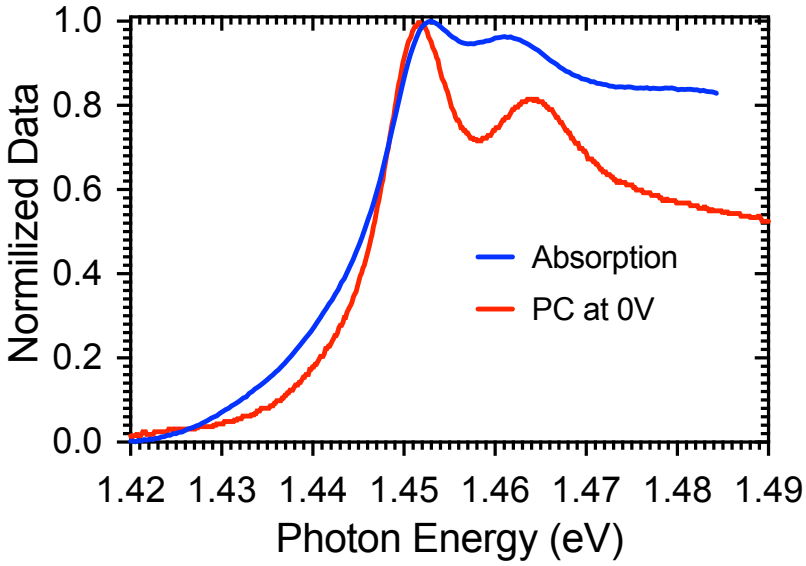

Figure 5.14 Absorption spectrum for propagated light through the sample (blue line), and the photocurrent spectrum (red line), both measured at room temperature

This shift cannot be adequately described by a variation in the QW width, since both transitions would shift in the same sense. Similarly, a reduction in the E-field caused by the removal of p-doped and n-doped materials cannot explain these changes in energy. It is noteworthy that the electric field would be expected to be unchanged as thick (1.5 μm) highly doped $Al_{0.4}Ga_{0.6}As$ layers ($1\times10^{18}cm^{-3}$) remain.

The change in energies is therefore tentatively explained as follows. With the substrate, intact GaAs layers are unstrained, whilst AlGaAs cladding layers and AlAs barriers are under compressive Bi-axial (in plane) strain since the AlAs lattice constant is 1.4% larger than that of GaAs. Upon removal of the GaAs substrate and cap layer, however, the 'substrate' material can be considered to be the $Al_{0.4}Ga_{0.6}As$ cladding layers. In this case, since the GaAs quantum well has a smaller lattice constant it will be under tensile strain and this, it is suggested, results in the band structures of GaAs being modified with a reduction in the conduction band energy and an increase in both valence band energies [16]. The valence band degeneracy is accordingly lifted, since a light hole has a higher energy. These changes in band-

structures qualitatively explain the small change in the absorption spectra once the substrate is removed.

Additionally, in-situ absorption measurements of the sample were carried out while 260 mW of laser power was applied to the sample. Fig. 5.15 shows these absorption measurements (circles) plotted with the transmission spectrum obtained previously.

A digital power meter was used to record the laser-transmitted power through the 1 mm hole (copper disk), both with the sample at P_3, and without the sample at P_0 at each photon energy. The same calculation procedure as used previously was applied to calculate the absorption through the sample structure. The results agreed quite well with the absorption spectra.

Since there is no shift in the excitonic transition energies of the two absorption spectra, no change occurred to the band energy of the sample material.

It is therefore clear that the sample temperature was not significantly affected by the laser beam, even when the power of the laser was reasonably high.

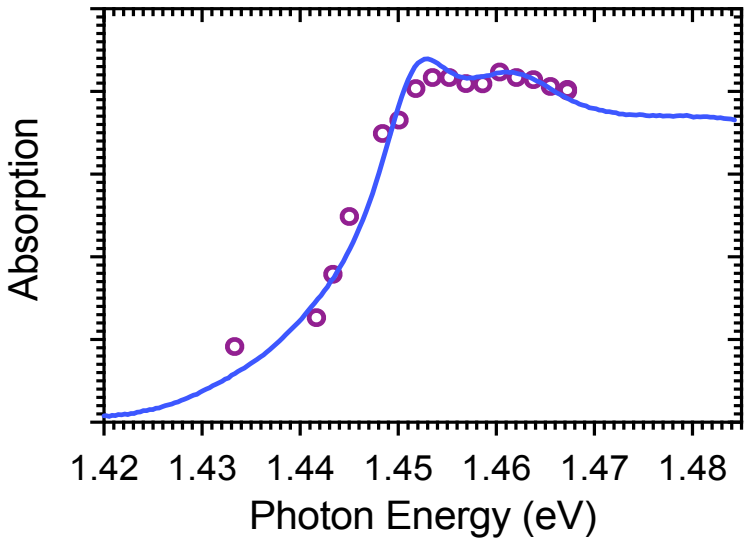

Figure 5.15 Absorption spectrum for propagated light through the sample (blue line). Closed circles are the in-situ absorption measurement results. Both were measured at room temperature

Additionally, the excitons peaks are not bleached, indicating that the carrier density is sufficiently low to allow the excitonic effect to be observed.

Direct thermal imaging of the sample was undertaken in order to investigate any change in the temperature of the sample, in addition to seeking evidence for the shift in the absorption spectra. Fig. 5.16 shows the thermal image of the back of the sample (a) before and (b) after directing the laser to the sample (laser applied for 15 minutes and photo taken instantly after switching the laser off).

The temperature change in the sample was 0.6 °C, which would result in a 0.25 nm change in band gap. This is insignificant, and in line with the results in Fig. 5.15.

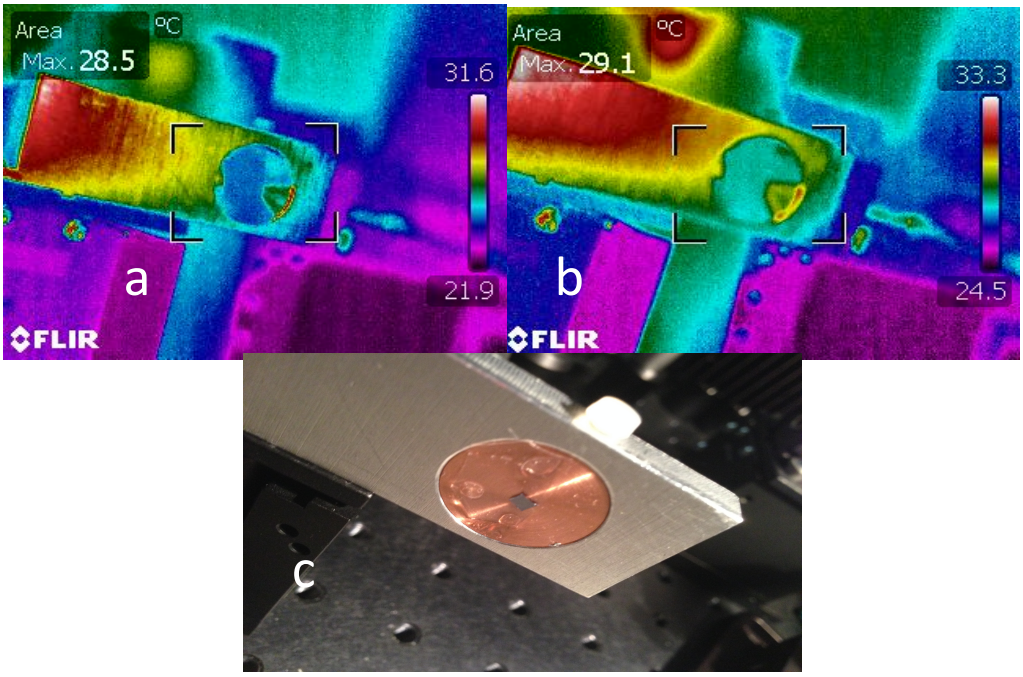

Figure 5.16 Thermal image of the sample (a) before the laser was applied (b) after the laser was applied, (c) photograph of the sample attached to the copper disk

5.4 THz Preliminary Measurements Results

Fig. 5.17 (a) plots the spectrally resolved absorption spectrum of the sample, and the emission spectra of the two lasers, collected by the OSA in the experimental setup. The two-semiconductor lasers wave operated at a total power of 260 mW (130 mW each), incident normal to the sample surface. The green and red arrows indicate the tuneability of the two lasers. With the lasers resonant with E1-HH1 and E1-LH1, a clear THz emission signal with power ≈ 1 μW was detected on the opposite side of the sample to the laser excitation using the pyroelectric detector and only 0.4 μW background noise was recorder (explained in the experimental setup in section 5.2).

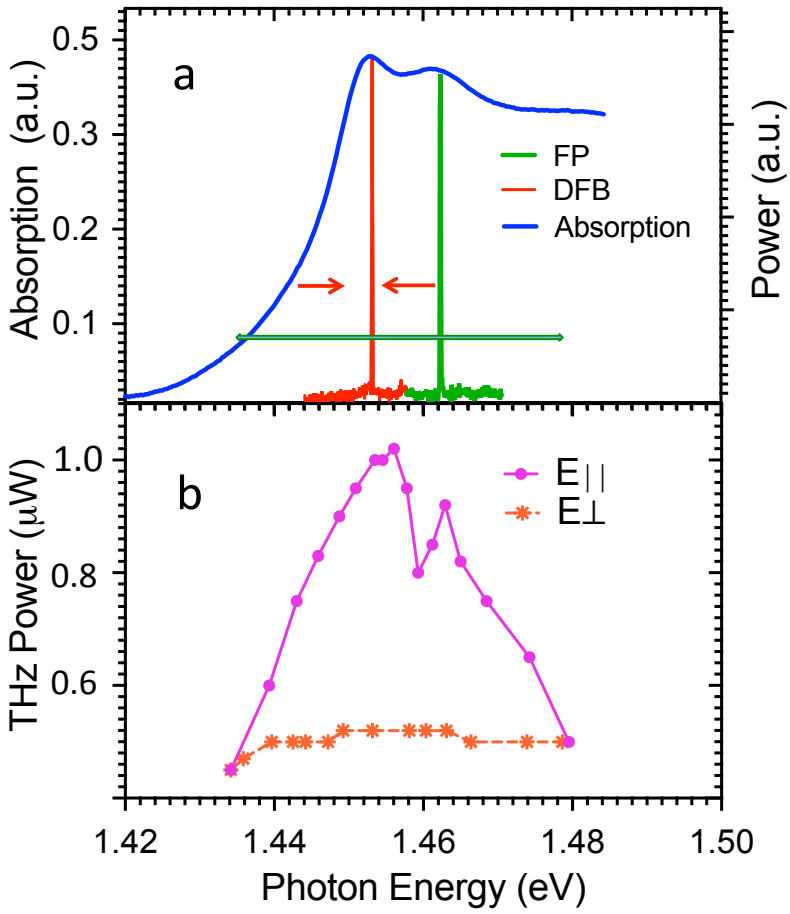

Figure 5.17 (a) absorption spectrum of the sample, and λ_1 and λ_2 resonance with E1-HH1 and E-LH1 transitions, (b) shows the THz wave power obtained through the excitation of the sample with respect to the lasers polarization

Fig. 5.17 (b) plots the measured THz power obtained in our system with both pump lasers operating at 260 mW as a function of the energy of the frequency tuneable laser (FP) with the other laser (DFB) resonant with the electron-heavy hole exciton. The THz power is measured for the lasers in collinear and crossed polarization. A clear signal is observed for collinear polarized pump sources that follow the envelope of the exciton resonances. The difference with the case for crossed polarization is marked, with the much smaller signal in this case being attributed to background black-body radiation.

To investigate this further, the power dependency of this signal was measured. Fig. 5.18 plots the power dependence of the THz power as a function of the total laser power absorbed in the sample (n. b. this is ≈ 27% of the incident power as determined by the transmission measurements) excitation was at 850 nm DFB. A graded ND filter was placed in the path of the laser beams in order to attenuate the total excitation power. A quadratic variation of the THz power indicates that second order non-linear effects are responsible for the THz generation process.

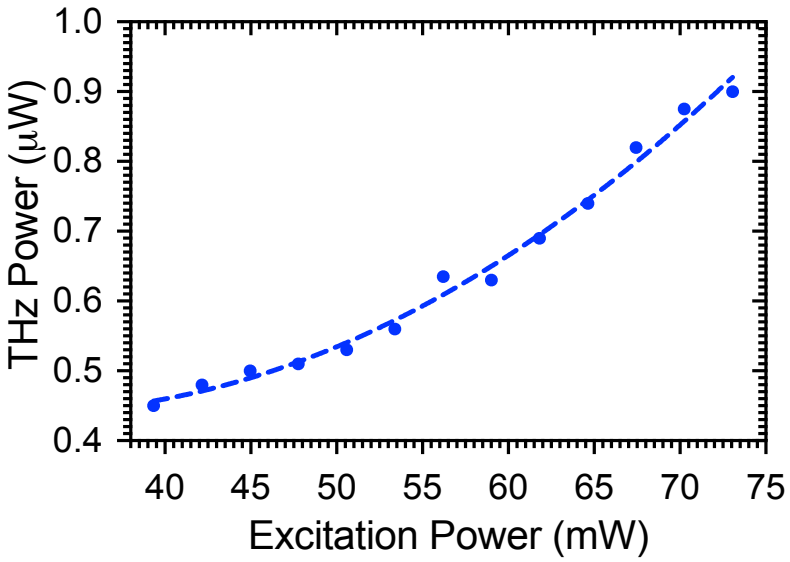

Figure 5.18 THz-Laser power dependence measurements and the quadratic fitting (dashed line) of the data

Fig. 5.19 shows the measured THz signal versus the estimated THz radiation based on the QB (i.e. E1-LH1). It is clear that the THz signal does not follow the LH absorption alone (which would be the case if the THz emission signal was due to the Quantum Beating (QB) with all excitation absorption resulting in THz generation).

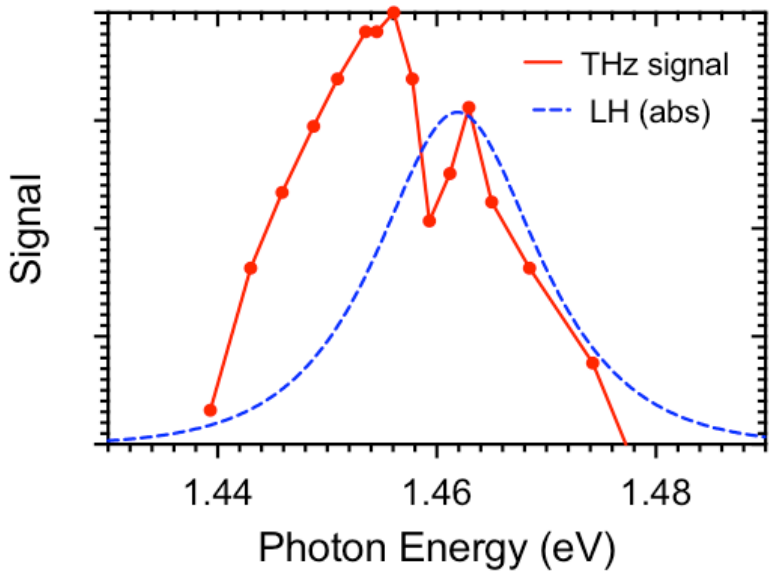

Figure 5.19 Illustrates the measured THz signal and the estimated THz signal emitted based on QB

A maximal conversion efficiency of 1.2×10^{-5} was obtained through second order non-linear excitonic effects at room temperature, using readily available CW laser diodes and a simple structure. We note that this was without the use of plasmonic effects or any kind of antenna, and without applying an E-field to the structure. And this efficiency could be improved by using a higher laser power or focussed lasers, since saturation was not observed. Further details about these findings will be discussed in the next chapter.

5.5 Conclusion

A tuneable THz signal was observed using readily available CW laser diodes and a simple experimental structure. THz signal generation based on a second order non-linear χ^2 was confirmed, and therefore the THz signal is not due to the QB as would have been expected, and could be tuned more widely than the QB estimated signal. A maximal conversion efficiency of 1.2×10^{-5} was achieved, which could be improved by using lasers with a higher power or focussed optics.

5.6 Future Work

In the following chapter more detailed investigations of the THz generation process are performed.

References

1. Kressel, H., Butler, J.K.: Semiconductor Lasers and Heterojunction LEDs. Academic Press, London (1977).

2. Panish, M.B.: Temperature Dependence of the Energy Gap in GaAs and GaP. J. Appl. Phys. 40, 163 (1969).

3. Govind P. Agrawal, N.K.D.: Semiconductor Lasers. Kluwer Academic Puplishers (1993).

4. Morthier, G., Vankwikelberge, P.: Handbook of distributed feedback laser diodes. Artech House (2013).

5. Yariv, A.: hypermespherical si lense. Oxford University Press, 1997.

6. Kunii, T., Matsui, Y.: Narrow spectral linewidth semiconductor lasers. Opt. quantum Electron. 24, (1992).

7. Kojima, K., Kyuma, K., Nakayama, T.: Analysis of the spectral linewidth of distributed feedback laser diodes. J. Light. Technol. 3, 1048–1055 (1985).

8. Leonhäuser, B., Kissel, H., Tomm, J.W., Hempel, M., Unger, A., Biesenbach, J.: High-power diode lasers under external optical feedback. In: Proc. SPIE. p. 93480M (2015).

9. Analyzers, S.: HP 71450B/1B/2B Optical Spectrum Analyzers.

10. Lee, Y.-S.: Principles of Terahertz Science and Technology. Springer, New York, U.S.A (2009).

11. http://gentec-eo.com/Content/downloads/specifications-sheet/THZ-I-BNC 2014 V2.0.pdf.

12. http://gentec-eo.com/Content/downloads/absorption-curves/Curves THz 2014 V2.0.pdf.

13. Hecht, E.: Optics, 4th. , San Francisko, US (2002).

14. Adachi, S.: GaAs and related materials: bulk semiconducting and superlattice properties. World Scientific (1994).

15. Lipson, A., S. G., Lipson, H., Lipson, “Optical Physics”. 4th ed. Cambridge University Press; Cambridge; 2011.

16. Jain, S.C., Willander, M., Maes, H.: Stresses and strains in epilayers, stripes and quantum structures of III-V compound semiconductors. Semicond. Sci. Technol. 11, 941–671 (1996).

Chapter Six

THz Frequency and Power Dependence Measurements

6.1 Introduction

To summarise the previous chapter, THz emission was generated using an optical nonlinear process and at quite an efficient conversion efficiency. The radiation wavelength was not confirmed. Although, according to the filter specification, most of the radiation at a wavelength of > 20 μm would pass through it, it remains important to investigate the THz emission wavelength through measurements.

This chapter presents and discusses the results of THz emission wavelength measurements, as well as confirmation of the second order nonlinear coefficient by measuring the THz wave power as a function of the excitation lasers' power within a wide range of emission wavelengths. Furthermore the origin of the THz signal is discussed.

6.2 Tuneable THz Measurements

As described in the previous chapter, a compact THz setup was used to measure the emission power from the device, which was designed to be in the THz range (this range was found to correspond to the difference between the two lasers' wavelengths).

Fig. 6.1 shows the absorption spectrum of the device structure as described in section 5.3. This is made up of a step - like 2D density of state (D.O.S) function and two pronounced peaks that result from electron-heavy hole and electron-light hole quantum well exciton. The figure also shows the THz signal power generated for the collinear polarization lasers, following the exciton absorption spectrum for a certain range of emission wavelengths. The maximum terahertz power of 1.1 μW being recorded when the two lasers had a resonance close to that of the heavy hole excitons. The figure also illustrates a particular phenomenon for which there is currently no explanation, namely a significant fall in power in the range 1.456-1.462 eV, followed by an increase, before following the expected downward curve from 1.462 eV onwards. The nonlinear process has therefore been confirmed for the case of E-HH and E-LH excitation. However the wavelength of the radiation has not been confirmed, and the 2^{nd} order process has not been confirmed spectrally.

As in previous measurements a THz signal was measured on the opposite side of the sample to the laser excitation using a pyroelectric detector.

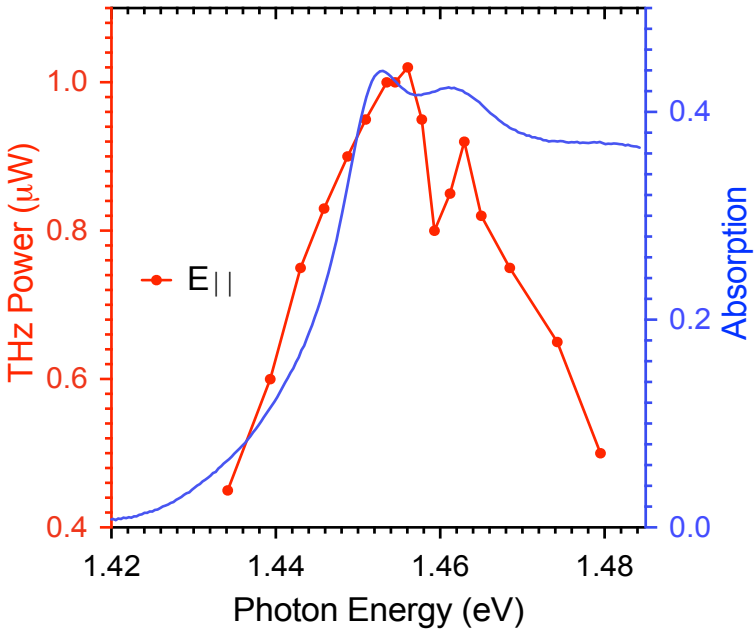

Figure 6.1 Absorption spectrum of the sample (in blue) and the THz wave power obtained through the excitation of the sample (in red)

The total power of the two lasers was fixed at 260 mW (130 mW for each laser beam). A continuously tuneable THz-wave in the range 0.2 – 6.7 THz was generated at room temperature, based on second order nonlinear excitonic effects in the GaAs/AlAs Multi-Quantum Well (MQW).

6.3 Experimental Setup for THz Frequency Measurements

In order to measure the THz frequency, the experimental setup that had been used for the THz emission measurements (described in the previous chapter), was modified by adding a Fabry-Perot interferometer (FPI). Fig. 6.2 illustrates the experiment's setup with this addition.

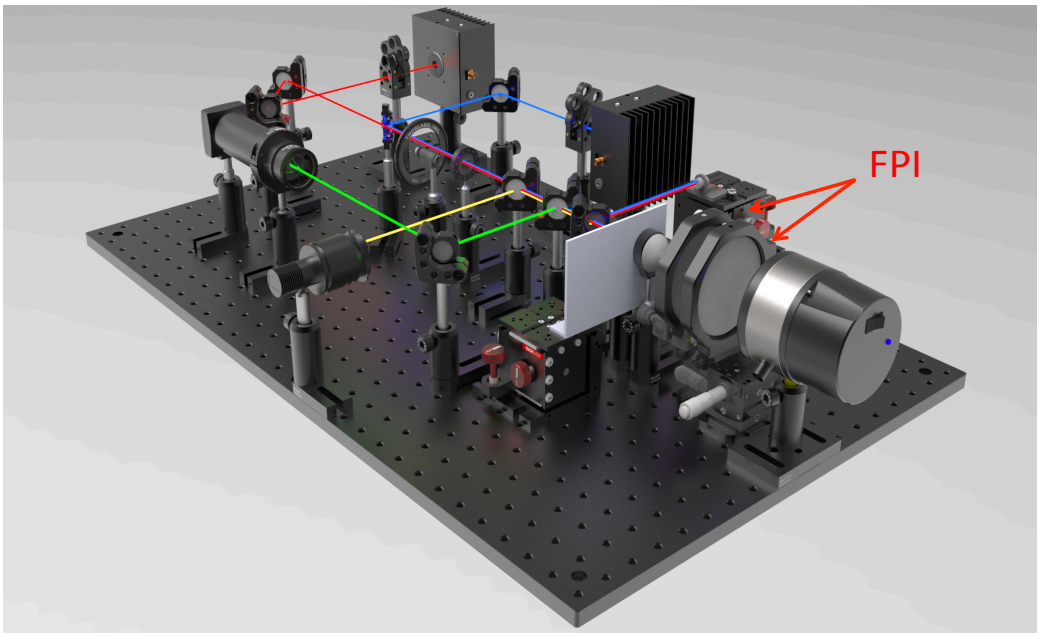

Fig. 6.2 Experimental setup including the Fabry-Perot Interferometer (FPI)

A simple FPI consists of a pair of partially reflective flat mirrors spaced micrometres-to-centimetres apart, with their reflective surfaces facing each other [1, 2].

In our experiments, two identical thin (525 μm) thick, 4" semi-insulator Si wafers, single side polished, were aligned as parallel as possible to form an FPI, as shown in Fig. 6.2. The Si wafer was chosen as it is readily available, and also because Si has a low imaginary part of the refractive index/lower absorption at the THz frequencies of interest [3].

One wafer was fixed on a mount and the other was mounted on a micrometer translation stage in order to be able to alter the cavity length, which is defined as the separation between the two partially reflecting surfaces between both reflectors. The schematic of the FPI is shown in Fig. 6.3.

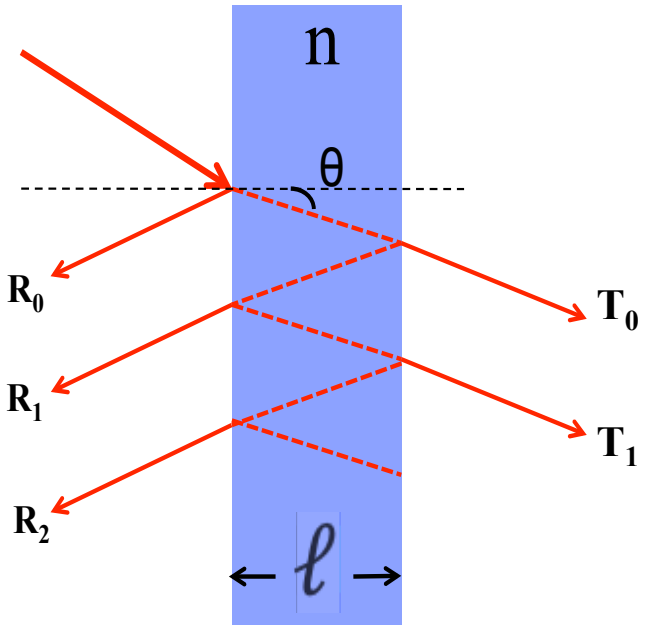

Figure 6.3 Fabry-Perot interferometer, the THz wave radiation incident on the interferometer and undergoes multiple internal reflection

The transmittance function of the Fabry-Perot interferometer is given by Eq. 6.1.

$$T = \frac{1}{1+F\sin^2(\frac{\delta}{2})} \tag{6.1}$$

where

T: is the transmittance

F: the finesse

And δ the phase difference between each successive transmitted pair (i.e. T_0 and T_1), δ is given by Eq. 6.2.

$$\delta = \frac{2\pi}{\lambda} 2nl\cos(\phi) \tag{6.2}$$

where

c : speed of light in a vacuum

ϕ: incident angle at which the light travels through the interferometer

l : thickness of the interferometer

n: refractive index of the material between the two reflecting surfaces (n).

The coefficient of finesse of the interferometer is calculated by Eq. 6.3.

$$F = \frac{4R}{(1-R)^2} \tag{6.3}$$

The constructive and destructive interference effects between the two reflecting surfaces originate the transmission function of the interferometer. Maximum transmission happens when the optical path length difference between the incident and reflected waves is an integer multiple of half the wavelength.

The reflectance coefficient, is yielded by Eq. 6.4 [4].

$$R = \left(\frac{n_1-n_2}{n_1+n_2}\right)^2 \tag{6.4}$$

where

n_1: refractive index of silicon,

n_2: refractive index of air

By combining all of the equations above, the transmittance coefficient T is

$$T = 1/[(1 + (\frac{4[(n_1-n_2)/(n_1+n_2)]^2}{[1-[(n_1-n_2)/(n_1+n_2)]^2]^2 \times \sin(\frac{4\pi l/\lambda}{4})^2}] \tag{6.5}$$

And by substituting the relevant values in Eq. 6.5, it is possible to calculate the fraction of transmitted radiation. This is done later when fitting the measurement results.

The refractive index of the Si ≈ 3.41 [5], and the reflectance is calculated to be 29% at a normal incident.

6.4 THz Frequency Results Measurements

Fig. 6.4 shows the signals measured for the THz emitter as the FP laser wavelength was tuned across the absorption spectrum. The laser excitation system was set at the maximum power of 260 mW at a series of different frequency separations, which produced a measurable THz signal. According to previous measurements it should be possible to tune the emitted high single THz wave across a range of 0.2-6.7 THz, hence, here, it was attempted to measure the frequency of the electromagnetic wave to confirm both that they were emitted through different frequency generations, along with the second order nonlinear optical coefficient χ^2 of the device.

The emission wavelength measurements were carried out by following the steps below:

- As the emission from the device was predicted to be due to difference frequency generation (DFG), three different points (A, B, C) were determined on the absorption spectrum, taking into the account the tuneable THz signal that had been measured previously. The FP laser was then set to offer resonance with each point, while the DFB laser wavelength was fixed,

to be in resonance with the heavy hole band. The difference in the photon energy results from the different frequency generation (DFG) were calculated, as shown in Fig. 6.4.

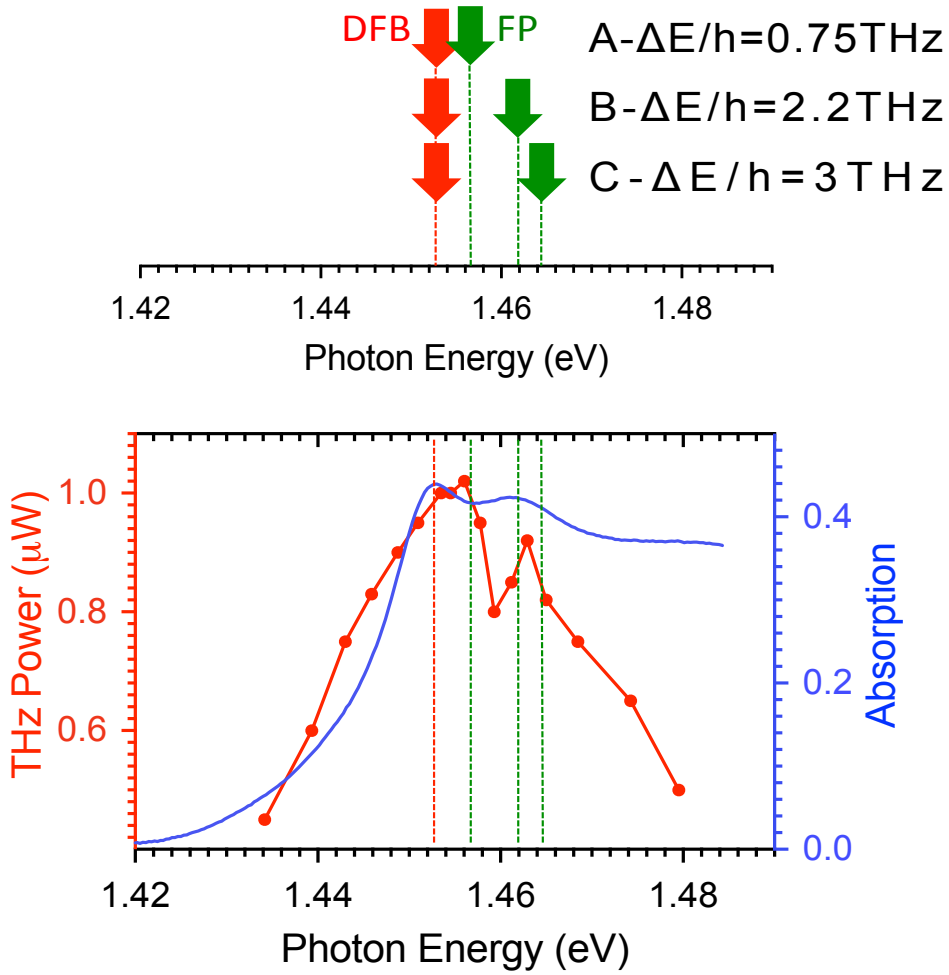

Figure 6.4 Absorption spectrum of the sample in blue, showing the DFB laser to be resonant with E1HH1, and the FP laser to be resonant with three different areas in the absorption spectrum A - 1.456 eV, B-1.462 eV, and C-1.456 eV. The figure also shows the THz wave power obtained through the excitation of the sample

- The emission wavelength generated for the three cases A, B, C was measured and found to match well with the predicted emission wavelength (based on DFG). This was measured by using the FPI (described in section 6.3). The flatness of the wafers and the space between then were investigated by

contacting the wafers to each other and shining light at their edge; if they were well aligned and attached to each other along the diameter, the light should not be able to pass through them. Fig. 6.5 illustrates the measurement setup, including the FPI. The two lasers were linearly polarized and a pyroelectric detector was used to measure the transmitted THz power. The collected THz wave illuminated the surface of the FPI at a normal incident angle.

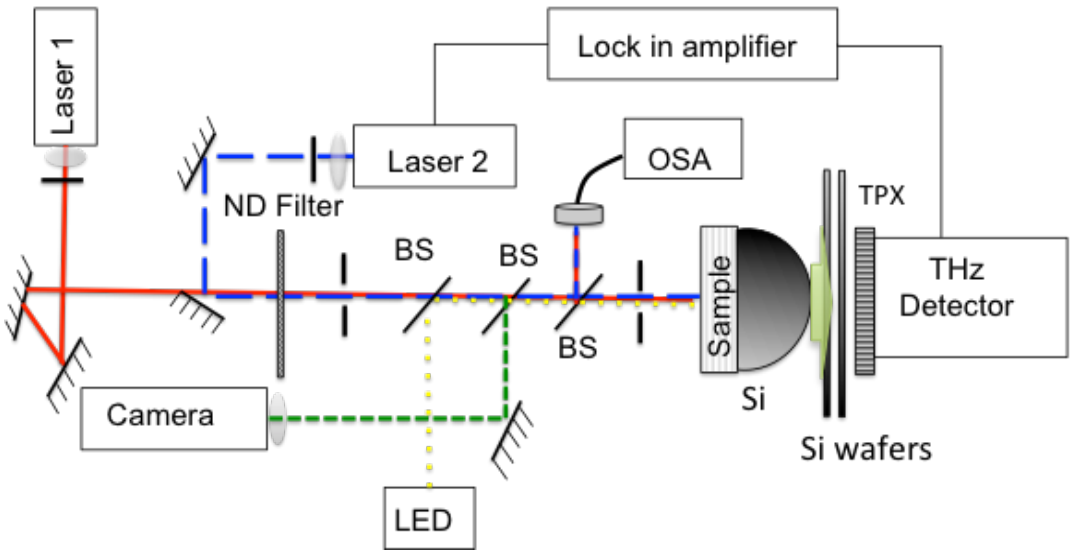

Figure 6.5 Schematic diagram of the THz measurements setup

The THz output wavelengths were measured by scanning the Si-based interferometer. Fig. (6.6-A, B, C) shows the signals detected for the three excitation cases, A, B and C, respectively, corresponding to the translation stage position. Fits were made using MATLAB which are solutions to Eq. 6.5.

Fig. 6.6-(A) shows the signal detected, together with the fit to the data, where λ is the fit parameter transmission peaks observed for A with repeats of ~ 387 μm as the

mirror displacement was changed, confirming emissions at ~ 0.77 THz, according to the oscillation of the Fabry-Perot. Whilst a fit at 0.75 THz is acceptable, this fit at 0.77 was considered optimal. This is in agreement with the broadening of the THz wave ≈ 25 GHz (due to one of the lasers having a broader linewidth than expected emission spectrum).

According to Fig. 6.6-B, the output wavelength was 126 μm, which is close to 136 μm, calculated from the two pump wavelengths, confirming emission at ~ 2.3 THz. Hence, there is a degree of concordance between the experimental data and the theory.

Fig. 6.6-C shows the transmission peaks observed for C with repeats of ~ 102 μm, with respect to the mirror displacement, which agreed well with the calculated data 99 μm (3.04 THz), and confirming emission at ~ 3.1 THz.

Whilst quite close, the experimental data is not in perfect agreement with the theoretical values. This is attributed the THz wave was not collimated and the finesse of the interferometer is quite poor.

Additionally, I note that the line width of the THz emitter could not be measured accurately since the interferometer had a low finesse.

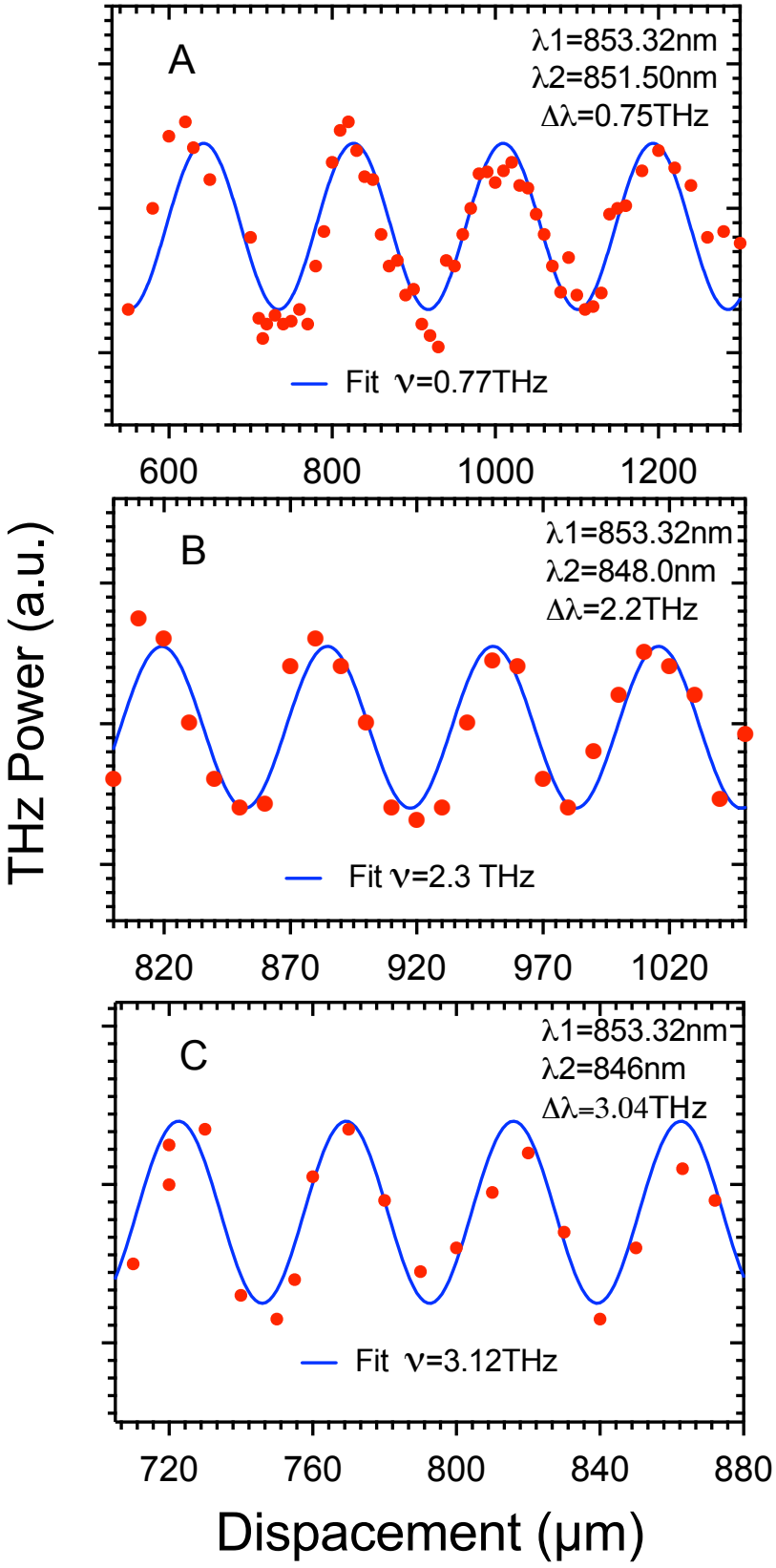

Fig. 6.6 THz power being transmitted through a Si interferometer as a function of the displacement between two Si wafers. The solid line is the theoretical fitting to the data at three different frequencies. A- 0.77 THz, B-2.4 THz, C- 3THz

Subsequently, the THz power dependence was measured at each of these three THz wavelengths. In order to control the lasers' power, a graded ND filter (from Thorlabs) was added to the path of the laser beams to adjust the lasers' power. The system was aligned prior to each measurement. The results are plotted in Fig. 6.7. In addition, the data points were fitted using a quadratic dependence, which corresponds to the dashed curve in Fig. 6.7. The data measured for all the cases A, B, and C clearly displays the quadratic dependence that is the typical characteristic of DFG [6], and which demonstrates the second order nonlinear process at all three frequencies. Also, based on the data presented in Fig. 6.7, it is evident that the device can emit efficient THz wave power, which indeed will be used for spectroscopic applications in the next chapter; its efficiency could be increased. Since bleaching was not observed in any of the absorbed power levels in the sample the efficiency could be increased by increasing the lasers' power density.

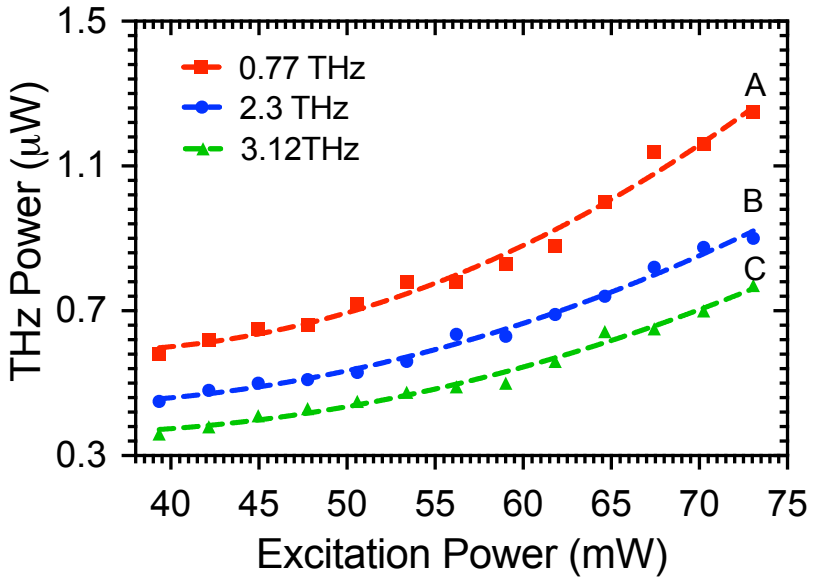

Figure 6.7 THz power as a function of the total power from the lasers absorbed by the sample

6.5 Discussion of Origins of THz Signal and Summary

Since the power dependence measurements confirmed the THz generation through second order nonlinear effect in GaAs/AlAs QWs.

This section describes the possible origin of the CW monochromatic, tuneable THz wave generation that has been observed in this work. Quantum well (QW) excitons are a 2D coherent elementary excitation, giving rise to a macroscopic transition dipole moment, that have been predicted to exhibit high χ^3 optical nonlinearities due to the combination of this macroscopic transition dipole moment and the rapid radiative and non-radiative decay of the excitons [7]. Fig. 6.8 (a) shows the dispersion of excitons and electron-hole pairs. Upon resonant excitation, the exciton may recombine radiatively (~2-3 ps) [8], or be thermally ionized through phonon scattering (~ 0.3 ps) [9]. The rapid radiative decay and thermal ionization of the excitons acts to push the exciton away from behaving as an ideal Boson, enhancing χ^3. A further macroscopic enhancement of χ^3 by a factor $(L/a_B)^2$ for near-resonant excitation (L= coherently excited QW area, a_B exciton radius), is possible as long as spatial coherency of the pump light and exciton is maintained [7]. As this effect utilizes the imaginary part of χ^3, corresponding to absorption saturation/state filling effects, Coulomb enhancement of χ^3 effects may also occur due to screening, band-gap renormalization, and Coulomb interactions [10].

Symmetry breaking is known to result in effective χ^2 processes being realised from high χ^3 materials. This can be achieved by the application of an electric field, such as those found at a semiconductor surface [10], or within a p-n junction [11]. The third-order nonlinear susceptibility χ^3 is converted to χ^2 as the dipole moments orient themselves in the direction of the applied field, enabling many important second-order non-linear processes [12]. Electric-field-induced second harmonic generation

(SHG) was initially used for the extraction of semiconductor material parameters from semiconductors [13], and field measurements of silicon metal–oxide–semiconductor (MOS) transistor interfaces. Here we utilize this conversion process for the conversion of χ^3 to χ^2 in a resonantly excited exciton system.

Fig. 6.8 (b) shows a schematic of the multi-quantum well structure to convert χ^3 to χ^2 processes, designed so as to have E1HH1 and E1LH1 resonances accessible by commercially available semiconductor lasers operating at ~ 850 nm. Additionally, overlapping excitonic transitions allow a contiguously broad tuning range for difference frequency generation. The built-in E-field due to the unbiased p-n junction (26 $kVcm^{-1}$) is sufficient to provide electron and hole wave-function separation of 7 nm, which is comparable to the QW width. For this proof-of-concept work, a detailed study of the optimal QW E-field, and QW number has not yet been conducted.

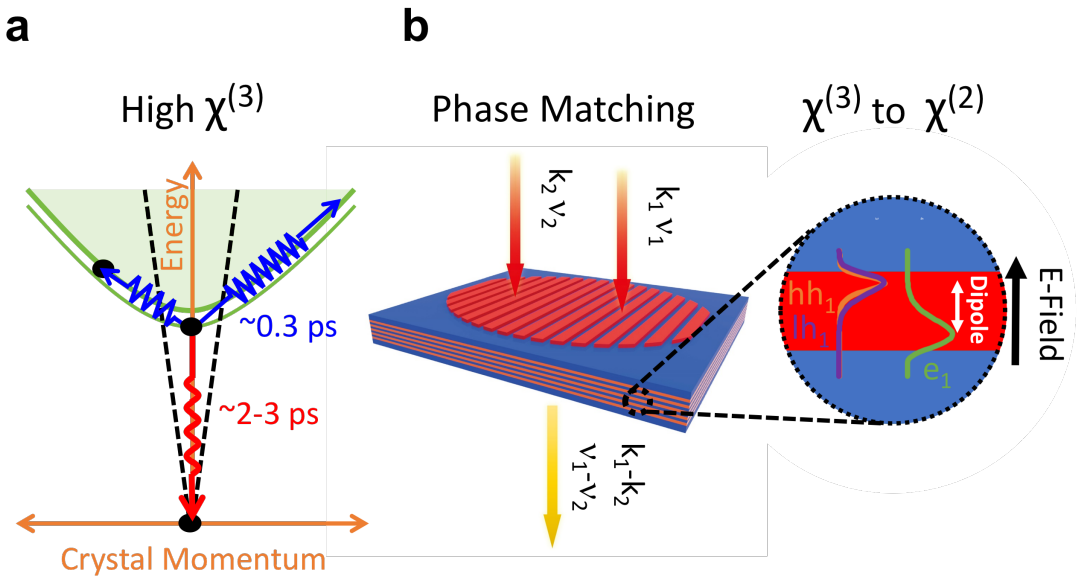

Figure 6.8 Schematic showing the concept for our broad spectral band-width THz emitter. High $\chi^{(3)}$ is obtained (a) via resonant excitation of excitons in a semiconductor quantum well. Phase-matching is achieved in-plane, through excitation in normal incidence (b), and this yields high $\chi^{(2)}$ processes through the application of an internal electric-field (c).

To summarize tuneable THz-wave generation was demonstrated in an MQW structure based on DFG using two CW lasers with slightly different wavelengths. The frequency of the THz wave was tuned in the 0.77 to 3.2 THz range by varying the FP laser in respect to the absorption spectrum of the device. The maximum power was obtained at 0.77 THz when the FP laser frequency was in resonance close to the HH exciton. Three different frequency measurements were presented here and the power dependence measurements confirmed the quadratic dependence of the THz emission power with regards to the absorbed power from the lasers. Fig. 6.9 plots the possible THz power levels at each THz frequency knowing the two pump frequencies. I note that a strong THz signal is observed when both pump lasers are resonant with E-HH exciton. This confirms that the generation process is not via a quantum beat (QB). Possible generation processes have been discussed. This device proved to be a source for generating single frequency waves, widely tuneable between 0.2-6.7 THz.

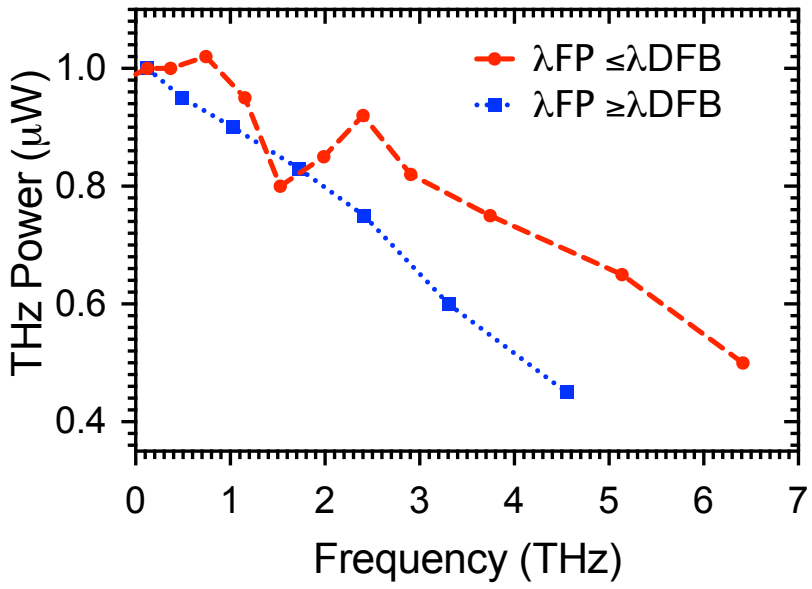

Figure 6.9 Continuously tuneable THz-wave emitted from the experimental device in the range 0.2–6.7 THz

It became clear that this tuneable THz-wave system, that consisted of a DFG-based THz-wave source with a pyroelectric detector, would be beneficial in practical THz-imaging, THz-sensing and spectroscopic applications. Subsequent experiments were therefore carried out using this system, as described in the next chapter.

6.6 Future Work

Fourier transform infrared (FTIR) spectroscopy can be used for measuring the linewidth of the THz signal and also identified the frequency for different THz signals more accurately and within a short time and less effort.

Since it is believed that the electric field play a big role in generating the THz signal it is worthy of further investigation. An increased electric field can be expected to increase the electron-hole wave-function separation and hence increase χ^2. However, an increased E-field, and electron-hole wave-function overlap will also reduce absorption, which will act to reduce the THz power generated. Investigation of the trade-offs would allow an optimal sample design to be realized.

There are two possible routes to make an E-Field study. Creating a sample with contacts to allow a bias to be applied would allow a wide range of E-Fields to be studied, but creating such a device poses significant challenges. Since the metal tracks patterning on glass/diamond is required, and also n and p contacts on sample (these would have to be gold plated to increase the height of contacts and soldered.

An alternative route is to have a series of samples grown where the intrinsic region width is changed to vary the built in electric field. This would be simple to implement within the existing system, as new samples could be readily fabricated as laid out in chapter 3. However, new epitaxial growths may require additional funds/time, and each sample allows only one E-field to be investigated. There would

be some additional uncertainty as different samples are used. Careful characterisation of the materials would be required to ensure that their quality was comparable in each growth run. Such variations would be minimised by growing all samples using the same QW recipes in sequential runs in the same epitaxy campaign.

Fig. 6.7 shows that higher excitation densities should be explored to enhance the THz conversion efficiency. It is expected that the quadratic response will be lost as high excitation densities lead to free carrier effects resulting in excitonic behaviour being lost as the Mott density is approached. This measurement can be achieved in two ways.

Using lasers with higher powers is a simple option but this would require a move away from semiconductor lasers to say two Ti:sapphire sources. Another route would be to use a Galilean telescope [14], to decrease the collimated laser beam diameter, resulting in an increase in the laser power density.

References

1. Yariv, A.: hypermespherical si lense. Oxford University Press, 1997.

2. Hecht, E.: Optics, 4th. , San Francisco, US (2002).

3. Lee, Y.-S.: Principles of Terahertz Science and Technology. Springer, New York, U.S.A (2009).

4. Fox, M.: Optical properties of solids. Oxford University Press, Oxford (2010).

5. Li, H.H.: Refractive-index of silicon and germanium and its wavelength and temperature derivatives. J. Phys. Chem. Ref. Data 9, 561–658 (1980).

6. Akiba, T., Seki, Y., Odagiri, M., Hashino, I., Suizu, K., Avetisyan, Y.H., Miyamoto, K., Omatsu, T.: Terahertz wave generation using type II phase matching polarization combination via difference frequency generation with LiNbO 3. Jpn. J. Appl. Phys. 54, 62202 (2015).

7. Hanamura, E.: Rapid radiative decay and enhanced optical nonlinearity of excitons in a quantum well. Phys. Rev. B. 38, 1228 (1988).

8. Schultheis, L., Honold, A., Kuhl, J., Köhler, K., Tu, C.W.: Optical dephasing of homogeneously broadened two-dimensional exciton transitions in GaAs quantum wells. Phys. Rev. B. 34, 9027 (1986).

9. Knox, W.H., Fork, R.L., Downer, M.C., Miller, D.A.B., Chemla, D.S., Shank, C. V, Gossard, A.C., Wiegmann, W.: Femtosecond dynamics of resonantly excited excitons in room-temperature GaAs quantum wells. Phys. Rev. Lett. 54, 1306 (1985).

10. Khurgin, J., Li, S.: Coulomb enhancement of the third-order nonlinearities in the mesoscopic semiconductor structures. Appl. Phys. A Mater. Sci. Process. 53, 523–534 (1991).

11. Timurdogan, E., Poulton, C. V, Byrd, M.J., Watts, M.R.: Electric field-induced second-order nonlinear optical effects in silicon waveguides. Nat. Photonics. 11, 200–206 (2017).

12. Shen, Y.R.: Surface properties probed by second-harmonic and sum-

frequency generation. Nature. 337, 519–525 (1989).

13. Maker, P.D., Terhune, R.W.: Study of optical effects due to an induced polarization third order in the electric field strength. Phys. Rev. 137, A801 (1965).

14. Elescopes, R.E.T.: Lab 4 : Afocal Systems. , OPTI 202L - GEOMETRICAL AND INSTRUMENTAL OPTICS LAB LAB (1976).

Chapter Seven

THz Absorption Spectrometer

7.1 Introduction

This chapter demonstrates the use of my tuneable continuous-wave THz emitter source for spectroscopic applications. The chapter explores the atmospheric attenuation of the THz emission at the frequency of 0.75 THz and describes the modified experimental setup used to measure the different attenuation peaks in the frequency range 0.65-0.85 THz. It is also investigates, both theoretically and experimentally, the demonstration of a transmission spectrometer indicating on absorption peaks of water vapour in the 0.65-0.85 THz wave frequency range. Furthermore, it highlights the spectral investigation of the emission linewidths of both laser beams at two specific regimes and studies their consequences for the generation of terahertz radiation and the broadening of the laser beams spectral linewidth.

7.2 The Absorption Lines at 0.75 THz

The electromagnetic wave attenuation through the atmosphere is dominated by absorption by molecular water vapour [1], These are polar molecules with well-studied spectral lines in the range of THz frequencies [2–6]. For this reason, it was decided to measure the attenuation caused by the absorption peaks of water vapour at the frequency of 0.75 THz in order to demonstrate the capability of the studied THz system for the identification of transition lines for a given element,

The same THz setup as described in 5.2 was used to measure the beam shape and atmospheric attenuation. Fig. 7.1 is a schematic diagram of the detector translation in the L and X direction and how the THz signal was convoluted by the size of the detector's active area. Since the detector's active area is only 4 mm^2 it is unable to collect the entire THz signal that is coupled with the Si lens to free space.

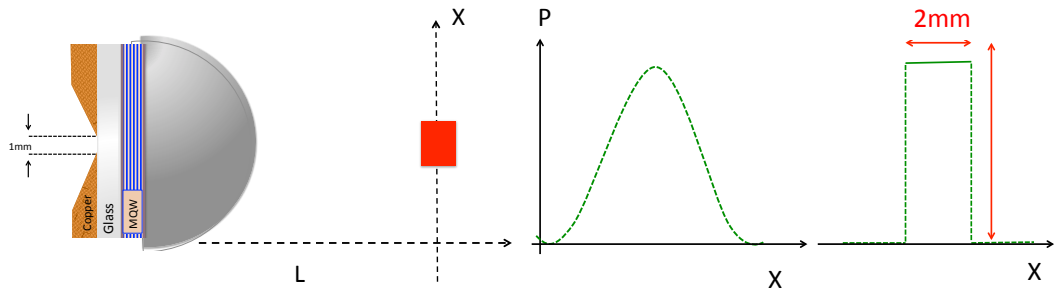

Figure 7.1 Detector movements in the L and X direction, and the limitation posed by the active area in respect to collecting the THz spectra

The attenuation measurements were carried out by setting the FP and DFB laser wavelengths to the wavelength that emits THz waves at a frequency 0.75 THz. The detector position was changed from 1 mm to 6 mm in the L direction and from -3 mm to +3 mm in the X direction, the negative / positive sign refer to the left and

right side of the centre point of the active area of the detector. Fig. 7.2 shows the transmitted THz wave pattern as recorded at different points of X or L for emission at 0.75 THz.

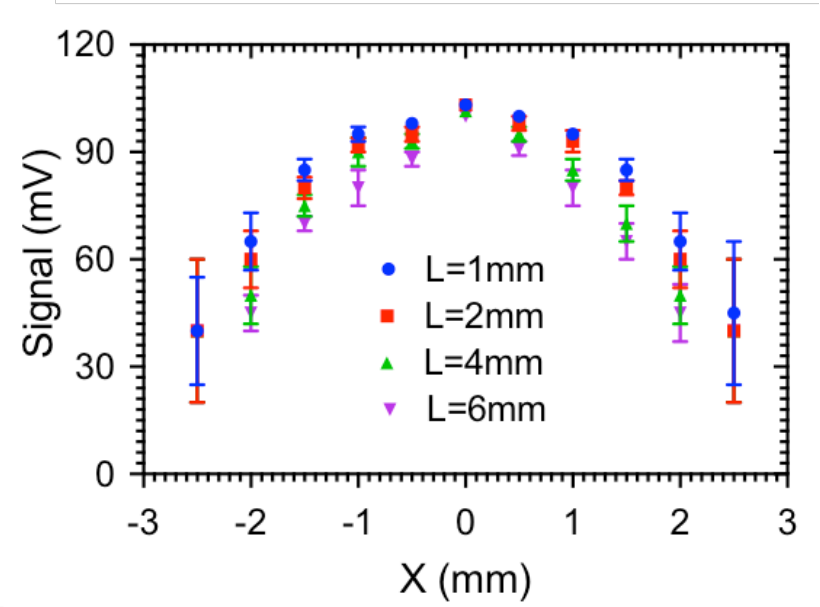

Figure 7.2 Measured radiation patterns as a function of X, at four different L as indicated in the legend on the figure, at 0.75 THz

The results indicate that the coupled THz wave is divergent with an angle of $\approx < 10°$. Also, the emission signal measurements in the X direction clearly show a significant decline in power and more uncertainty in the measurements at $X > \pm 1.5$ mm, due to the detector size limitation, which could not capture the whole THz beam, the THz beam shape is convoluted with respect to the active area size. This meant that the measurement / calculation of the attenuation was undertaken in the L direction only, since the detector could be aligned to detect the central part of the spectrum when the signal power was maximum, thus ensuring that the reduction in the THz signal power at different path lengths was due to the attenuation resulting from the absorption of molecular water vapour in the atmosphere.

Fig. 7.3 shows the signal for 0.75 THz in the L direction as a function of the wave path up to 10 mm. The results confirm that the THz signal at a frequency of 0.75 THz decreases as a function of the THz wave path length increasing.

The attenuation was calculated for a path length of 9 mm using Eq. 7.1 [7].

$$\text{Attenuation(dB)} = -\frac{10}{L} \times \log_{10}\left(\frac{P_{out}}{P_{in}}\right) \tag{7.1}$$

where

L: is the THz path

P_{out}: THz signal output power

P_{in}: THz signal input power

The signal at 1 mm was considered as the input signal and the signal at 10 mm as the output signal, and the attenuation was found to be ($\approx 4.5\times10^4$ dB/km). The experiment was carried out at room temperature (19 °C) and a humidity of 49%.

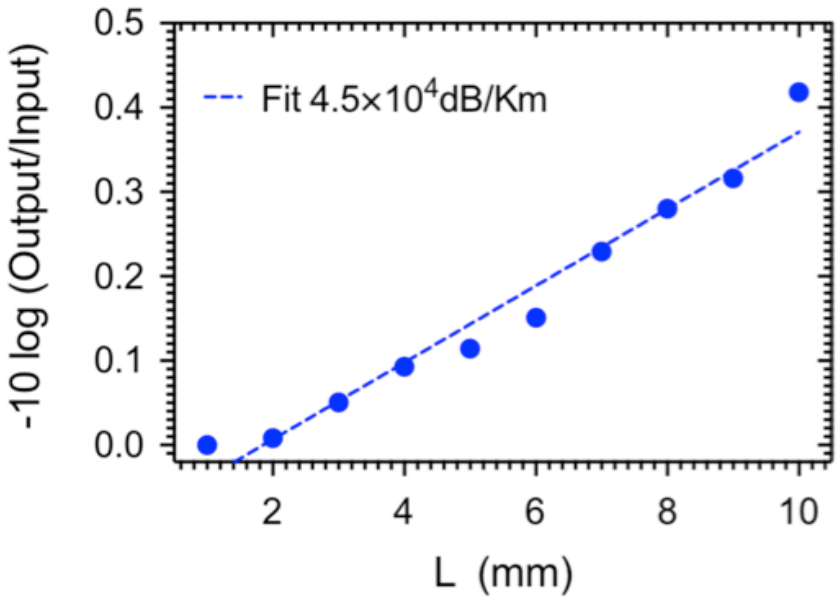

Figure 7.3 THz signal as a function of electromagnetic path length at 0.75 THz

The experimental results clearly show relatively higher attenuation (absorption) compared to the results of ≈ 2×10^4 dB/km in [2, 5] and ≈1-2×10^4 dB/km according to [8].

It is suggested that this apparent overestimation was because the detector was over filled by the beam, due to the THz beam divergence, with this overfilling increasing as L increases.

A MATLAB code, using the database in [9], was used to model the signals that propagate through atmospheric gases to calculate the atmospheric attenuation in a similar state to our experimental environment of 19 °C and 49% humidity, together with T= 24 °C and 60% humidity for a frequency range of 0.6-0.9 THz. The results are plotted in Fig. 7.4.

It is clear that the attenuation is sensitive to the ratio of the humidity and also to the temperature, as shown in Fig. 7.4 and also justified in [8, 10–12].

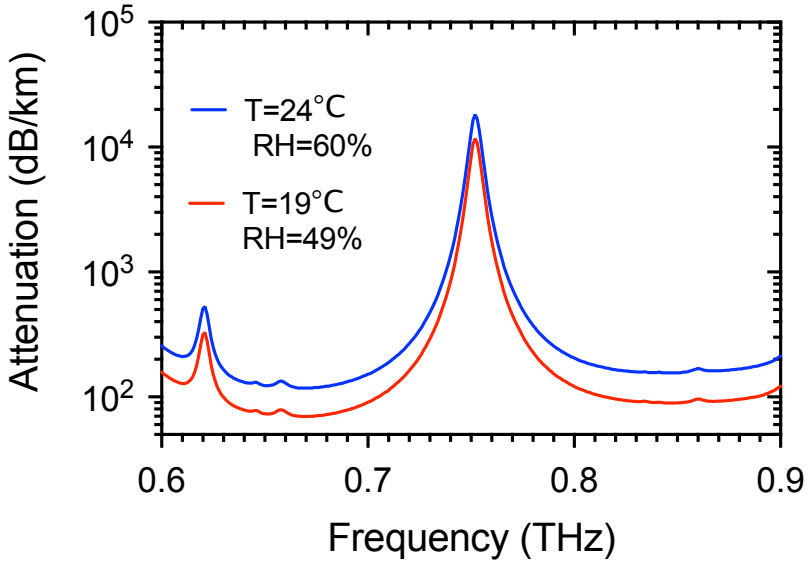

Figure 7.4 Simulated atmospheric attenuation for 0.6-0.9 THz at 19 °C, relative humidity 49% and T=24 °C, RH=60%, clearly showing the attenuation at 0.75 THz

7.3 The Modified Experimental Setup

A 3D image of the modified THz system using the CW THz source for a gas spectrometer application is shown in Fig. 7.5.

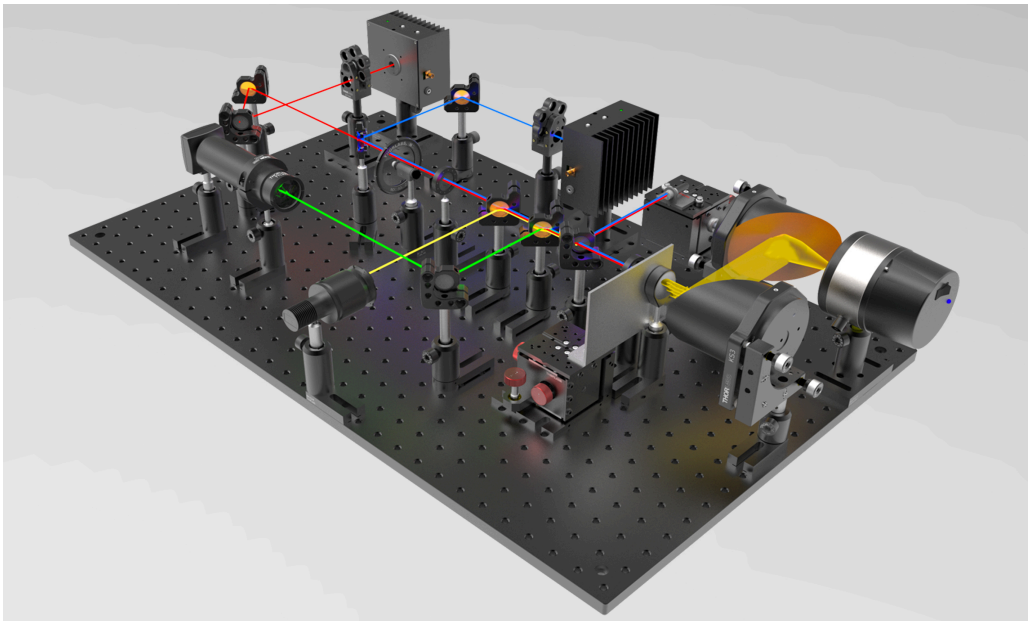

Figure 7.5 Experimental setup. Two parabolic mirrors were added to the collection system in order to collect and focus the THz beam on the active area of the detector, figure produced by SolidWorks

The THz measurement setup described in section 5.2 was modified by adding two parabolic mirrors to the THz wave collection. One of the mirrors was fixed on a mount and the other was installed on a translation stage in order to be able to change the terahertz beam path lengths, as shown in Fig. 7.6.

For each THz wave frequency the radiation was collimated by the first parabolic mirror, with a focal length of 152.4 mm, and then the collimated beam was incident on the second mirror surface, which was aligned and positioned at its focal length (as shown in Fig. 7.6).

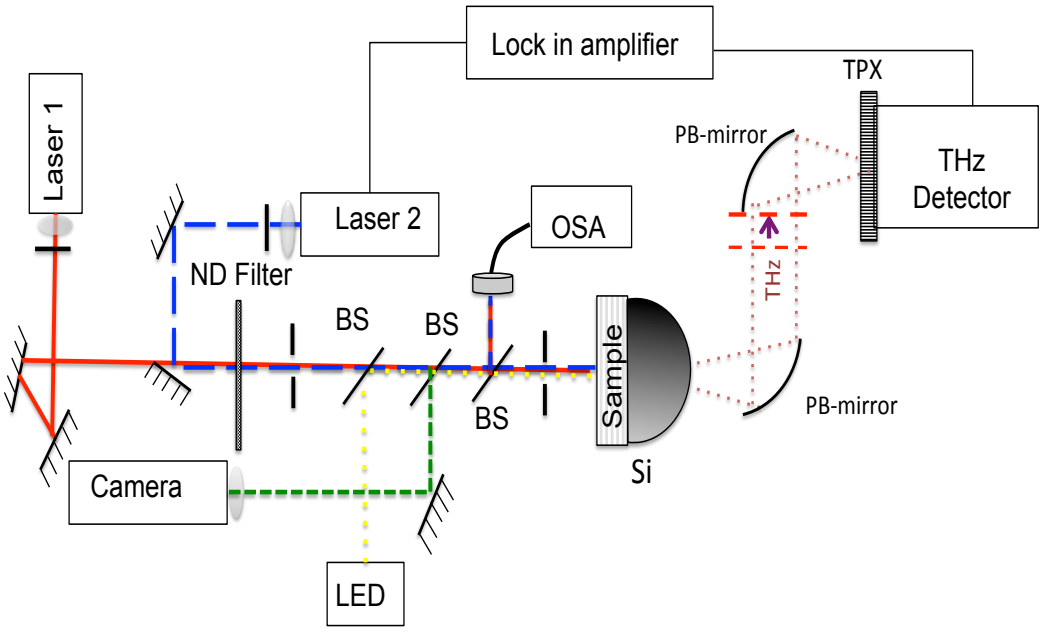

Figure 7.6 Schematic diagram of the THz set up with the parabolic mirrors, also showing the possible change in the THz wave path length

The measurements were performed at room temperature and the following steps were performed:

- The THz wave frequency was assumed to be equal to the frequency difference between the two laser sources, and then the specific FP laser wavelength was identified and tuned by changing the current and temperature.
- The collection system was aligned, and the mirrors set at a distance of 50 mm from each other. The signal was amplified by a lock-in amplifier and then recorded by the detector.
- In order to change the THz radiation path, the second mirror was moved away from the first mirror in order to increase the THz wave path length to 150 mm, and the detector was again re-aligned, followed by the THz signal recording.

The above steps were repeated for each THz frequency.

The attenuation was calculated by using Eq. 7.1, with the signal recorded at a 50 mm mirror distance being set as the input signal, and the signal that was measured at 150 mm being set as the output single.

All the THz signals were measured at room temperature (19 °C) and a humidity of 49%. Fig. 7.7 shows the calculated attenuation using the THz setup when adding the parabolic mirrors to collect the transmitted THz signal.

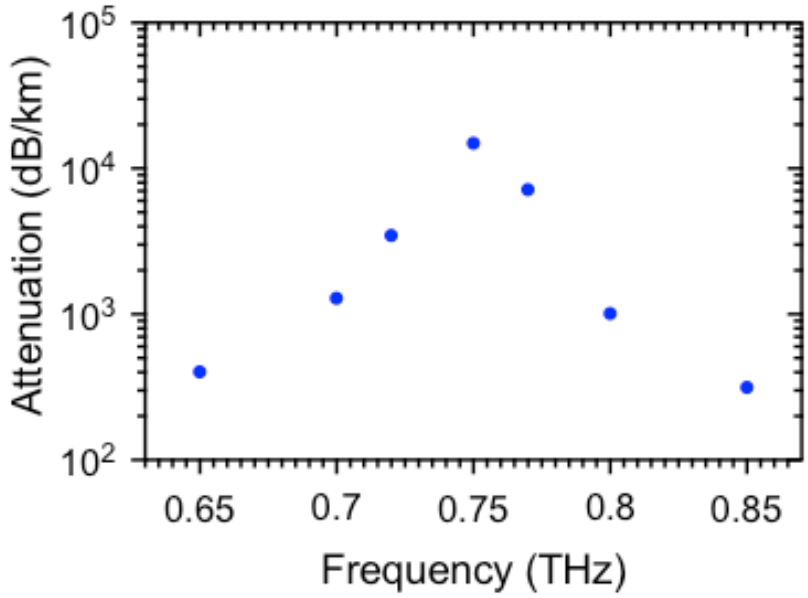

Figure 7.7 Transmission at 0.65, 0.7, 0.75, 0.8 and 0.85 THz, calculated for the measured THz signal using the modified setup

The parabolic mirrors improved the collection system and focused the THz beam to the active area of the detector, thus enabling the whole signal power to be extracted, amplified and recorded by the lock-in amplifier.

7.4 Results and Discussions

Fig. 7.8 plots the attenuation coefficient of the THz signal through air between 650 and 850 GHz, spanning a water absorption line at 750 GHz. Experimental points are plotted in addition to the expected atmospheric absorption computed by a summation of individual absorption lines that is valid for this frequency range.

Since the bandwidth of the CW THz spectra is directly related to the lasers' linewidth, and their stability, and considering both the broadening of the linewidth in the laser beams (as shown in Fig. 5.5), and the OSA resolution of 0.1 nm, it can be seen (green line) that the absorption spectrum convoluted with a Gaussian function with a standard deviation equal to this broadening in the FP line shape (21 GHz). An excellent agreement fit between the measured and simulated results data is therefore observed, demonstrating the utility of this tuneable THz source for performing absorption spectroscopy.

It is noted that DFB lasers should provide ~<MHz linewidth [13] and with external cavity lasers can have <kHz linewidth [14]. Future optimized systems should have resolution similar to these values.

The main experimental problem lay in maintaining the stability of the entire system, including the stability of the laser beams' linewidth and power.

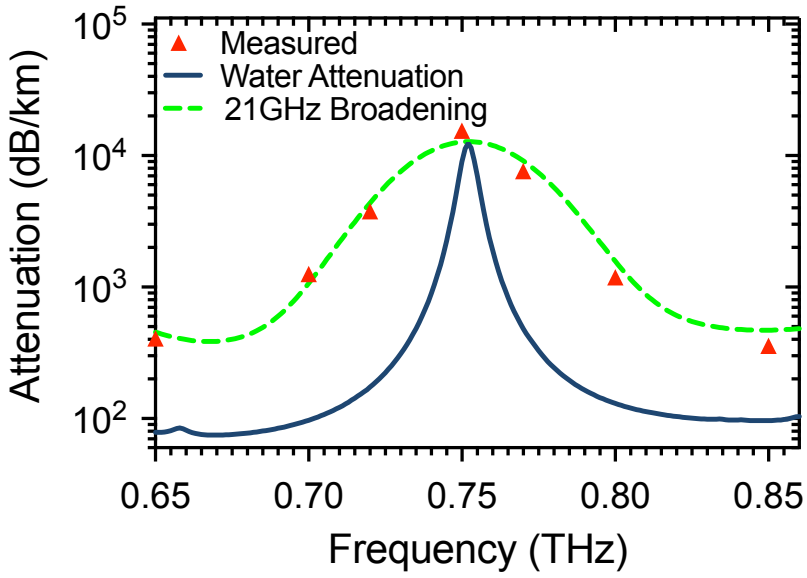

Figure 7.8 Transmission at THz range 0.65-0.85THz, theoretically calculated in (dark blue); the solid triangles are the measured data, and the dashed green line is the Gaussian Fitting, with respect to the broadening of the laser beams

The laser power was monitored along their paths, and in order to ensure the stability of the laser beams' line shape, the two laser beams were investigated six different times (A-F), 15-30 minutes apart, when set to produce THz waves at a specific frequency (0.85 THz).

Fig. 7.9 (a) plots the laser's spectra on these six occasions (A-F). In order to more carefully investigate the long-term stability of the THz source, this data is re-plotted with expanded scales for the F-P (Fig. 7.9 (b)), and the DFB (Fig. 7.9 (c)). Gaussian fittings were used to determine the peak wavelengths for each spectrum and the FWHM for both lasers' emission peaks in each spectrum. The uncertainty in peak wavelength was ±0.006 nm, resulting in a frequency uncertainty of ± 2.5 GHz for the THz signal. Whilst in future, this stability may need to be improved for spectroscopic applications, at the moment the broad spectral linewidth of the FP laser is the critical limiter to spectral resolution.

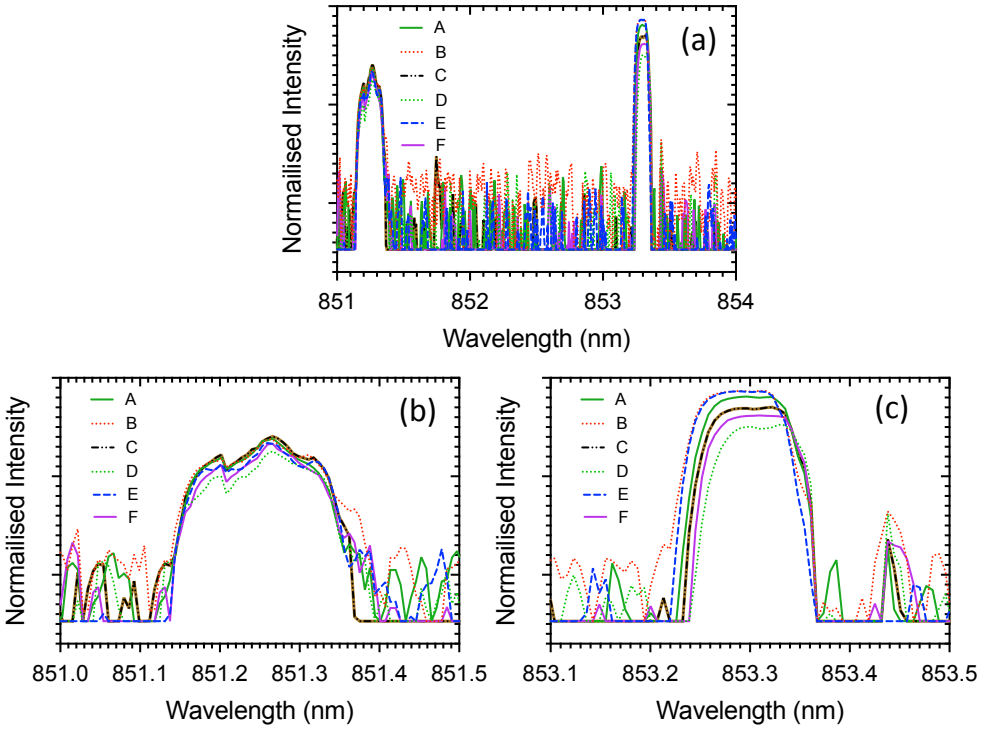

Figure 7.9 (a) Laser spectra at six different points 15-30 minutes apart. Gaussian fittings were used to determine the peaks for each spectrum and the FWHM for both lasers' emission peaks in each spectrum, (b) FP Laser spectra (c) DFB laser spectra

7.5 Conclusion

This study has successfully demonstrated a THz system to identify an absorption line of water vapour in a radiation frequency range of 0.65-0.85 THz.

Since the attenuation is very sensitive to both temperature and relative humidity, a model was re-produced to simulate the attenuation in the laboratory environment (T=19 °C and relative humidity 49%), and the calculated data was then used to investigate the reliability of the proposed system, and the accuracy of the measurement results.

The results indicated a good agreement between the calculated data and the measured data, and therefore the proposed system is considered an attractive source for a wide range of spectroscopy applications.

7.6 Future Work

Since the bandwidth of the CW THz spectra is directly related to the lasers' linewidth, and their stability. Laser sources that have a narrower linewidth such as DFB laser or an external cavity F-P is preferable and could be used to improve the CW THz spectra (get a narrower THz spectra bandwidth). The external cavity may also improve the stability of the laser beams.

References

1. Deepak, A., Wilkerson, T.D., Ruhnke, L.H.: Atmospheric water vapor. Elsevier (2013).

2. Exter, M.V., Fattinger CH., and G.: Terahertz time-domain spectroscopy of water vapor. Opt. Lett. 14, 1128–1130 (1989).

3. Mittleman, D.M., Jacobsen, R.H., Neelamani, R., Baraniuk, R.G., Nuss, M.C.: Gas sensing using terahertz time-domain spectroscopy. Appl. Phys. B Lasers Opt. 67, 379–390 (1998).

4. Möller, K.D., Rothschild, W.G.: Far-infrared spectroscopy. New York Wiley. (1971).

5. Park, I., Sydlo, C., Fischer, I., Elsäßer, W., Hartnagel, H.L.: Generation and spectroscopic application of tunable continuous-wave terahertz radiation using a dual-mode semiconductor laser. Meas. Sci. Technol. 19, 1–9 (2008).

6. Jepsen, P.U., Jacobsen, R.H., Keiding, S.R.: Generation and detection of terahertz pulses from biased semiconductor antennas. J. Opt. Soc. Am. B. 13, 2424 (1996).

7. Hollas, J.M.: Modern Spectroscopy. John Wiley & Sons Ltd., UK (1987).

8. Slocum, D.M., Slingerland, E.J., Giles, R.H., Goyette, T.M.: Atmospheric absorption of terahertz radiation and water vapor continuum effects. J. Quant. Spectrosc. Radiat. Transf. 127, 49–63 (2013).

9. Radiocommunication Sector of International Telecommunication Union. Recommendation ITU-R P.676-10: Attenuation by atmospheric gases. (2013).

10. Lee, Y.-S.: Principles of Terahertz Science and Technology. Springer, New York, U.S.A (2009).

11. Nagatsuma, T., Ducournau, G., Renaud, C.C.: Advances in terahertz communications accelerated by photonics. Nat Phot. 10, 371–379 (2016).

12. Yang, Y., Shutler, A., Grischkowsky, D.: Measurement of the transmission of the atmosphere from 0.2 to 2 THz. Opt. Express. 19, 8830 (2011).

13. Kojima, K., Kyuma, K., Nakayama, T.: Analysis of the spectral linewidth of distributed feedback laser diodes. J. Light. Technol. 3, 1048–1055 (1985).

14. Huang, S., Zhu, T., Yin, G., Lan, T., Li, F., Huang, L., Liu, M.: Dual-cavity feedback assisted DFB narrow linewidth laser. Sci. Rep. 7, (2017).

Chapter Eight

Conclusion and Future Work

8.1 Conclusion

The aim of the research discussed throughout this thesis was to produce an efficient emitter for THz generation that was low cost, compact and portable, while being widely tuneable across the THz spectrum and able to operate at room temperature.

A theoretical model of the MQW was developed to provide the detail about the width of the wells and the barriers, for which excitation of of E1-HH1, E1-LH1 excitons could be achieved through the use of cheap, widely commercially available continuous wave lasers.

The model was also used successfully to investigate the sufficient barrier thickness that could separate the wells properly to minimise carrier tunneling between QWs. The sample was grown by MBE, and opto-electronic characterization of the fabricated mesa diode was carried out using different experimental setups. According to the sample characterization results, the transition energy matched the modelled results well, suggesting that the sample was matched to the design.

Prior to the THz measurements, the sample was processed by using different techniques to achieve maximum excitation power absorption and to minimize the THz absorption within the sample. Having been supported with diamond or glass, a

THz absorption spectrum of the sample was measured in order to find out the exact energies of the transitions peaks. A specially made experimental setup was built to measure the THz, and the commercial lasers used were characterized. In situ absorption spectra measurements showed no saturation of the excitonic transitions within the QWs at the ecitation powers used.

The preliminary measurements of THz indicated emission of tunable CW THz at room temperature through second order nonlinear processes, as demonstrated by the power dependence of the THz power. Moreover the possible origin of the THz signal was explored. Initially the wavelength was not accurately identified but an etalon interferometer allowed three different THz radiation wavelengths to be measured. A comparatively efficient, tunable THz wave generated at room temperature was confirmed. This was then exploited for spectrometer applications, with the attenuation through the atmosphere due to the absorption of water vapor being measured. When this was compared to database values, a good match was recorded, despite some broadening due to unexpected pump instability of one of the laser linewidths.

8.2 Future Work

Although I have realised an efficient tunable THz source working at room temperature and these results are highly competitive with the current state-of-the-art for THz sources, it is possible to improve the efficiency of the device by considering the following suggested methods.

- A comprehensive study of the optimal growth techniques for realising perfect structures and hence narrow excitonic transitions are required.

- Using different growth processes in MBE such as migration-enhanced epitaxy (MEE) need to be considered as it might enhance excitonic transitions. Also, MOVPE could be considered when different material such as InGaP which has a good lattice match to the GaAs could be used in between the AlGaAs and the n-GaAs substrate layers during the sample growth (in order to provide an easier way to remove the substrate), since a high selectivity rate of the GaAs over InGaP or InGaP over GaAs is achievable with using plasma dry etching and also wet etch can be used efficiently to etch the GaAs, in all cases the sample could be release from the substrate. Furthermore. The high resistivity Si has a good transparency to THz, therefore it could be used (bound to the backside of the sample) instead of the diamond (bound to the front side of the sample) to support the thin sample and in meanwhile provide a good waveguide platform for the THz wave.
- Photoluminescence excitation (PLE) and photoluminescence (PL) could be used in order to determine the transition linewidths, free of thermal broadening (at low temperature).
- Raman spectroscopy could be used to investigate the possible change in strain in the sample after the preparation process (removing the cap layer and the substrate).
- Fourier transform infrared (FTIR) spectroscopy is highly recommended for identifying the frequency for different THz signals more accurately and also measuring the line width of the THz signal and within a short time and less effort.

- Since the electric field is expected to be playing a key role in generating the THz signal it is worthy of further investigation. An increased electric field can be expected to increase the electron-hole wave-function separation and hence increase χ^2. However, an increased E-field, increase electron-hole wave-function overlap and meanwhile lead to reduce the absorption, that results in reducing the THz power. There are two possible routes to vary the E-Field applied to the device. Either creating a sample with contacts to allow a bias to be applied would allow a wide range of E-Fields to be studied, but creating such a device poses significant challenges. Metal tracks would need to be patterned on glass/diamond is required, and also n and p contacts would need to be on only one side of the sample (these would have to be gold plated to increase the height of contacts and soldered).

  An alternative route is varying the built in electric field by growing a series of samples grown where the intrinsic region width is changed. This would be simple to implement within the existing system, as new samples could be readily fabricated as laid out in chapter 3. Yet, new epitaxial growths may require additional funds/time, and each sample allows only one E-field to be investigated. Since there would be some additional uncertainty as different samples are used. Careful characterisation of the materials would be required to ensure that their quality was comparable in each growth run. Such variations would be minimised by growing all samples using the same QW recipes in sequential runs in the same epitaxy campaign.
- Since the THz output power depends on the excitation laser's power, an increase in the density of the applied laser power lead to an increase in the emitted THz power. Furthermore Fig. 6.7 shows that higher excitation

densities should be explored to enhance the THz conversion efficiency. It is expected that the quadratic response will be lost as high excitation densities lead to free carrier effects resulting in excitonic behaviour being lost as the Mott density is approached. This measurement can be achieved in two ways.

- During the growth process, it would be possible to add Distributed Bragg reflector (DBR) layers to the sample structure below the active layers in order to reflect back to the active layers the light that had passed through the device without being absorbed and this would result in an increase in the THz power.
- Using lasers with higher powers is a simple option but this would require a move away from semiconductor lasers to say two Ti:sapphire sources. Another route would be to use a Galilean telescope to decrease the collimated laser beam diameter, resulting in an increase in the laser power density.
- Furthermore, ensuring both pump lasers have narrow line widths (in range of MHz) would improve the THz spectra, as it is clear that the THz emission linewidth is directly related to the laser linewidths.
- Moreover, in order to provide a compact THz source, fibre coupled lasers, fibre-optic couplers, suitable optics to realise the correct beam size and a simple sample mount should be used. More compact THz detectors are also available.
- Finally a combination of all the above techniques will further improve the already efficient performance of the THz emitters and its application for spectroscopic application. In time, this will bring the prospect of an affordable, portable and highly efficient THz imaging system even closer to reality.